8-2019

Analytical and Iterative Regularization Methods for Nonlinear Ill-posed Inverse Problems: Applications to Diffuse Optical and Electrical Impedance Tomography

Sanwar Uddin Ahmad
Clemson University, sanwardu@gmail.com

Analytical and Iterative Regularization Methods for Nonlinear Ill-posed Inverse Problems: Applications to Diffuse Optical and Electrical Impedance Tomography

---

A Dissertation
Presented to
the Graduate School of
Clemson University

In Partial Fulfillment
of the Requirements for the Degree
Doctor of Philosophy
Mathematics

---

by
Sanwar Uddin Ahmad
August 2019

Accepted by:
Dr. Taufiquar R. Khan, Committee Chair
Dr. Andrew Brown
Dr. Hyesuk Lee
Dr. Shitao Liu

Abstract

Electrical impedance tomography (EIT) and Diffuse Optical Tomography (DOT) are imaging methods that have been gaining more popularity due to their ease of use and non-ivasiveness. EIT and DOT can potentially be used as alternatives to traditional imaging techniques, such as computed tomography (CT) scans, to reduce the damaging effects of radiation on tissue.

The process of imaging using either EIT or DOT involves measuring the ability for tissue to impede electrical flow or absorb light, respectively. For EIT, the inner distribution of resistivity, which corresponds to different resistivity properties of different tissues, is estimated from the voltage potentials measured on the boundary of the object being imaged. In DOT, the optical properties of the tissue, mainly scattering and absorption, are estimated by measuring the light on the boundary of the tissue illuminated by a near-infrared source at the tissue's surface.

In this dissertation, we investigate a direct method for solving the EIT inverse problem using mollifier regularization, which is then modified and extended to solve the inverse problem in DOT. First, the mollifier method is formulated and then its efficacy is verified by developing an appropriate algorithm. For EIT and DOT, a comprehen-

sive numerical and computational comparison, using several types of regularization techniques ranging from analytical to iterative to statistical method, is performed. Based on the comparative results using the aforementioned regularization methods, a novel hybrid method combining the deterministic (mollifier and iterative) and statistical (iterative and statistical) is proposed. The efficacy of the proposed method is then further investigated via simulations and using experimental data for damage detection in concrete.

Dedication

To the almighty God and my family.

Acknowledgments

I would like to thank Almighty Allah who gives me the capability and strength to fulfill my long-cherished dream of earning doctoral degree from the United States of America.

I would like to express my special thanks of gratitude to my advisor, Dr. Taufiquar Khan, who advised me since my first year at Clemson. His guidance helped me in all the time of research and writing of this dissertation. He was always confident in my abilities, encouraged me to pursue my passions, and do what was best for me since the beginning.

I am also using this opportunity to express my gratitude to all, the School of Mathematical and Statistical Science's faculties and staffs at Clemson who have been so kind and supportive throughout my graduate life. I would like to especially thank my committee members, Dr. Andrew Brown, Dr. Hyesuk Lee, and Dr. Shitao Liu, for their valuable time and support.

Heartiest thanks to our research group members, Dr. Taufiquar Khan (Chair), Thowhida Akther, Matthew Brinckerhoff, Shyla Kupis, Lee Redfearn, Scott Scruggs, Thanh To, for their inspiring guidance, invaluable constructive criticism and friendly advice at our research group meetings. Also, I would like to give a special thanks to

Shyla Kupis for helping to review this dissertation.

A special thanks to all the Bangladeshi community members at Clemson who supported me from the beginning of my stay here, encouraged me to start the study, and helped me in many ways.

I always believe from my heart that, there have always been my parents who are praying for me, their heartiest support and suffering since my child hood. I wish, they are here with me today. I also remember my Late parents-in-law who encouraged me to pursue a higher degree. Especially my mother-in-law did a lot till her death to look after my daughter and wife while I was busy with my future goal. I want to express my very profound gratitude to my elder brother and sister unfailing support and continuous encouragement since my childhood. Also, I want to acknowledge all the other family members, my only sister-in-law, and brothers-in-law, who never forget to appreciate my single achievement.

And last but certainly not least I would like to thank my beloved Wife Thowhida Akther and our only daughter Subah Zareen Tia whose sacrifice and dreams to fulfill my dream. Sometimes I lose my beliefs, but my wife never stopped believing in me and has been a firm supporter of mine all these years. She is been always there to help me in my academic needs as well as to perform our household activities smoothly. And it's my daughter who sacrificed most, in my entire graduate life. This accomplishment would not have been possible without them.

I know there are many I forgot to thank or thanked inadequately. When I look back at all the people who have touched my life in just these few years of my life, I am overwhelmed. Thanks Allah again for everything that I have and that I achieved in my life.

Table of Contents

List of Tables

List of Figures

List of Symbols

Ω	Medium or object
$\partial\Omega$	boundary of Ω
g	measured electric potential or Dirichlet data
σ	conductivity distribution
u	electric potential/photon density inside Ω
Γ_D	Dirichlet trace for forward EIT
Γ_N	Neumann trace for forward EIT
γ_D	Dirichlet trace for forward DOT
γ_N	Neumann trace for forward DOT
γ_R	Robin trace for forward DOT
H	Hilbert space
B	bilinear form
F	bounded linear functional
$\mathcal{A}$	admissible space for σ
I	vector of injected current
$\mathbb{F}$	scalar field
F_D	linear functional for Dirichlet forward operator of EIT
F_N	linear functional for Neumann forward operator of EIT
e_l	surface area of l-th electrode
z_l	contact impedance at l-th electrode
U_l	measured electric potential at l-th electrode
f	Neumann data
k	wave length number
t	time
c	speed of light
S	strength of the source

D	diffusion coefficient
μ_a	absorption coefficient
μ_s	scattering coefficient
μ_s'	reduced scattering coefficient
$\frac{\partial u}{\partial n}$	normal component of the derivative of u
Q	parameter space for D and μ_a
ε	additive Gaussian noise
β	regularization parameter
F	forward map
$\tilde{q}$	values of optical parameters
$\tilde{q}_b$	homogeneous background of optical parameters
α_D	step size for D
α_u	step size for u
V_i	measured voltages
$\wedge_\sigma$	Dirichlet to Neumann operator for EIT
$J_\lambda(\cdot)$	cost functional for the inverse EIT problem
λ	regularization parameter
Γ_D	Dirichlet trace operator of forward DOT operator
Γ_N	Neumann trace operator of forward DOT operator
g^δ	noisy data
δ	noise level
$J_\beta(\cdot)$	cost functional for the inverse DOT problem
$\tilde{F}_R$	forward operator for Robin DOT problem
β	regularization parameter
$\mathcal{F}$	solution set for Schródinger differetial equation
$\mathcal{G}_0$	free-space Green's function
e_γ	standard mollifier
$\tilde{e}_\gamma$	effective mollifier
γ	resolution parameter
h_l	orthonormal basis for $\mathcal{F}$

Chapter 1

Introduction

In 1896, the German physicist Wilhelm Conrad Röntgen invented a new kind of ray called X-ray, and he was able to measure the absorption of X-rays traveling through a body to obtain direct images of the body's interior [72]. Nowadays most hospitals use commercial computed tomography (CT) machines, which are used to measure the absorption of radiation by a body for early detection of cancer and other types of problems. However, CT imaging involves the use of x-rays, which are a form of ionizing radiation. Exposure to ionizing radiation is known to be harmful and may increase the risk of cancer. Hence, it is desirable to find new, non-invasive medical imaging methods for early detection of cancer. In this dissertation, we present analytical and iterative methods for solving the inverse problems for Electrical Impedance Tomography (EIT) and Diffuse Optical Tomography (DOT) inverse problems, two potentially non-invasive alternatives to CT imaging.

The theory and applications for inverse problems in EIT and DOT has been signifi-

cantly developed and advanced in recent years, particularly in the context of medical imaging. However there is still a need to advance current techniques for solving the EIT and DOT inverse problems by improving existing methods and developing new tomographic methods. In contrast to the CT inverse problem, the EIT and the DOT inverse problems are neither linear nor well-posed [22, 46, 48, 78], which makes solving the inverse problem very challenging in terms of obtaining highly resolvable images of a body's internal resistivity distribution. According to Hadamard's definition of well-posedness [36]:

Definition 1. *(Well-posedness) A Problem is well-posed if*

- *A solution exists.*
- *The solution is unique.*
- *The solution depends continuously on the data.*

If a problem is not well-posed it is called ill-posed.

1.1 Electrical Impedance Tomography

Electrical impedance tomography (EIT) uses low-frequency electrical current to probe a body and measure its resistance or impedance of electrical flow; the method is therefore sensitive to changes in electrical conductivity. By injecting known amounts of current and measuring the resulting electrical potential field at points on the boundary of the body, it is possible to invert such data to determine the conductivity or

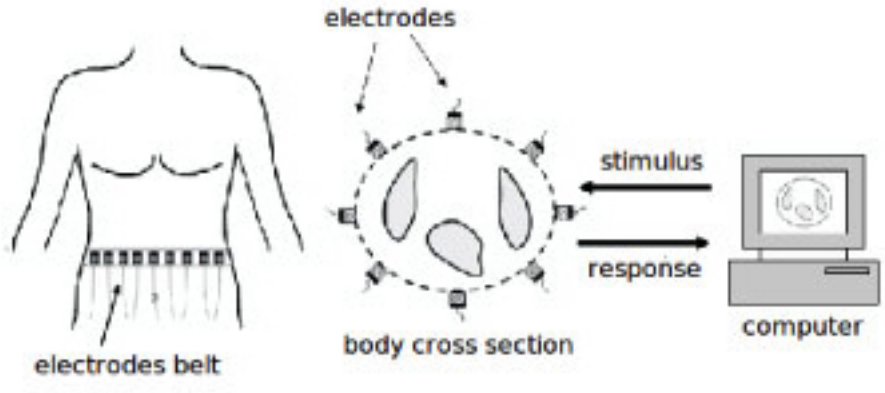

Figure 1.1: Typical EIT experiment (this figure is adapted from [61])

resistivity inside the body probed by the currents. EIT methods have shown to work well in both geophysical and industrial settings and, therefore, it is possible that future medical imaging applications may follow rather rapidly in applicability from the advancements in other applications.

In Electrical Impedance Tomography (EIT), the internal resistivity distribution is reconstructed using electrical measurement from the boundary of the object. This resistivity distribution carries valuable information about the interior of the object. The EIT forward problem is described by the elliptic differential equation, with known electrical conductivity σ, for the electric potential u with Neuman boundary condition

$$-\text{div}(\sigma \nabla u) = 0, \text{ in } \Omega \tag{1.1}$$

where $\Omega \subset \mathbb{R}^d, d = 2$ or 3, is a bounded, connected open Lipschitz domain and $\sigma \in L^\infty(\Omega)$, i.e. there exists constants $\sigma_1, \sigma_2 \in \mathbb{R}$, s.t., $0 < \sigma_1 < \sigma < \sigma_2 < \infty$. The electric potentials at the electrodes are measured to compute the voltage measurements. The inverse problem then involves determining the electrical conductivity of σ from these noisy voltage measurements.

1.2 Diffuse Optical Tomography

In optical tomography an image is constructed by reconstructing the optical parameters, usually the optical scattering and absorption coefficients, within a medium. These optical parameters are determined by illuminating the medium with a flash of near-infrared light and taking measurements on the surface. Typically this source is laser light in the visible (about 400 to 700 nm) or near infrared range. By "near-infrared", we are referring to wavelengths between 700 and 1000 nanometers (nm), with most experimental techniques usually falling between 700 nm and 850 nm.
Basically, DOT is a type of optical imaging, is the process of imaging an object through sectioning by use of an optical wave. Tissues are highly scattered medium, so, as the collimated laser beam passes through the tissue, some of the light is absorbed by chromophores (such as hemoglobin, lipid and water), but most of it is scattered. In fact, in the near infrared range, it has been shown that absorption of light by biological tissue is minimized, so it can penetrate up to about 6 cm in breast tissue and about 2 to 3 cm in the brain and joints [45].
The forward problem in DOT involves solving an elliptic partial differential equation with Robin boundary conditions where μ_a and D are known. The solution u describes the photon density of the scattered light arriving at the detectors. The complete DOT experiment is given in the frequency domain, with Robin boundary condition

$$-\nabla \cdot (D\nabla u) + (\mu_a + ik)u = 0 \text{ in } \Omega \tag{1.2}$$

$$\gamma_R u = u + 2D\frac{\partial u}{\partial n} = f \text{ on } \partial\Omega \tag{1.3}$$

here, D is the diffusion coefficient, μ_a is the absorption coefficient, $k = \omega/c$ is the imaginary wave number, ω is the modulation frequency of the laser, c is the speed of

light, and f is the source.

1.3 Contribution and Overview

A framework for hybrid regularization and comprehensive comparison combining analytical, iterative and statistical algorithms is presented in this dissertation for the image reconstruction problem in EIT and DOT. In this dissertation we:

- Extend the mollifier approach to solve the inverse problems in EIT to DOT.
- Investigate the appropriate modification of the formulaiton of the mollifier method for EIT.
- Develop computational algorithms for the mollifier method to verify the efficacy of the analytical approach using simulations and experimental data.
- Perform a comprehensive comparison of a wide range of regularization techniques for EIT and DOT, including analytical mollifier, statistical and iterative regularization methods, by devising computational algorithms in MATLAB.
- Propose hybrid algorithms for both EIT and DOT reconstructions based on the comparison of of these methods; we combine several methods, which are mainly the deterministic (mollifier and iterative) and statistical (iterative and statistical).
- Verify the efficacy of the proposed hybrid methods both in simulation and using experimental data for damage detection in concrete.

This dissertation is structured as follows. In chapter 2, we briefly introduce the EIT forward problem and the Complete Electrode Model (CEM), a more complete version of EIT for experimental data. We also discuss the well-posedness of the forward operators for EIT and CEM. In chapter 3, the forward model of DOT and it's well-posedness are discussed. The existence and uniqueness of the forward solution is also represented. Chapter 4 contains the analytical setting of the inverse problem for both EIT and DOT. In chapter 5, we discuss the analytical framework of the mollifier regularization for EIT inverse problem, and propose an extension of the method to DOT. In addition, we also identify a few corrections to the method for EIT that exists in the literature. We present the implementation of the classical iteratively regularized Gauss-Newton (IRGN) method for solving the inverse problems in EIT and DOT in chapter 6. In chapter 7, we solve the inverse problems of EIT and DOT from simulated and experimental data. Finally, in chapter 8, we conclude this dissertation.

Chapter 2

Electrical Impedance Tomography

Electrical Impedance Tomography (EIT) is a noninvasive imaging technique in which the electrical conductivity, permitivity and impedance of a part of the body, Ω, is inferred from the surface, $\partial\Omega$, electrode measurements and used to form a tomographic image of that part, [17, 11, 37]. EIT can be applied to nondestructive testing [25, 65], the monitoring of oil and gas mixtures in oil pipelines [44], noninvasive medical imaging [17, 41, 9], etc. For example, EIT has been used in civil engineering to monitor water infiltration into soil [25, 12, 21, 23]. Stacey [76] also studied the EIT's feasibility by monitoring moisture movement in Berea sandstone. Hou and Lynch [42] applied EIT to loaded cementitious composites that were fiber reinforced. Among further applications for EIT is geophysical prospection [50]. The majority of EIT systems apply small alternating currents at a single frequency, however, some EIT systems use multiple frequencies to better differentiate between normal and suspected abnormal tissue within the same organ. In this chapter, we discuss the forward model for EIT and its well-posedness.

2.1 EIT forward problem

Suppose an electric current f is applied to $\partial\Omega$, boundary of a body Ω, and the electric potential g is measured on $\partial\Omega$. Then the forward problem for EIT is described by the elliptic differential equation, with known σ, for the electric potential u with Neuman boundary conditions

$$-\text{div}(\sigma\nabla u) = 0, \text{ in } \Omega \tag{2.1}$$

$$\sigma\frac{\partial u}{\partial n} = f, \text{ on } \partial\Omega \tag{2.2}$$

and with Dirichlet conditions

$$-\text{div}(\sigma\nabla u) = 0, \text{ in } \Omega \tag{2.3}$$

$$u = g, \text{ on } \partial\Omega \tag{2.4}$$

where $\Omega \subset \mathbb{R}^d, d = 2 \text{ or } 3$, is a bounded, connected open Lipschitz domain and $\sigma \in L^\infty(\Omega)$, i.e. there exists constants $\sigma_1, \sigma_2 \in \mathbb{R}$, s.t., $0 < \sigma_1 < \sigma < \sigma_2 < \infty$. The Neumann trace Γ_N and the Dirichlet trace Γ_D are defined, respectively as,

$$\Gamma_N : \tilde{H}^1(\Omega) \to \tilde{H}^{-1/2}(\partial\Omega) \tag{2.5}$$

$$u \mapsto \sigma\frac{\partial u}{\partial n}|_{\partial\Omega} \tag{2.6}$$

and

$$\Gamma_D : \tilde{H}^1(\Omega) \to \tilde{H}^{1/2}(\partial\Omega) \tag{2.7}$$

$$u \mapsto u|_{\partial\Omega} \tag{2.8}$$

where the spaces above are defined as,

$$
\begin{aligned}
H^1(\Omega) &= \{v \in L^2(\Omega) | \int_\Omega |\nabla v|^2 + v^2 dx < \infty\} \\
\tilde{H}^1(\Omega) &= \{v \in H^1(\Omega) | \int_{\partial\Omega} v ds = 0\} \\
H_0^1(\Omega) &= \{v \in H^1(\Omega) | \Gamma_D(v) = 0\} \\
\tilde{H}^{-1/2}(\partial\Omega) &\cong \{\Gamma_N(v) | v \in \tilde{H}^1(\Omega)/\tilde{H}_0^1(\Omega)\} \\
\tilde{H}^{1/2}(\partial\Omega) &\cong \{\Gamma_D(v) | v \in \tilde{H}^1(\Omega)/\tilde{H}_0^1(\Omega)\}.
\end{aligned}
$$

Here $\tilde{H}^{-1/2}(\partial\Omega)$ is the dual space of $\tilde{H}^{1/2}(\partial\Omega)$. The inner product for the space $H^1(\Omega)$ is defined as,

$$\langle u, v \rangle_{H^1} = \int_\Omega (\nabla u \cdot \nabla v + uv) dx \tag{2.9}$$

In EIT, one uses the following inner product, induced by an equivalent norm $||.||_*$ to $||.||_{H^1}$ in $\tilde{H}^1(\Omega)$,

$$\langle u, v \rangle_{H^1(\Omega)} = \int_\Omega \nabla u \cdot \nabla v dx \tag{2.10}$$

Lemma 1. *If $u \in \tilde{H}^1(\Omega)$, then the norm $||u||_*^2 = \int_\Omega |\nabla u|^2 dx$ is equivalent to $||u||_{H^1(\Omega)}^2 = \int_\Omega |\nabla u|^2 + |u|^2 dx$.*

Proof. Clearly, $||u||_*^2 = \int_\Omega |\nabla u|^2 dx \leq \int_\Omega |\nabla u|^2 + |u|^2 dx = ||u||_{H^1(\Omega)}^2$.
From Poincare's inquality, there exists a constant $c > 0$, such that,

$$c \int_\Omega |\nabla u|^2 dx \geq \int_\Omega |u|^2 dx$$

Therefore,

$$\begin{aligned}\int_\Omega |\nabla u|^2 dx &= \frac{1}{1+c}\int_\Omega |\nabla u|^2 + c|\nabla u|^2 dx \\ &\geq \frac{1}{1+c}\int_\Omega |\nabla u|^2 + |u|^2 dx = \frac{1}{1+c}||u||^2_{H^1(\Omega)}\end{aligned}$$

Thus there exists a constant $c > 0$, such that,

$$\frac{1}{1+c}||u||^2_{H^1(\Omega)} \leq ||u||^2_* \leq ||u||^2_{H^1(\Omega)}.$$

Hence the claim is complete. □

Next we discuss the well-posedness of the Dirichlet and Neumann problems.

2.2 Well-posedness of the forward problem

To discuss the well-posedness of the EIT forward problem, we need some preliminary results.

Definition 2. *(Bilinear Form) A function $B : V \times V \to \mathbb{F}$ is called a bilinear form if for any $u, v, w \in V$ and any $c \in \mathbb{F}$, the following conditions are satisfied.*

$$\begin{aligned}(i) B(u+v, w) &= B(u, w) + B(v, w) \\ (ii) B(u, v+w) &= B(u, v) + B(u, w) \\ (iii) B(cu, v) &= B(u, cv) = cB(u, v)\end{aligned}$$

where V is a vector space and $\mathbb{F}$ is a field of a scalar.

Theorem 1. *(Lax Miligram Theorem,[10]) Let $B : H \times H \to \mathbb{K}$, where $\mathbb{K} = \mathbb{R}$ or $\mathbb{C}$, be a bilinear ($\mathbb{K} = \mathbb{R}$)/ sesquilinear ($\mathbb{K} = \mathbb{C}$) form and $\langle \cdot, \cdot \rangle$ be an inner product defined in the Hilbert space H. If there exists $c_1, c_2 > 0$ such that for all $u, v \in H$,*

$$(i) B \text{ is coercive, i.e.,} c_1||u||^2 \leq B(u,u)$$

$$(ii) B \text{ is bounded, i.e.,} |B(u,v)| \leq c_2||u||||v||$$

then for any bounded linear functional $F : H \to \mathbb{K}$, there exists a unique $u \in H$ such that $\langle F(u), v\rangle = B(u,v)$. Moreover, $||u|| \leq \frac{1}{c}||F||$, where $c > 0$ is a constant.

Theorem 2. *(Riesz Represenation Theorem, [26, 73] Let H be a Hilbert space, and f be a continuous linear functional on H. Then there exists a unique $u \in H$ such that $f(v) = \langle v, u\rangle$, for all $v \in H$. Furthermore, $||f||_{H^*} = ||v||_H$, where H^* denotes the dual space of H.*

2.2.1 Well-posedness of the Dirichlet EIT problem

First, we discuss the uniqueness and existence of the following elliptic problem.

Lemma 2. *Let Ω be an open, bounded set and $f \in H^{-1}(\Omega)$, then for $u \in H_0^1(\Omega)$, there exists a unique weak solution to the following equations*

$$-\nabla \cdot (\sigma \nabla u) = f, \text{ in } \Omega$$

$$u = 0, \text{ on } \partial\Omega$$

with $0 < \sigma_1 < \sigma < \sigma_2 < \infty \in L^\infty(\Omega)$.

Proof. Weak formulation of the above problem can be easily obtained using Green's theorem as, for any $v \in H_0^1(\Omega)$

$$\int_\Omega \sigma \nabla u \cdot \nabla v dx = \int_\Omega f v dx$$
$$\implies B(u, v) = F(v)$$

where $B(u, v) = \int_\Omega \sigma \nabla u \cdot \nabla v dx$ and $F(v) = \int_\Omega f v dx$.

Claim. $B(u, v)$ is a bilinear form.

Let $u, v, w \in H_1^0$ and $\lambda \in \mathbb{R}$. Then,

(i)

$$\begin{aligned} B(u + w, v) &= \int_\Omega \sigma \nabla (u + w) \cdot \nabla v dx \\ &= \int_\Omega \sigma \nabla u \cdot \nabla v dx + \int_\Omega \sigma \nabla w \cdot \nabla v dx \\ &= B(u, v) + B(w, v) \end{aligned}$$

(ii)

$$\begin{aligned} B(u, v + w) &= \int_\Omega \sigma \nabla u \cdot \nabla (v + w) dx \\ &= \int_\Omega \sigma \nabla u \cdot \nabla v dx + \int_\Omega \sigma \nabla u \cdot \nabla w dx \\ &= B(u, v) + B(u, w) \end{aligned}$$

(iii)

$$\begin{aligned} B(\lambda u, v) &= \int_\Omega \sigma \nabla \lambda u \cdot \nabla v dx \\ &= \int_\Omega \sigma \nabla u \cdot \nabla \lambda v dx = B(u, \lambda v) \\ &= \lambda \int_\Omega \sigma \nabla u \cdot \nabla v dx = \lambda B(u, v) \end{aligned}$$

Hence, $B(u, v)$ is bilinear.

Claim. $B(u, v)$ is coercive and bounded.

(i) $B(u, u) = \int_\Omega \sigma |\nabla u|^2 dx \geq \sigma_1 ||u||_*^2 \geq \frac{\sigma_1}{1+c} ||u||_{H_0^1(\Omega)}^2$, for some constant $c > 0$.

Thus $B(u, v)$ is coercive.

(ii)

$$\begin{aligned} |B(u, v)| &= |\int_\Omega \sigma \nabla u \cdot \nabla v dx| \\ &\leq \sigma_2 |\int_\Omega \nabla u \cdot \nabla v dx| \\ &\leq \sigma_2 ||u||_* ||v||_* \leq \sigma_2 c_2 ||u||_{H_0^1(\Omega)} ||v||_{H_0^1(\Omega)} \end{aligned}$$

Hence, $B(u, v)$ is bounded.

Clearly, $F(v)$ is linear and by assumption it is bounded. Hence by Lax-Miligram theorem, there exists a unique $u \in H_0^1(\Omega)$, such that,

$$B(u, v) = F(v)$$

. Hence, the proof. □

Now consider the Dirichlet EIT forward problem (2.3,2.4). We want to retrieve a ho-

mogeneous problem that can be solved. Since $\partial\Omega$ is C^1 continuous and $g \in H^{1/2}(\partial\Omega)$, then there exists $u_g \in H^1(\Omega)$, such that, $u_g|_{\partial\Omega} = g$. We define, $u_0 = u - u_g$, then the Dirichlet EIT forward problem is equivalent to the follwoing elliptic problem,

$$-\nabla \cdot (\sigma \nabla u_0) = \nabla \cdot (\sigma \nabla u_g), \text{ in } \Omega$$
$$u_0 = 0, \text{ on } \partial\Omega$$

The weak formulation of the problem above can be simplified as,

$$\int_\Omega \sigma \nabla u_0 \cdot \nabla v dx = -\int_\Omega \sigma \nabla u_g \cdot \nabla v dx, \text{ for } u_0, v \in H_0^1(\Omega) \tag{2.11}$$

which can be denoted as, $B(u_0, v) = F_D(v)$. Previously, we proved that $B(u_0, v)$ is a bilinear form for any $u_0, v \in \tilde{H}^1$ and it is coercive and bounded. Clearly, $F_D(v)$ is a linear functional. We want to prove that $F_D(v)$ is bounded.
Now,

$$\begin{aligned}
|F_D(v)| &= |\int_\Omega \sigma \nabla u_g \cdot \nabla v dx| \\
&\leq \sigma_2 |\int_\Omega \nabla u_g \cdot \nabla v dx| \\
&\leq \sigma_2 ||u_g||_{H_0^1} ||v||_{H_0^1} = \sigma_2 ||u_g||_{\tilde{H}^1} ||v||_{H_0^1} \\
&\leq \sigma_2 ||u||_{\tilde{H}^{1/2} \to \tilde{H}^1} ||g||_{\tilde{H}^{1/2}} ||v||_{H_0^1} \\
&\leq \sigma_2 c ||v||_{H_0^1(\Omega)}
\end{aligned}$$

where $c > 0$ is a constant.
Hence by the Lax-Miligram theorem, we have a unique solution u_0 of the problem, and a unique solution to the Dirichlet problem (2.3-2.4) can be obtained by setting $u = u_0 + u_g$.

Now for the well-posedness of the Dirichlet problem, we need to prove that the solution depends continuously on the data.

Lemma 3. $||u||_{\tilde{H}^1(\Omega)} \leq c||g||_{\tilde{H}^{1/2}(\partial\Omega)}$.

Proof. Previously we showed that,

$$|F_D(v)| = |\int_\Omega \sigma \nabla u_g \cdot \nabla v dx| \leq \sigma_2 ||u_g||_{\tilde{H}^1} ||v||_{H_0^1}$$

Hence,

$$\begin{aligned} ||F_D||_{H_0^1(\Omega)} &= \sup_{||v||_{H_0^1(\Omega)} \neq 0} \frac{|F_D(v)|}{||v||_{H_0^1(\Omega)}} \\ &\leq \sup_{||v||_{H_0^1(\Omega)} \neq 0} \frac{\sigma_2 ||u_g||_{\tilde{H}^1(\Omega)} ||v||_{H_0^1(\Omega)}}{||v||_{H_0^1(\Omega)}} = \sigma_2 ||u_g||_{\tilde{H}^1(\Omega)} \end{aligned}$$

Thus,

$$\begin{aligned} ||u||_{H^1(\Omega)} &= ||u_0 + u_g||_{H^1(\Omega)} \\ &\leq ||u_0||_{H_0^1(\Omega)} + ||u_g||_{\tilde{H}^1(\Omega)} \\ &\leq ||F_D||_{H_0^1 \to \mathbb{R}} + ||u_g||_{\tilde{H}^1(\Omega)} \\ &\leq \sigma_2 ||u_g||_{\tilde{H}^1(\Omega)} + ||u_g||_{\tilde{H}^1(\Omega)} \leq c||g||_{\tilde{H}^{1/2}(\partial\Omega)} \end{aligned}$$

Therefore, the solution continuously depends on g. □

Hence the Dirichlet forward problem for EIT is well-posed. Next we will show the well-posedness of the Neumann forward problem.

2.2.2 Well-posedness of the Neumann EIT Problem

Consider the Neumann EIT forward problem described in (2.1)-(2.2). As before, we derive the weak formulation of the Neumann problem by the use of Green's theorem as follows.

$$\begin{aligned} -\int_\Omega \nabla \cdot (\sigma \nabla u) v dx &= 0 \\ \implies \int_\Omega \sigma \nabla u \cdot \nabla v dx - \int_{\partial\Omega} \sigma \frac{\partial u}{\partial n} v ds &= 0 \\ \implies \int_\Omega \sigma \nabla u \cdot \nabla v dx &= \int_{\partial\Omega} f v ds \\ \implies B(u,v) &= F_N(v) \end{aligned}$$

In section 2.2.1.,we showed that $B(u,v)$ is bilinear, coercive and bounded. To show the uniqueness and existence of the solution to the Neumann problem, we need to prove the following lemma.

Lemma 4. *There exists a constant $c > 0$, such that,*

$$|F_N(v)| = |\langle f, v \rangle_{\tilde{H}^{-1/2}(\partial\Omega) \times \tilde{H}^{1/2}(\partial\Omega)}| \leq c ||v||_{\tilde{H}^1(\Omega)}.$$

Proof. Let $S : \tilde{H}^{-1/2}(\partial\Omega) \to \tilde{H}^{1/2}(\partial\Omega)$ be a Riesz map, as described in Theorem 2.

Then we have,

$$\begin{aligned}|\langle f, v\rangle_{\tilde{H}^{-1/2}(\partial\Omega)\times\tilde{H}^{1/2}(\partial\Omega)}| &= |\langle Sf, v\rangle_{\tilde{H}^{1/2}(\partial\Omega)\times\tilde{H}^{1/2}(\partial\Omega)}| \\ &= |\langle F_D(Sf), v\rangle_{\tilde{H}^1(\Omega)} \\ &\leq ||F_D(Sf)||_{\tilde{H}^1(\Omega)}||v||_{\tilde{H}^1(\Omega)} \\ &\leq c||v||_{\tilde{H}^1(\Omega)}\end{aligned}$$

Hence F_N is bounded. □

Thus the weak solution of the Neumann problem (2.1), (2.2), satisfies the conditions of the Lax-Miligrm therorem, which establish the uniqueness and existence of the weak solution of the Neumann EIT forward problem. For the well-posedness of the Neumann problem, we need to prove the following lemma.

Lemma 5. $||u||_{\tilde{H}^1(\Omega)} \leq c||f||_{\tilde{H}^{1/2}(\partial\Omega)}$

Proof. From the Lax-Miligram theorem, there exists a constant c_1, such that

$$||u||_{\tilde{H}^1(\Omega)} \leq \frac{1}{c_1}||F_N||_{\tilde{H}^1(\Omega)\to\mathbb{R}}.$$

From the previous lemma, we also have,

$$|F_N| \leq ||F_D(Sf)||_{\tilde{H}^1(\Omega)}||v||_{\tilde{H}^1(\Omega)}$$

Hence,

$$\begin{aligned}
||F_N||_{\tilde{H}^1(\Omega)\to\mathbb{R}} &= \sup_{||v||_{H^1}\neq 0} \frac{|F_N(v)|}{||v||_{H^1}} \\
&\leq \sup_{||v||_{H^1}\neq 0} \frac{||F_D(Sf)||_{\tilde{H}^1(\Omega)}||v||_{\tilde{H}^1(\Omega)}}{||v||_{H^1}} \\
&= ||F_D(Sf)||_{\tilde{H}^1(\Omega)}.
\end{aligned}$$

Thus,

$$\begin{aligned}
||u||_{\tilde{H}^1(\Omega)} &\leq \frac{1}{c_1}||F_N||_{\tilde{H}^1(\Omega)\to\mathbb{R}} \\
&\leq \frac{1}{c_1}||F_D(Sf)||_{\tilde{H}^1(\Omega)} \\
&\leq \frac{c_2}{c_2}||S(f)||_{\tilde{H}^{1/2}(\partial\Omega)} \\
&\leq \frac{c_2}{c_1}||S||_{\tilde{H}^{-1/2}(\partial\Omega)\to\tilde{H}^{1/2}(\partial\Omega)}||f||_{\tilde{H}^{-1/2}(\partial\Omega)} \\
&\leq \frac{c_2 c_3}{c_1}||f||_{\tilde{H}^{-1/2}(\partial\Omega)}
\end{aligned}$$

where S is the Riesz map described in the previous lemma, and $c_1, c_2, c_3 > 0$ are constants. Hence we conclude that the Neumann solution depends continuously on data. □

2.3 Complete Electrode Model (CEM)

In EIT, we determine the conductivity distribution inside an object by applying electric currents at the boundary through electrodes and measuring the voltages at the boundary as well. The governing equations for EIT problems (2.1) is provided in

the previous chapter. In practice, currents are applied to the electrodes on the surface $\partial\Omega$ of the body. These currents produce a current density with inward pointing normal component,

$$\sigma \frac{\partial u}{\partial n} = j, \text{ on } \partial\Omega, \tag{2.12}$$

together with the conservation of charge condition $\int_{\partial\Omega} j ds = 0$ and the condition $\int_{\partial\Omega} u ds = 0$. This model is commonly known as the continuum model, [17]. Unfortunately, due to the lack of knowledge of the current density j, the continuum model does not perform well for real experiments [17, 19]. It became important to model the electrodes in order to comparing predictions of the resulting model with experimental data, [56, 75]. In this chapter, we briefly discuss the Complete Electrode Model (CEM) for the EIT problems, which is now the standard model for the EIT experiments. We briefly describe the formulation of the CEM, derive the variational form. We have also discuss the well-posedness, uniqueness and existence of the solution to the forward CEM.

2.3.1 Model

The Complete Electrode Model is the most accurate model for EIT as it accounts for the contact impedance between the object and the electrodes, [19, 75, 83]. Suppose L electrodes have been fixed around the surface of an object. Current is applied to a subset of these electrodes, and the resulting voltage is measured at all other electrodes. This EIT experiment is repeated several times with different electrode configurations to efficiently characterize the imaged object. The inverse problem

then is to reconstruct the conductivity distribution inside the object from a finite set of surface point measurements.

The equation (2.1) is used to solve the electric potential at the electrodes and inside Ω for some applied current I. We obtained (2.1) by a scaling analysis of Maxwell's equation for electromagnetic fields inside of an object [17, 83]. We denote the class of admissible conductivities as

$$\mathcal{A} = \{\sigma \in L^\infty(\Omega) | \sigma(x) \geq \sigma_0 > 0, \text{ for } x \in \Omega \text{ and } \sigma_0 \in \mathbb{R}\}.$$

Currents are applied to electrodes on the surface $\partial\Omega$ of the body. Let j denote the inward unit normal component for the current density that is produced by current on the surface. Then, the Neumann boundary condition is

$$\sigma \frac{\partial u}{\partial n} = j \quad \text{on } \partial\Omega. \tag{2.13}$$

(2.1) and (2.13) are known as the *continuum model*. In practice, the current density j at the electrodes is unknown, but $\int_{E_l} \sigma \frac{\partial u}{\partial n} dS = I_l$ is known, where n is the unit outward normal to Ω, e_l is the surface area of the lth electrode and I_l is the current injected into e_l. Thus the Neumann condition (2.13) can be rewritten as

$$\int_{e_l} \sigma \frac{\partial u}{\partial n} dS = I_l \quad \text{for } l = 1, 2, ..., L. \tag{2.14}$$

Furthermore, we know $j = 0$ for the current density on the boundary between the electrodes, such that

$$\sigma \frac{\partial u}{\partial n} = 0 \quad \text{on } \partial\Omega / \cup_{l=1}^{L} \overline{e_l}. \tag{2.15}$$

The potential on the electrodes is considered to be constant: U_l = constant. This property is known as the *shunting effect*, which is represented by

$$u = U_l, \text{ on } e_l, \text{ for } l = 1, 2, ..., L. \tag{2.16}$$

There is also an electro-chemical effect due to the formation of a thin and highly resistive layer between the electrodes and the body. Electrical impedance from this layer, z_l, is called the effective contact impedance or surface impedance at e_l. This effect changes (2.16) to

$$u + z_l \sigma \frac{\partial u}{\partial n} = U_l \quad \text{on } e_l \text{ for } l = 1, 2, ..., L. \tag{2.17}$$

The complete electrode model (CEM) consists of (2.1), (2.14), (2.15) and (2.17), together with the following conditions.

$$\sum_{l=1}^{L} I_l = 0 \quad \text{(conservation of charge)} \tag{2.18}$$

$$\sum_{l=1}^{L} U_l = 0 \quad \text{(choice of a ground)} \tag{2.19}$$

Although the CEM has a unique solution, the accuracy of it is determined by the predicted experimental measurements [75].

2.3.2 Weak formulation of CEM

Proposition 1. *Let Ω, σ and the electrodes e_l satisfies the conditions described before, and let $z_l \in \mathbb{R}, 1 \leq l \leq L$. Assuming $(u, U) \in H = H^1(\Omega) \oplus \tilde{\mathbb{R}}^L$ and that u is a weak*

solution to

$$\nabla \cdot (\sigma \nabla u) = 0, \ \textit{in } \Omega \tag{2.20}$$

subject to the boundary conditions on $\partial\Omega$*,*

$$u + z_l \sigma \frac{\partial u}{\partial n} = U_l, \ \textit{on } e_l, 1 \leq l \leq L \tag{2.21}$$

$$\sigma \frac{\partial u}{\partial n} = 0 \ \textit{on } \partial\Omega / (\cup_{l=1}^{L} e_l) \tag{2.22}$$

$$\int_{e_l} \sigma \frac{\partial u}{\partial n} = I_l \ \textit{for } 1 \leq l \leq L \tag{2.23}$$

where $\tilde{\mathbb{R}}^L = \{v \in \mathbb{R}^L | \sum_{i=1}^{L} v_i = 0\}$*. Then for any* $(v, V) \in H$*,*

$$b((u, U), (v, V)) = \sum_{l=1}^{L} I_l V_l \tag{2.24}$$

where $b((u, U), (v, V)) = \int_\Omega \sigma \nabla u \cdot \nabla v dx + \sum_{l=1}^{L} \frac{1}{z_l} \int_{e_l} (u - U_l)(v - V_l) dS$*.*
Conversely, if $(u, U) \in H$ *satisfies (2.24) for all* $(v, V) \in H$*, then* (u, U) *also satisfies (2.20)-(2.23).*

Proof. Let $(u, U) \in H$ satisfies (2.20)-(2.23). Let us denote the test functions $v \in H^1(\Omega)$ and $V \in \tilde{\mathbb{R}}^L$. We multiply v with (2.20) and integrate over Ω to obtain

$$\int_\Omega v \nabla(\sigma \cdot \nabla u) dx = 0. \tag{2.25}$$

Applying Green's formula, we have

$$\int_\Omega \sigma \nabla u \cdot \nabla v dx - \int_{\partial\Omega} \sigma \frac{\partial u}{\partial n} v dS \quad = 0 \tag{2.26}$$

$$\implies \sum_{l=1}^{L} \int_{e_l} \frac{u - U_l}{z_l} v dS + \int_\Omega \sigma \nabla u \cdot \nabla v dx \quad = 0. \tag{2.27}$$

Here we used (2.15) and the result from (2.17), such that $\sigma \frac{\partial u}{\partial n} = \frac{u - U_l}{z_l}$ on $\partial\Omega$.

Multiplying (2.17) by the test functions $V_l \in \tilde{\mathbb{R}}^L$ and integrating over each electrode e_l, we have

$$\sum_{l=1}^{L} \frac{1}{z_l} \int_{e_l} (u - U_l) V_l dS + \sum_{l=1}^{L} V_l I_l \quad = 0. \tag{2.28}$$

Combining (2.27) and (2.28), we have

$$\sum_{l=1}^{L} \frac{1}{z_l} \int_{e_l} (u - U_l)(v - V_l) dS + \int_\Omega \sigma \nabla u \cdot \nabla v dx = \sum_{l=1}^{L} V_l I_l. \tag{2.29}$$

Defining the map $b : H \times H \to \mathbb{R}$ as

$$b((u, U), (v, V)) = \int_\Omega \sigma \nabla u \cdot \nabla v dx + \sum_{l=1}^{L} \frac{1}{z_l} \int_{e_l} (u - U_l)(v - V_l) dS. \tag{2.30}$$

Thus, the weak form of CEM is

$$b((u, U), (v, V)) = f(v, V), \text{ for all } (v, V) \in H^1(\Omega) \oplus \tilde{\mathbb{R}}^L. \tag{2.31}$$

where $f(v, V) = \sum_{l=1}^{L} I_l V_l$ is a functional that maps $H \mapsto \mathbb{R}$.

Conversely, suppose $(u, U) \in H$ satisfies (2.30) for any $(v, V) \in H$. Choosing $v \in$

$H^1(\Omega)$ and $V = 0$, then (2.30) is,

$$\int_\Omega \sigma \nabla u \cdot \nabla v dx = 0$$

Thus u is a weak solution of (2.20). Now using Green's theorem we have,

$$\begin{aligned} \int_\Omega \sigma \nabla u \cdot \nabla v dx &= \int_{\partial\Omega} \sigma \frac{\partial u}{\partial n} v dS - \int_\Omega \nabla \cdot (\sigma \nabla u) v dx \\ &= \int_{\partial\Omega} \sigma \frac{\partial u}{\partial n} v dS \end{aligned} \tag{2.32}$$

Combining this with (2.24), we have,

$$\int_{\partial\Omega} \sigma \frac{\partial u}{\partial n} v dS + \sum_{l=1}^{L} \frac{1}{z_l} \int_{e_l} (u - U_l) v dS = 0. \tag{2.33}$$

Since v is chosen as arbitrary, we can say that u must satisfies (2.21) and (2.22). Now for $v = 0$, (2.24) is,

$$-\sum_{l=1}^{L} \frac{1}{z_l} \int_{e_l} (u - U_l) V_l dS = \sum_{l=1}^{L} I_l V_l$$

Equating coefficients of V_l, we get

$$-\frac{1}{z_l} \int_{e_l} (u - U_l) V_l dS = I_l, \text{ for } 1 \leq l \leq L$$

Using this result in (2.33), we have

$$\int_{e_l} \sigma \frac{\partial u}{\partial n} v dS = I_l, 1 \leq l \leq L$$

as V_l is arbitrary. Thus u satisfies (2.23). □

2.4 Well-posedness of CEM forward solution

We define $\tilde{\mathbb{R}}^L = \{I \in \mathbb{R}^L | \sum_{l=1}^{L} I_l = 0\}$ and $H = H^1(\Omega) \oplus \tilde{\mathbb{R}}^L$. We observe that, setting $b((u,U),(u,U)) = 0$ does not give us $(u,U) = 0$, rather it gives $u = U_1 = ... = U_L =$ constant. This suggests that we have to introduce the quotient space $\dot{H} = H/\mathbb{R}$, equipped with the usual norm,

$$||(u,U)||_{\dot{H}} = \inf_{c\in\mathbb{R}} \left(||u-c||^2_{H^1(\Omega)} + ||U-c||^2_{\tilde{\mathbb{R}}^L} \right)^{1/2} \tag{2.34}$$

We want to use the Lax-Miligram theorem to show the existence and uniqueness of (u,U) satisfying CEM. We need the following results. However, to satisfy the hypotheses of the Lax-Miligram theorem, we need a different norm in $\dot{H}$ defined as,

$$||(u,U)||^2_* = ||\nabla u||^2_{L_2(\Omega)} + \sum_{l=1}^{L} ||u - U_l||^2_{L_2(e_l)}.$$

Lemma 6. *$||\cdot||_{\dot{H}}$ is equivalent to $||\cdot||_*$.*

Proof. The sketch of the proof is given in [75, 47].

Claim. There exists a constant $C > 0$ such that $||(u,U)||^2_* \leq C||(u,U)||^2_{\dot{H}}$.

For $(u,U) \in H$, we can choose $c \in \mathbb{R}$, such that

$$||u-c||^2_{H^1(\Omega)} + ||U-c||^2_{\mathbb{R}_L} \leq ||(u,U)||^2_{\dot{H}} + \varepsilon, \text{ for an arbitrary } \varepsilon > 0$$

We can rewrite the norm $||\cdot||_*$ as,

$$\begin{aligned}
||(u,U)||_*^2 &= ||\nabla(u-c)||_{L^2(\Omega)}^2 + \sum_{l=1}^{L} ||(u-c)-(U_l-c)||_{L^2(e_l)}^2 \\
&= ||\nabla(u-c)||_{L^2(\Omega)}^2 + \sum_{l=1}^{L} \int_{e_l} |(u-c)-(U_l-c)|^2 ds \\
&\leq ||\nabla(u-c)||_{L^2(\Omega)}^2 + 2\sum_{l=1}^{L} \int_{e_l} |(u-c)|^2 ds + \sum_{l=1}^{L} \int_{e_l} |(U_l-c)|^2 ds \\
&= ||\nabla(u-c)||_{L^2(\Omega)}^2 + 2\sum_{l=1}^{L} \int_{e_l} |(u-c)|^2 ds + 2\sum_{l=1}^{L} |e_l|^2 |(U_l-c)|^2.
\end{aligned}$$

We know that $H^{1/2}(\partial\Omega) \subset L^2(\Omega)$. Then using the Sobolev embedding theorem and the trace theorem [30], we have,

$$\begin{aligned}
2\sum_{l=1}^{L} \int_{e_l} |(u-c)|^2 ds &\leq 2\sum_{l=1}^{L} \int_{\partial\Omega} |(u-c)|^2 ds \\
&= 2||u-c||_{L^2(\partial\Omega)}^2 \\
&\leq C_1 ||u-c||_{H^{1/2}(\partial\Omega)}^2 \\
&\leq C_1 ||u-c||_{H^1(\Omega)}^2.
\end{aligned}$$

Using the above we have,

$$\begin{aligned}
||(u,U)||_*^2 &\leq C_1 ||u-c||_{H^1(\Omega)}^2 + C_2 |(U-c)|_{\mathbb{C}^L}^2, \text{ with } C_2 = \max_{1\leq l\leq L}\{2|e_l|\} \\
&\leq C\left(||u-c||_{H^1(\Omega)}^2 + |(U-c)|_{\mathbb{C}^L}^2\right), \text{ with } C = \max\{C_1, C_2\} \\
&= C\left(||(u,U)||_{H(\Omega)}^2 + \varepsilon\right).
\end{aligned}$$

Since $\varepsilon > 0$ is taken as arbitrary, we can say that,

$$||(u,U)||_*^2 \leq C||(u,U)||_{\dot{H}(\Omega)}^2$$

Claim. There exists a constant $c > 0$ such that $c||(u,U)||_{\dot{H}(\Omega)}^2 \leq ||(u,U)||_*^2$.

Using trace theorem and Poincare's inequality, we have

$$\begin{aligned}
||(u,U)||_{\dot{H}}^2 &= \inf_{c\in\mathbb{R}} \left(||u-c||_{H^1(\Omega)}^2 + ||U-c||_{\mathbb{R}_L}^2 \right) \\
&\leq ||\nabla(u-c)||_{L^2(\Omega)}^2 + ||(u-c)||_{L^2(\Omega)}^2 + \sum_{l=1}^{L} |U_l - c|^2, \text{ for any } c \in \mathbb{R} \\
&\leq ||\nabla(u-c)||_{L^2(\Omega)}^2 + ||(u-c)||_{L^2(\Omega)}^2 + \sum_{l=1}^{L} \frac{1}{|e_l|} ||U_l - c||_{L^2(e_l)}^2 \\
&\leq ||\nabla u||_{L^2(\Omega)}^2 + ||(u-c)||_{L^2(\Omega)}^2 + \sum_{l=1}^{L} \frac{1}{|e_l|} ||U_l - u||_{L^2(e_l)}^2 + \sum_{l=1}^{L} \frac{1}{|e_l|} ||u - c||_{L^2(e_l)}^2 \\
&\leq ||\nabla u||_{L^2(\Omega)}^2 + 2||(u-c)||_{L^2(\Omega)}^2 + \sum_{l=1}^{L} \frac{1}{|e_l|} ||U_l - u||_{L^2(e_l)}^2 \\
&\leq (1+c_1)||\nabla u||_{L^2(\Omega)}^2 + C_2 \sum_{l=1}^{L} ||U_l - u||_{L^2(e_l)}^2, \text{ with } C_2 = \max_{1\leq l\leq L} \{\frac{1}{|e_l|}\} \\
&\leq C||(u,U)||_*^2.
\end{aligned}$$

Hence the two norms are equivalent. □

Now we are ready to show that $b((u,U),(v,V))$ satisfies the hypotheses of the Lax-Miligram theorem.

Lemma 7. *$b((u,U),(v,V)) = \int_\Omega \sigma \nabla u \cdot \nabla v dx + \sum_{l=1}^{L} \frac{1}{z_l} \int_{e_l} (u - U_l)(v - V_l) dS$ is a bilinear form.*

Proof. Let $(u,U),(v,V),(w,W) \in H$ and $\lambda \in \mathbb{R}$. Then,

(i)

$$\begin{aligned} b((u+w,U+W),(v,V)) &= \int_\Omega \sigma \nabla(u+w)\cdot\nabla v dx + \sum_{l=1}^{L} \frac{1}{z_l}\int_{e_l} \left((u-U_l)+(w-W_l)\right)(v-V_l)dS \\ &= \int_\Omega \sigma \nabla u\cdot\nabla v dx + \sum_{l=1}^{L} \frac{1}{z_l}\int_{e_l} (u-U_l)(v-V_l)dS \\ &+ \int_\Omega \sigma \nabla w\cdot\nabla v dx + \sum_{l=1}^{L} \frac{1}{z_l}\int_{e_l} (W-W_l)(v-V_l)dS \\ &= b((u,U),(v,V)) + b((w,W),(v,V)) \end{aligned}$$

(ii)

$$\begin{aligned} b((u,U),(v+w,V+W)) &= \int_\Omega \sigma \nabla u\cdot\nabla (v+w) dx + \sum_{l=1}^{L} \frac{1}{z_l}\int_{e_l} (u-U_l)((v-V_l)+(w-W_l))dS \\ &= \int_\Omega \sigma \nabla u\cdot\nabla v dx + \sum_{l=1}^{L} \frac{1}{z_l}\int_{e_l} (u-U_l)(v-V_l)dS \\ &+ \int_\Omega \sigma \nabla u\cdot\nabla w dx + \sum_{l=1}^{L} \frac{1}{z_l}\int_{e_l} (u-U_l)(w-W_l)dS \\ &= b((u,U),(v,V)) + b((u,U),(w,W)) \end{aligned}$$

(iii)

$$\begin{aligned} b(\lambda(u,U),(v,V)) &= \int_\Omega \sigma \nabla \lambda u\cdot\nabla v dx + \sum_{l=1}^{L} \frac{1}{z_l}\int_{e_l} (\lambda u-\lambda U_l)(v-V_l)dS \\ &= \int_\Omega \sigma \nabla u\cdot\nabla \lambda v dx + \sum_{l=1}^{L} \frac{1}{z_l}\int_{e_l} (u-U_l)(\lambda v-\lambda V_l)dS = b((u,U),\lambda(v,V)) \\ &= \lambda\int_\Omega \sigma \nabla u\cdot\nabla v dx + \lambda\sum_{l=1}^{L} \frac{1}{z_l}\int_{e_l} (u-U_l)(v-V_l)dS = \lambda b((u,U),(v,V)) \end{aligned}$$

Hence, $b(u,v)$ is bilinear. $\square$

Lemma 8. *$b((u,U),(v,V))$ is bounded and coercive.*

Proof. We have,

$$\begin{aligned}
|b((u,U),(v,V))| &= |\int_\Omega \sigma\nabla u\cdot\nabla v dx + \sum_{l=1}^{L}\frac{1}{z_l}\int_{e_l}(u-U_l)(v-V_l)dS| \\
&\leq \sigma_2|\int_\Omega \nabla u\cdot\nabla v dx| + \sum_{l=1}^{L}\frac{1}{z_l}|\int_{e_l}(u-U_l)(v-V_l)dS| \\
&\leq \sigma_2||\nabla u||_{L^2(\Omega)}||\nabla v||_{L^2(\Omega)} + \sum_{l=1}^{L}\frac{1}{z_l}||u-U_l||_{L^2(e_l)}||v-V_l||_{L^2(e_l)} \\
&\leq C_1\left(||\nabla u||_{L^2(\Omega)}||\nabla v||_{L^2(\Omega)} + \sum_{l=1}^{L}||u-U_l||_{L^2(e_l)}||v-V_l||_{L^2(e_l)}\right) \\
&\leq C||(u,U)||_*||(v,V)||_*, \text{ for some } C>0.
\end{aligned}$$

Thus $b((u,U),(v,V))$ is bounded.

Now,

$$\begin{aligned}
|b((u,U),(u,U))| &= |\int_\Omega \sigma|\nabla u|^2 dx + \sum_{l=1}^{L}\frac{1}{z_l}\int_{e_l}(u-U_l)^2 dS| \\
&\geq \sigma_1||\nabla u||^2_{L^2(\Omega)} + \sum_{l=1}^{L}\frac{1}{z_l}||u-U_l||^2_{L^2(e_l)} \\
&\geq k||(u,U)||^2_*, \text{ for some } k>0.
\end{aligned}$$

Hence $b(u,U),(v,V))$ is coercive. $\square$

In order to apply the Lax-Miligram theorem, we need to prove the following lemma.

Lemma 9. *The mapping* $f(v,V) = \sum_{l=1}^{L} I_l V_l$, *with* $I, V \in \tilde{\mathbb{R}}^L$ *is well-defined and continuous.*

Proof. Suppose $(v,V) = (v_*, V_*) \in H(\Omega)$. Then,

$$\begin{aligned} f(v,V) &= \sum_{l-1}^{L} I_l V_l \\ &= \sum_{l-1}^{L} I_l (V_l - c), \text{ for some } c \in \mathbb{R} \text{ and using } \sum_{l-1}^{L} I_l = 0 \\ &= \sum_{l-1}^{L} I_l (V_* - c) = \sum_{l-1}^{L} I_l V_* = f(v, V_*). \end{aligned}$$

Thus $f(v,V)$ is well-defined. Now there exists a constant $c \in \mathbb{R}$ such that,

$$\left(||v-c|^2_{H^1(\Omega)} + ||V-c||^2_{\mathbb{R}^L} \right)^{1/2} \leq ||(v,V)|| + \varepsilon$$

for some $\varepsilon > 0$. Then,

$$\begin{aligned} |f(v,V)| &= \sum_{l-1}^{L} I_l (V_l - \text{constant}) \\ &\leq ||I||^2_{\mathbb{R}^L} ||V_l - \text{constant}||^2_{\mathbb{R}^L} \\ &\leq ||I||^2_{\mathbb{R}^L} \left(||(v,V)|| + \varepsilon \right). \end{aligned}$$

Hence $f(v,V)$ is continuous. □

Using lemma 7-9, we conclude that the weak formulation of the CEM satisfies all the hypotheses of Lax-Miligram theorem. Hence it has a unique solution.

2.5 Fréchet differentiability of the CEM operator

For the inversion procedure and implementing IRGN method, we need to compute the jacobian of the forward operator, $F(\sigma)$, required for carrying out the numerical computation using iterative Newton methods. First we linearize the forward model by replacing σ, u and U in (2.20 - 2.23) by $(\sigma+\eta)$, $(u+w)$ and (U_l+W_l), respectively, and denote the linearized operator by $F'(\sigma)$. Here η is an arbitrary direction of σ with $\eta|_{\partial\Omega} = 0$, $(w, W) \in H(\Omega)$. Then ignoring the higher order terms, we arrive at,

$$-\nabla \cdot (\sigma \nabla w) = \nabla \cdot (\eta \nabla u) \text{ in } \Omega \tag{2.35}$$

$$w + z_l \sigma \frac{\partial w}{\partial n} = W_l, \text{ on } e_l, l = 1, 2, ..., L \tag{2.36}$$

$$\int_{e_l} \sigma \frac{\partial w}{\partial n} ds = 0, \text{ for } l = 1, 2, ..., L \tag{2.37}$$

$$\sigma \frac{\partial w}{\partial n} = 0, \text{ on } \partial\Omega/(\cup_{l=1}^{L} e_l). \tag{2.38}$$

If the regularity assumptions on the domain and the coefficients are satisfied, the forward operator is differentiable, established by the following theorem, [56].

Theorem 3. *Let I be a fixed current vector and $z_l, l = 1, ..., L$ be fixed positive contact impedances. The operator F that maps $\sigma \in int(\mathcal{A})$ to the solution $(u, U) \in H$ of the forward problem, is Fréchet differentiable. If $\eta \in L^\infty(\Omega) = \{v(x) : \sup_{x\in\Omega} |v(x)| < \infty\}$, such that $\sigma + \eta \in \mathcal{A}$, then the derivative $F'(\sigma)\eta = (w, W) \in H$ satisfies the following variational problem,*

$$b((w, W), (v, V)) = -\int_\Omega \eta \nabla u \cdot \nabla v dx \tag{2.39}$$

for all $(v, V) \in H$, where $(u, U) = F(\sigma)$.

Proof. The proof of the above theorem is well established in the literature, see, [56, 49]. □

The above theorem establishes the differentialbility of the forward CEM operator $F(\sigma)$. We denote the derivative operator as $F'(\sigma)$, and the matrix, called the jacobian of $F(\sigma)$, [56, 68]. Let $\nabla_t F(\sigma)$ be the gradient of $F(\sigma)$ with respect to the t-th component of $\sigma \in Q_h$. Then $F'(\sigma)$ has the form,

$$F'(\sigma) = \begin{pmatrix} \nabla_1 F(\sigma) \\ \nabla_2 F(\sigma) \\ \vdots \\ \nabla_{|T|} F(\sigma) \end{pmatrix} \in \mathbb{R}^{|T| \times LP}$$

We denote, $\nabla_t F(\sigma) = (U_t^1, U_t^2, \ldots, U_t^L) \in \mathbb{R}^{LP}$, then we can compute the vectors $U_t^m \in \tilde{\mathbb{R}}^L$, as part of the solution (u_t^m, U_t^m) of the variational problem (2.39).

Chapter 3

Diffuse Optical Tomography

Diffuse Optical Tomography (DOT) is a non-invasive technique that utilize light in the near infrared spectral region to measure the optical properties of physiological tissue. This technique requires the object being imaged to be least partially light-transmitting or translucent, so it works best on soft tissues, such as breast and brain tissues. By monitoring spatial-temporal variations in the light absorption and scattering properties of tissue, regional variations in oxy- and deoxy-hemoglobin concentration as well as cellular scattering can be imaged. Based on these measurements, spatial maps of tissue properties such as total hemoglobin concentration, blood oxygen saturation and scattering can be obtained using model-based reconstruction algorithms. DOT has been applied in various deep-tissue applications including breast cancer imaging [45, 27, 67, 28], brain functional imaging [34, 86, 55, 32, 80, 81, 82], stroke detection [53], arthritic finger [39] etc.

In a typical DOT experiment, an optical wave from a light source is projected onto the body. Usually, this is a laser light in the visible (about 400 to 700nm), or near

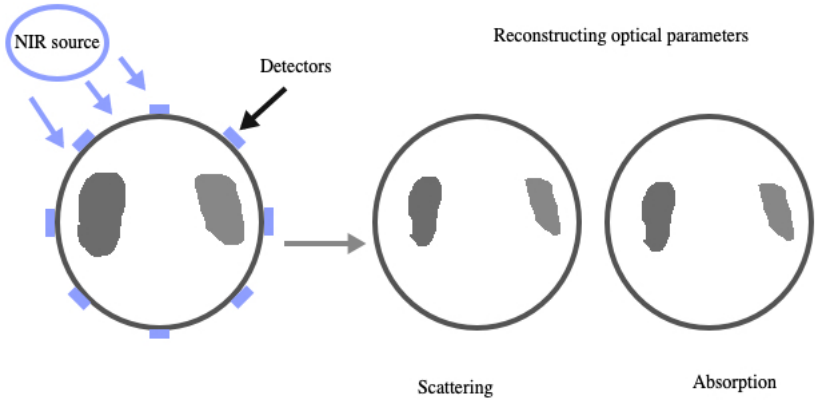

Figure 3.1: DOT experiment

infrared range (about 700 to 1600nm). Due to scattering properties of tissues, some of the light beam is absorbed by chromophores (such as hemoglobin, lipid and water) inside the tissue, and the rest is scattered. To collect this scattered beam, multiple detectors are placed on the boundary of the tissue, as shown in figure 3.1. From this data a 2-D image (slice) of the tissue is reconstructed in the form of a spatial map of the tissue's absorption and scattering coefficients [45]. Since cells in tumors have higher absorption coefficients than normal cells due to an increased water or ionic concentration, and they also scatter photons differently, the absorption and scattering coefficients of the cells being imaged are the most important parameters to be determined in most medical applications [45, 85].

Given a light source f on the boundary and the absorption and scattering coefficients μ_a and μ_s, respectively, for all locations $x \in \Omega$, the forward problem in DOT is to determine the measurements g on the boundary $\partial\Omega$ of Ω. The relationship between these variables is most often described using the radiative transport equation (RTE), [2, 16, 22, 33, 78].

$$\frac{1}{c}\frac{\partial \tilde{I}}{\partial t} + \hat{s}\cdot\nabla\tilde{I} + (\mu_a + \mu_s)\tilde{I} = \mu_s \int p(\hat{s}', \hat{s})\tilde{I}(x, \hat{s}')d\hat{s}' \tag{3.1}$$

where $\tilde{I}(x, \hat{s}, t)$, the variable of interest, is the specific intensity, also known as the spectral radiance (number of photons per unit volume), at position x, in the direction $\hat{s}$ at time t [4].

However, the RTE is computationally expensive and in practice, researchers use an approximation equation to RTE with Robin boundary equation [38]. The most common approximation is the diffusion approximation, which results in a modality known as diffuse optical tomography (DOT).

$$\nabla - \cdot(D\nabla u) + (\mu_a + ik)u = h, \text{ in } \Omega \tag{3.2}$$

where u is the photon density, h is the source, D is the diffusion coefficient, expressed as $D = \frac{1}{3(\mu_a+\mu_s')}$, where μ_a is the absorption coefficient and μ_s' is the reduced scattering coefficient. In practice, source cannot be placed inside he body, so in this dissertation we set $h = 0$. The diffusion model is a first order approximation to the radiative transport equation, assuming $\mu_s' >> \mu_a$and the detector and source are not too close together [4, 45].

As the previous chapter, in this chapter we discuss the well-posedness of the DOT forward problem and the existence and uniqueness of it's solution.

3.1 The DOT forward problem

The DOT forward problem involves solving an elliptic partial differential equation with Robin boundary conditions where μ_a and D are known. The solution u describes the photon density of the scattered light arriving at the detectors. The complete DOT

experiment is given in the frequency domain, with Robin boundary condition

$$-\nabla \cdot (D\nabla u) + (\mu_a + ik)u = 0 \text{ in } \Omega \tag{3.3}$$

$$\gamma_R u = u + 2D\frac{\partial u}{\partial n} = f \text{ on } \partial\Omega \tag{3.4}$$

here, D is the diffusion coefficient, μ_a is the absorption coefficient, $k = \omega/c$ is the imaginary wave number, ω is the modulation frequency of the laser, c is the speed of light, f is the source, and $\gamma_R : H^1(\Omega) \to H^{-1/2}(\partial\Omega)$ is the Robin trace map, with the solution space defined as, $H^1(\Omega) = \{v \in L^2(\Omega) | \int_\Omega (|\nabla v|^2 + v^2)dx < \infty\}$ and $H^{1/2}(\partial\Omega) \simeq \{\gamma_D(v) | v \in H^1(\Omega)/H_0^1(\Omega)\}$. We also consider $\Omega \subset \mathbb{R}^n$, $n = 2, 3$ a bounded, connected Lipschitz domain. Furthermore, the DOT model with Neumann boundary condition is given by,

$$-\nabla \cdot (D\nabla u) + (\mu_a + ik)u = 0, \text{ in } \Omega \tag{3.5}$$

$$\gamma_N u = -D\frac{\partial u}{\partial n} = g, \text{ on } \partial\Omega \tag{3.6}$$

where g the measurements of the scattered photons on the boundary, and $\gamma_N : H^1(\Omega) \to H^{-1/2}(\partial\Omega)$ is the Neumann trace map, with $H^{-1/2}(\partial\Omega) \simeq \{\gamma_N(v) | v \in H^1(\Omega)/H_0^1(\Omega)\}$. Note that, $H_0^1(\Omega) = \{v \in H^1 | \int_{\partial\Omega} v ds = 0\}$. For the well-posedness, we need D, μ_a to be bounded. That is there exists constants D_0, D_1 and μ_0, μ_1 such that,

$$0 < D_0 \leq D \leq D_1 < \infty, \quad 0 < \mu_0 \leq \mu_a \leq \mu_1 < \infty \tag{3.7}$$

Thus we can define the parameter space for DOT as,

$\tilde{Q} := \{(D, \mu_a) \in L^\infty(\Omega) \times L^\infty(\Omega) : 0 < D_0 < D < D_1 \;\; 0 < \mu_0 < \mu_1 < \mu_1\}$

We note that $H_0^1(\Omega) \hookrightarrow H^1(\Omega) \hookrightarrow L^2(\Omega)$ is the dual space of $H^{1/2}(\partial\Omega)$. In general, these spaces are known as Sobolev spaces. The Sobolev space $W_p^k(\Omega)$ is formally

defined as

$$W_p^m(\Omega) = \{u \in L^p(\Omega) | D^\alpha u \in L^p(\Omega), \forall |\alpha| \leq m\}.$$

That is $W_p^k(\Omega)$ is the set of all functions in $L^p(\Omega)$ whose $|\alpha| \leq m$ weak partial derivatives are also in $L^p(\Omega)$. It is convenient to let $W_2^m(\Omega) = H^m(\Omega)$, which we adopt here.

3.2 Well-posedness of the DOT problem (Robin boundary condition)

Consider the Robin problem described in (3.3) - (3.4).

$$\begin{aligned} -\nabla \cdot (D\nabla u) + (\mu_a + ik)u &= 0 \text{ in } \Omega \\ \gamma_R u = u + 2D\frac{\partial u}{\partial n} &= f \text{ on } \partial\Omega \end{aligned}$$

where $u \in H^1(\Omega)$, $g \in H^{1/2}(\partial\Omega)$ and $q = (D, \mu_a) \in \bar{Q}$, as described before. To discuss the well-posedness of the Robin problem, first we derive the weak formulation.
For any test function $v \in H^1(\Omega)$, we have

$$\begin{aligned} & -\int_\Omega \nabla \cdot (D\nabla u)\bar{v}dx + \int_\Omega (\mu_a + ik)u\bar{v})dx = 0 \\ \implies & \int_\Omega D\nabla u \cdot \nabla \bar{v}dx + \int_\Omega (\mu_a + ik)dxu\bar{v} - \int_{\partial\Omega} D\frac{\partial u}{\partial n}\bar{v}ds = 0 \end{aligned}$$

where $\bar{v}$ represents the complex conjugate of v. Now using the boundary condition (3.4), we get

$$\int_\Omega D\nabla u \cdot \nabla \bar{v} dx + \int_\Omega (\mu_a + ik) dx = \frac{1}{2} \int_{\partial\Omega} (g - u)\bar{v} ds$$

$$\implies \int_\Omega D\nabla u \cdot \nabla v dx + \int_\Omega (\mu_a + ik) dx + \frac{1}{2} \int_{\partial\Omega} u\bar{v} ds = \frac{1}{2} \int_{\partial\Omega} g\bar{v} ds \tag{3.8}$$

Defining $B(u, v) = \int_\Omega D\nabla u \cdot \nabla v dx + \int_\Omega (\mu_a + ik) u\bar{v} dx + \frac{1}{2} \int_{\partial\Omega} u\bar{v} ds$ and $f_R(v) = \frac{1}{2} \int_{\partial\Omega} g\bar{v} ds$, we have the weak formulation of the robin problem as,

$$B(u, v) = f_R(v), \text{ for any } u, v \in H^1(\Omega).$$

Recall the definition of a sesquilinear form.

Definition 3. *(Sesquilinear form) A map $b : V \times V \to \mathbb{C}$, is called a sesquilinear form, if it satisfies the following conditions,*

(i) $b(x + y, z + w) = b(x, z) + b(y, z) + b(x, w) + b(y, w)$,

(ii) $b(c_1 x, c_2 y) = c_1 \bar{c_2} b(x, y)$

where $x, y, z, w \in V$ and $c_1, c_2 \in \mathbb{C}$.

Lemma 10. *$B(u, v) = \int_\Omega D\nabla u \cdot \nabla \bar{v} dx + \int_\Omega (\mu_a + ik) u\bar{v} dx + \frac{1}{2} \int_{\partial\Omega} u\bar{v} ds$ is a sesquilinear form.*

Proof. (i) For any $u, v, w, z \in H^1(\Omega)$, we have

$$\begin{aligned}
B(u+v, z+w) &= \int_\Omega D\nabla(u+v)\cdot\nabla(\bar{z}+\bar{w})dx + \int_\Omega(\mu_a+ik)(u+v)(\bar{z}+\bar{w})dx \\
&\quad + \frac{1}{2}\int_{\partial\Omega}(u+v)(\bar{z}+\bar{w})ds \\
&= \int_\Omega D\nabla u\cdot\nabla\bar{z}dx + \int_\Omega(\mu_a+ik)u\bar{z}dx + \frac{1}{2}\int_{\partial\Omega}u\bar{z}ds \\
&\quad + \int_\Omega D\nabla u\cdot\nabla\bar{w}dx + \int_\Omega(\mu_a+ik)u\bar{w}dx + \frac{1}{2}\int_{\partial\Omega}u\bar{w}ds \\
&\quad + \int_\Omega D\nabla v\cdot\nabla\bar{z}dx + \int_\Omega(\mu_a+ik)v\bar{z}dx + \frac{1}{2}\int_{\partial\Omega}v\bar{z}ds \\
&\quad + \int_\Omega D\nabla v\cdot\nabla\bar{w}dx + \int_\Omega(\mu_a+ik)v\bar{w}dx + \frac{1}{2}\int_{\partial\Omega}v\bar{w}ds \\
&= B(u,z) + B(u,w) + B(v,z) + B(v,w).
\end{aligned}$$

(ii) For any $c_1, c_2 \in \mathbb{C}$, we have,

$$\begin{aligned}
B(c_1u, c_2v) &= \int_\Omega D\nabla c_1u\cdot\nabla\bar{c_2}vdx + \int_\Omega(\mu_a+ik)c_1u\bar{c_2}vdx + \frac{1}{2}\int_{\partial\Omega}c_1u\bar{c_2}vds \\
&= c_1\bar{c_2}\left(\int_\Omega D\nabla u\cdot\nabla\bar{v}dx + \int_\Omega(\mu_a+ik)u\bar{v}dx + c_1\bar{c_2}\frac{1}{2}\int_{\partial\Omega}u\bar{v}ds\right) \\
&= c_1\bar{c_2}B(u,v).
\end{aligned}$$

Hence $B(u,v)$ is a sesquilinear form. □

We will use the Lax-Milgram theorem for sesquilinear form to show the existence and uniqueness of the solution to the robin problem. The inner product for the space $H^1(\Omega)$ is

$$\langle u, v\rangle_{H^1(\Omega)} = \int_\Omega(\nabla u\cdot\nabla\overline{v} + u\overline{v})dx. \tag{3.9}$$

In order to show the boundedness and coerciveness of $b(u, v)$, it is convenient to define an equivalent norm for the space $H^1(\Omega) \times H^1(\Omega)$ as,

$$||u||_*^2 = \int_\Omega D|\nabla u|^2 dx + \int_\Omega \mu_a |u|^2 dx + \frac{1}{2}\int_{\partial\Omega} |u|^2 ds$$

Lemma 11. *$||u||_{H^1}$ and $||U||_*$ are equivalent.*

Proof.

$$\begin{aligned}
||u||_{H^1}^2 &= \int_\Omega |\nabla u|^2 + |u|^2 dx \\
&\leq \int_\Omega \frac{D(x)}{D_0}|\nabla u|^2 + \frac{\mu_a(x)}{\mu_0}|u|^2 dx \\
&= \frac{1}{D_0}\int_\Omega D|\nabla u|^2 dx + \frac{1}{\mu_0}\int_\Omega \mu_a |u|^2 dx \\
&\leq \max\{\frac{1}{D_0}, \frac{1}{\mu_0}\}\left(\int_\Omega D|\nabla u|^2 + \mu_a|u|^2 dx + \frac{1}{2}\int_{\partial\Omega}|u|^2 ds\right) \\
&\leq C_1 ||u||_*^2
\end{aligned}$$

where $C_1 = \max\{\frac{1}{D_0}, \frac{1}{\mu_0}\}$. Now

$$\begin{aligned}
||u||_*^2 &= \int_\Omega D|\nabla u|^2 dx + \int_\Omega \mu_a |u|^2 dx + \frac{1}{2}\int_{\partial\Omega}|u|^2 ds \\
&\leq D_1 \int_\Omega |\nabla u|^2 dx + \mu_1 \int_\Omega |u|^2 dx + \frac{1}{2}\int_{\partial\Omega}|u|^2 ds \\
&\leq \max\{D_1, \mu_1\}\left(\int_\Omega |\nabla u|^2 dx + \mu_1 \int_\Omega |u|^2 dx\right) + c(\Omega)\int_\Omega |\nabla u|^2 dx, \text{ using Sobolev Trace theorem} \\
&\leq \max\{D_1 + c(\Omega), \mu_1\}\left(\int_\Omega |\nabla u|^2 dx + \mu_1 \int_\Omega |u|^2 dx\right) \\
&= C_2 ||u||_{H^1}^2
\end{aligned}$$

where $C_2 = \max\{D_1 + c(\Omega), \mu_1\}$. Hence the proof. □

Lemma 12. *$B(u,v)$ is bounded and coercive.*

Proof. We will use Cauchy-Schwartz inequality to prove this.

$$\begin{aligned}
|B(u,v)| &= |\int_\Omega D\nabla u\nabla\bar{v}dx + \int_\Omega \mu_a u\bar{v}dx + \int_{\partial\Omega}\frac{1}{2}u\bar{v}ds| \\
&\leq \left(\int_\Omega |D\nabla u|^2dx\right)^{1/2}\left(\int_\Omega |\nabla v|^2dx\right)^{1/2} + \left(\int_\Omega |\mu_a u|^2dx\right)^{1/2}\left(\int_\Omega |v|^2dx\right)^{1/2} \\
&+ \frac{1}{2}\left(\int_{\partial\Omega}|u|^2ds\right)^{1/2}\left(\int_{\partial\Omega}|v|^2ds\right)^{1/2} \\
&\leq D_1\left(\int_\Omega |\nabla u|^2dx\right)^{1/2}\left(\int_\Omega |\nabla v|^2dx\right)^{1/2} + \mu_1\left(\int_\Omega |u|^2dx\right)^{1/2}\left(\int_\Omega |v|^2dx\right)^{1/2} \\
&+ \frac{c_1}{2}\left(\int_\Omega |\nabla u|^2dx\right)^{1/2}\left(\int_\Omega |\nabla v|^2dx\right)^{1/2}, \text{ using Sobolev Trace theorem} \\
&\leq C\left(\left(\int_\Omega |\nabla u|^2dx\right)^{1/2}\left(\int_\Omega |\nabla v|^2dx\right)^{1/2} + \left(\int_\Omega |u|^2dx\right)^{1/2}\left(\int_\Omega |v|^2dx\right)^{1/2}\right) \\
&\leq C||u||_{H^1(\Omega)}||v||_{H^1(\Omega)}
\end{aligned}$$

where $C = \max\{D_1 + \frac{c_2}{2} + \mu_1\}$. Hence $B(u,v)$ is bounded. Next We need to show $B(u,v)$ is coercive.

$$\begin{aligned}
|B(u,u)| &\geq |Re(B(u,u)| \\
&\geq |\int_\Omega D|\nabla u|^2dx + \int_\Omega \mu_a|u|^2dx + \int_{\partial\Omega}\frac{1}{2}|u|^2ds| \\
&= ||u||_*^2.
\end{aligned}$$

Hence $B(u,v)$ is coercive. □

To satisfy all the hypotheses of the Lax-Miligram theorem, we need to show that $f(v) = \frac{1}{2}\int_{\partial\Omega} g\bar{v}ds$ is a bounded linear functional.

Lemma 13. *$f_R(v)$ is a bounded linear functional.*

Proof. Clearly, $f_R(v)$ is linear. We have the duality pairing,

$$f_R(v) = \langle g, v \rangle_{H^{-1/2}(\partial\Omega)\times H^{1/2}(\partial\Omega)}$$

By Riesz representation theorem, there exists a bounded linear operator $S : H^{-1/2} \mapsto H^{1/2}$, such that,

$$\begin{aligned} |\langle g, v \rangle_{H^{-1/2}(\partial\Omega)\times H^{1/2}(\partial\Omega)}| &= |\langle Sg, v \rangle_{H^{1/2}(\partial\Omega)\times H^{1/2}(\partial\Omega)}| \\ &\leq ||Sg||_{H^1(\Omega)}||v||_{H^1(\Omega)} \\ &\leq c||v||_{H^1(\Omega)}, \text{ using boundedness of } S. \end{aligned}$$

Thus $f_R(v)$ is a bounded linear operator. □

From Lemma 12-13, we have that the hypotheses of the generalized Lax-Miligram theorem are satisfied. So we can conclude that the there exists a unique solution of (3.3)-(3.4).

3.3 Fréchet differentiability of the DOT operator

The inverse problem of the DOT problem is to estimate the diffusion (D) and the absorption (μ) coefficient for a source function f. We solve the inverse problem using iteratively regularized Gauss-Newton (IRGN) method, for which a Fréchet differentiablity of the map $\gamma_0 F_N^{(k,q^\dagger)}(0, f)$ is a necessary tool. Recall that Fréchet differentia-

bility of $\gamma_0 F_N^{(k,q^\dagger)}(0,f)$ is defined as

$$\lim_{||\eta||_\infty \to 0} \frac{||\gamma_0 F_N^{(k,q^\dagger)}(q+\eta:0,f) - \gamma_0 F_N^{(k,q^\dagger)}(q:0,f) - \gamma_0 {F'_N}^{(k,q^\dagger)}(q:0,f)\eta||}{||\eta||_\infty} = 0$$

Theorem 4. *Suppose $q_1 = (D_1, \mu_1), q_2 = (D_2, \mu_2)$ are two pairs of real-valued $L_\infty(\Omega)$ functions satisfying,*

$$0 < m_D \leq D_{1,2}(x) \leq M_D, \quad 0 \leq \mu_{1,2}(x) \leq M_\mu, \qquad \textit{for some } m_D, M_D, M_\mu > 0$$

then there exists a constant C, such that,

$$||\gamma_0 F_N^{(k,q^\dagger)}(q_2:0,f) - \gamma_0 F_N^{(k,q^\dagger)}(q_1:0,f) - \gamma_0 {F'_N}^{(k,q^\dagger)}(q_1:0,f)\eta|| \leq C||\eta||_\infty^2 \quad (3.10)$$

where $\eta = q_2 - q_1$. In particular, $\gamma_0 {F'_N}^{(k,q^\dagger)}(q_1 : 0, f)$ is the Fréchet derivative of $\gamma_0 F_N^{(k,q^\dagger)}(0,f)$ with respect to q at q_1.

Proof. See [63]. □

Chapter 4

Inverse Problem for EIT and DOT

Inverse problems are important because of their abundance in application. Many of the problems we encounter in daily life are inverse problems: given an observed or desired effect, what was the original cause? Mathematically, we represent a general inverse problem with the equation $F(x) = y$, where the output y is known, as well as the transformation function F, but the input data x are unknown. Such problems are relatively straight forward mathematically if F has an inverse. However as mathematicians know, inverse often do not exist or can only be approximated numerically. In addition such inverses are very unstable in the sense that a small change to the input data can lead to a large change in the output. Another way to say this is that inverse problems are often sensitive, they do not depend continuously on the data, violating the third condition of Hadamard (see Definition 1) and thus are ill posed. Inverse problems arise naturally in medical imaging as the unknowns are the geometry and physiological properties of the tissue being imaged. In the case of optical imaging like DOT, as well as in EIT, the "output data" y is the data about the scattered

photons read by the detectors at the boundary of the tissue. Due to the sensitivity of the unknown parameter values to small perturbations in the data measurements at the boundary, these problems are ill-posed and can only be solved through numerical optimization. Further due to sensitivity of the solution regularization is needed.
In this chapter, we discuss the existence and uniqueness of the inverse problems for EIT and DOT.

4.1 Inverse problem for EIT

In EIT, the conductivity distribution $\sigma \in \Omega$ is unknown, and the inverse problem is to reconstruct σ from simultaneous measurements of boundary voltages V given the corresponding current densities I. The Dirichlet EIT forward problem is to find $u \in H^1(\Omega)$ for a given $\sigma \in L^\infty(\Omega)$. Then the Dirichlet-to-Neumann (DtN) map is defined as the operator $\wedge_\sigma : H^{1/2}(\partial\Omega) \to H^{-1/2}(\partial\Omega)$ given by,

$$u \mapsto \sigma \frac{\partial u}{\partial n} \text{ on } \partial\Omega.$$

Theoretically, we want to determine σ from the knowledge of the DtN map. However, in practice, the reconstruction is done with the partially known DtN map. In chapter 2, we have shown the well-posedness of the EIT forward problem. But, unlike the EIT forward problem, the inverse problem is highly ill-posed, i.e., small perturbation in the measurement can lead to highly different solutions in the parameter space of σ. In this section, we discuss the existence and uniqueness of the solution to the inverse EIT problem with the assumption that we have a complete knowledge of the DtN map.

4.1.1 Existence and uniqueness of the inverse EIT solution

In this section, we discuss the existence and uniqueness of the inverse EIT problem. For that, we need more smoothness for the parameter σ in the parameter space. We consider $\sigma \in \{H^2(\Omega) : 0 < \sigma_1 < \sigma < \sigma_2 < \infty\}$. We will establish the uniqueness by converting the governing equation into a Schrödinger type equation using a Liouville transformation by setting $w = \sqrt{\sigma}u$. Using this transformation into (2.3) we have,

$$\begin{aligned}
0 &= \nabla \cdot (\sigma \nabla u) \\
&= \nabla \cdot \left(\sigma \nabla \left(\frac{w}{\sqrt{\sigma}} \right) \right) \\
&= \sigma \triangle \left(\frac{w}{\sqrt{\sigma}} \right) + \nabla \left(\frac{w}{\sqrt{\sigma}} \right) \cdot \nabla \sigma \\
&= \sigma \triangle \left(\frac{w}{\sqrt{\sigma}} \right) + 2\sqrt{\sigma} \left(\nabla \left(\frac{w}{\sqrt{\sigma}} \right) \cdot \nabla \sqrt{\sigma} \right), \text{ using product rule} \\
&= \sigma \triangle u + 2\sqrt{\sigma} \nabla u \cdot \nabla \sqrt{\sigma} \\
&= \sqrt{\sigma} \triangle u + 2 \nabla u \cdot \nabla \sqrt{\sigma}, \text{ as } 0 < \sigma_1 < \sigma
\end{aligned} \tag{4.1}$$

Now

$$\begin{aligned}
\triangle w &= \nabla \cdot \nabla (\sqrt{\sigma} u) \\
&= \nabla \cdot \left(\sqrt{\sigma} \nabla u + u \nabla \sqrt{\sigma} \right) \\
&= \sqrt{\sigma} \triangle u + 2 \nabla u \cdot \nabla \sqrt{\sigma} + u \triangle \sqrt{\sigma} \\
&= u \triangle \sqrt{\sigma} \\
\implies \triangle w - w \left(\frac{\triangle \sqrt{\sigma}}{\sqrt{\sigma}} \right) &= 0
\end{aligned}$$

which is a Schrödinger type equation. Similarly, we want to find the Dirichlet and Neumann boundary conditions w.r.t. w. Consider,

$$w = \hat{g}, \text{ on } \partial\Omega$$
$$\frac{\partial w}{\partial n} = \hat{f}, \text{ on } \partial\Omega$$

Then using the transformation above and the boundary conditions described in (2.4) and (2.1), we have

$$u = \frac{w}{\sqrt{\sigma}} = \frac{\hat{g}}{\sqrt{\sigma}} = g, \text{ on } \partial\Omega$$
$$\sigma\frac{\partial u}{\partial n} = \sigma\frac{\partial}{\partial n}\left(\frac{w}{\sqrt{\sigma}}\right) = \sigma w\frac{\partial \sigma^{-1/2}}{\partial n} + \sqrt{\sigma}\frac{\partial w}{\partial n} = \sigma\hat{g}\frac{\partial \sigma^{-1/2}}{\partial n} + \sqrt{\sigma}\hat{f} = f, \text{ on } \partial\Omega$$

In matrix form we have,

$$\begin{bmatrix} \frac{1}{\sqrt{\sigma}} & 0 \\ \sigma\frac{\partial\sigma^{-1/2}}{\partial n} & \sqrt{\sigma} \end{bmatrix}\begin{bmatrix} \hat{g} \\ \hat{f} \end{bmatrix} = \begin{bmatrix} g \\ f \end{bmatrix}.$$

The system above has a unique solution. Hence one can easily convert the Dirichlet and Neumann problem into a Schrödinger type equation. Therefore the inverse EIT problem has a unique solution as Schrödinger equation has a unique solution.

4.1.2 Cost functional for EIT

Unlike the forward problem, the inverse problem suffers from ill-posedness due to the partial knowledge of the DtN map from using N number of experiments. Hence one

has to consider minimization of the following regularized functional,

$$J_\lambda(\sigma) = \frac{1}{2}||\Gamma_D F_N(u) - g^\delta||^2_{L^2(\Omega)} + \lambda R_p(\sigma - \sigma_b) \tag{4.2}$$

where, σ_b is the background conductivity, λ is the regularization parameter, g^δ is the noisy measurement or data and $R_p(\cdot)$ is a penalty term which is set as $R_p(\sigma - \sigma_b) = \frac{1}{p}||\sigma - \sigma_b||^p_{L^p(\Omega)}$. The penalty term is convex and weakly lower semi-continuous, [47]. In this dissertation we consider $p = 2$, which is the most widely used classical smoothing penalty, known as the Tikhonov regularization. The minimization of (4.2), is also studied for total variation (TV) and Mumford-Shah penalty in [70, 71]. The existence of the minimizer of (4.2) is established in the following theorem, [47].

Theorem 5. *There exists a minimizer σ_λ to $J_\lambda(\sigma)$ over the admissible space $\mathcal{A} = \{\sigma \in L^\infty : 0 < \sigma_1 < \sigma < \sigma_2 < \infty\}$. Let $g_n \subset L^2(\Omega)$ be a sequence of noisy data converging to g^δ, and σ_n is the minimizer corresponding to g_n. Then the sequence σ_n has a subsequence converging in $H^1(\Omega')$ to a minimizer of J_λ. Moreover if $\lambda = \lambda(\delta)$ satisfies $\lim_{\delta\to 0} \lambda(\delta) = 0$ and $\lim_{\delta\to 0} \frac{\sigma^2}{\lambda(\delta)} = 0$, then the sequence of minimizers $\{\sigma_n\}$ has a subsequence converges in $H^1(\Omega')$ to an $R_p(\cdot)$ minimizing solution σ_λ as $\delta \to 0$. Furthermore if σ^T is unique then the whole sequence converges.*

Proof. Sketch of the proof is given in [47, 40]. □

4.2 Inverse problem for DOT

In diffuse optical tomography(DOT), a light source of near-infrared range is projected on the tissue. This interacts with the tissue primarily through the scattering and

absorption coefficients of the photons.

This interaction is modeled in chapter 3, in the time independent (or dc) case, by the diffusion approximation

$$-\nabla \cdot (D\nabla u) + \mu_a u = 0 \quad \text{in } \Omega \tag{4.3}$$

$$u + 2D\frac{\partial u}{\partial n} = f \quad \text{on } \partial\Omega \tag{4.4}$$

In [3], the authors showed that the unique recovery diffusion and absorption coefficients can not occur simultaneously.

We want to reconstruct a spatial map of the optical parameters D and μ_a, given the information of scattered photons collected at the detectors placed on the boundary of the medium. Thus the inverse problem can be stated as: given data g on $\partial\Omega$ find $q = (D, \mu_a)$.

In other words, we wish to find $\tilde{q} = (D, \mu_a)$, such that $\tilde{F}(\tilde{q}) = g$, and $||g - g^\delta|| \leq \delta$, where g is the measured data for $\tilde{q}$ obtained by using the forward operator $\tilde{F}$ and g^δ, is the perturbed measurement from the data given by,

$$g^\delta = \gamma_N \tilde{F}(q*) + \varepsilon$$

where γ_N is the Neumann trace, $q* = (D^*, \mu_a^*)$ are the true optical parameters, ε is the data noise, and δ is an upper bound of the noise. This problem is nonlinear and unstable [52, 5], and ill-posed [4, 64] since it is under-determined for a finite set of data.

We will denote $\tilde{q} = (D, \mu_a)$ to represent the values of the optical parameters, and $\tilde{q}_b = (D_b, \mu_b)$ to represent their values on a homogeneous background representing

healthy tissue. Thus, in the image reconstruction problem, we would like to determine $\tilde{q}$ knowing the complete Robin to Neumann map given by,

$$-\nabla \cdot (D\nabla u) + \mu_a u = 0 \text{ in } \Omega \tag{4.5}$$

$$u + 2D\frac{\partial u}{\partial n} = f \text{ on } \partial\Omega \tag{4.6}$$

$$-D\frac{\partial u}{\partial n} = g \text{ on } \partial\Omega \tag{4.7}$$

4.2.1 Existence and uniqueness of the inverse DOT solution

Due to the well-posedness of the forward problem of DOT, it was sufficient to consider $\tilde{q} \in \tilde{Q}$. However more smoothness in the parameter space is needed to prove the uniqueness of the solution to the inverse problem. Thus we will consider $\tilde{q} \in \{H^2(\Omega) \times L^\infty(\Omega), 0 < D_0 \leq D \leq D_1 < \infty, 0 < \mu_0 \leq \mu_a \leq \mu_1 < \infty\}$. Given the higher regularity it can be shown that Hadamard's first two conditions for well-posedness are met.

In this section, we discuss the existence and uniqueness of the inverse DOT problem. We will establish the uniqueness by converting the governing equation into a Schrödinger type equation with the knowledge of Dirichlet to Neumann pairs instead of Robin to Neumann pairs. Using the Liouville transformation by setting $w = \sqrt{D}u$

in (4.5) we have,

$$
\begin{aligned}
0 &= -\nabla \cdot \left(D\nabla \left(\frac{w}{\sqrt{D}} \right) \right) + (\mu_a + ik)\frac{w}{\sqrt{D}} \\
&= -D\triangle \left(\frac{w}{\sqrt{D}} \right) - \nabla \left(\frac{w}{\sqrt{D}} \right) \cdot \nabla D + (\mu_a + ik)\frac{w}{\sqrt{D}} \\
&= -D\triangle \left(\frac{w}{\sqrt{D}} \right) - 2\sqrt{D} \left(\nabla \left(\frac{w}{\sqrt{D}} \right) \cdot \nabla \sqrt{D} \right) + (\mu_a + ik)\frac{w}{\sqrt{D}}, \text{ using product rule} \\
&= -D\triangle u - 2\sqrt{D} \left(\nabla u \cdot \nabla \sqrt{D} \right) + (\mu_a + ik)u \\
&= -\sqrt{D}\triangle u - 2\nabla u \cdot \nabla \sqrt{D} + (\mu_a + ik)u. \qquad (4.8)
\end{aligned}
$$

Now

$$
\begin{aligned}
\triangle w &= \nabla \cdot \nabla(\sqrt{D}u) \\
&= \nabla \cdot \left(\sqrt{D}\nabla u + u\nabla \sqrt{D} \right) \\
&= \sqrt{D}\triangle u + 2\nabla u \cdot \nabla \sqrt{D} + u\triangle \sqrt{D} \\
\implies \triangle w - w \left(\frac{\triangle \sqrt{D}}{\sqrt{D}} \right) &= \sqrt{D}\triangle u + 2\nabla u \cdot \nabla \sqrt{D}.
\end{aligned}
$$

Using the result in (4.8) we can write,

$$
\begin{aligned}
-\triangle w + w \left(\frac{\triangle \sqrt{D}}{\sqrt{D}} \right) + (\mu_a + ik)\frac{w}{\sqrt{D}} &= 0 \\
-\triangle w + \left(\frac{\triangle \sqrt{D}}{\sqrt{D}} + \frac{\mu_a + ik}{D} \right) w &= 0 \\
-\triangle w + bw &= 0
\end{aligned}
$$

where $b = \left(\frac{\triangle\sqrt{D}}{\sqrt{D}} + \frac{\mu_a + ik}{D}\right)$. This is a Schrödinger type equation. Similarly, we want to find the Dirichlet and Neumann boundary conditions w.r.t. w. Consider,

$$w = \hat{g}, \text{ on } \partial\Omega$$
$$\frac{\partial w}{\partial n} = \hat{f}, \text{ on } \partial\Omega$$

Then using the transformation above and the boundary conditions described in (4.6) and (4.7), we have

$$u = \frac{w}{\sqrt{D}} = \frac{\hat{g}}{\sqrt{D}} = g, \text{ on } \partial\Omega$$
$$D\frac{\partial u}{\partial n} = D\frac{\partial}{\partial n}\left(\frac{w}{\sqrt{D}}\right) = Dw\frac{\partial D^{-1/2}}{\partial n} + \sqrt{D}\frac{\partial w}{\partial n} = D\hat{g}\frac{\partial D^{-1/2}}{\partial n} + \sqrt{D}\hat{f} = f, \text{ on } \partial\Omega$$

In matrix form we have,

$$\begin{bmatrix} \frac{1}{\sqrt{D}} & 0 \\ D\frac{\partial D^{-1/2}}{\partial n} & \sqrt{D} \end{bmatrix} \begin{bmatrix} \hat{g} \\ \hat{f} \end{bmatrix} = \begin{bmatrix} g \\ f \end{bmatrix}.$$

The system above has a unique solution, as the determinant of the coefficient matrix is $-1 \neq 0$. Hence one can easily get the full knowledge of Dirichlet-to-Neumann map from the knowledge of Robin-to-Neumann map. This is summarized in the following theorem, [22].

Theorem 6. *Assuming D is known on $\partial\Omega$, then the frequency domain inverse problem with a Robin-to-Neumann setting is equivalent to determining $q = (D, \mu_a) \in H^2(\Omega) \times L^\infty(\Omega)$ from all possible Dirichlet-to-Neumann pairs $(\hat{g}, \hat{f}) \in H^{1/2}(\partial\Omega) \times$*

$H^{-1/2}(\partial\Omega)$ *which are related by the Schrödinger type boundary value problem:*

$$-\triangle w + \left(\frac{\triangle\sqrt{D}}{\sqrt{D}} + \frac{\mu_a + ik}{D} \right) w = 0$$

$$w = \hat{g} \ on \ \partial\Omega$$

$$\frac{\partial w}{\partial n} = \hat{f} \ on \ \partial\Omega$$

4.2.2 Cost functional for DOT

It is understood that a uniqueness of the solution to the inverse problem follows with a complete knowledge of the Robin-to-Neumann map and appropriate restrictions to the parameter space. However, in practice we only have access to finitely many source configurations and experiments, instead of the complete knowledge of the Robin-to-Neumann map. Hence the inverse problem is solved by minimizing a cost functional for a finite number of source and measurement pairs (g_i, f_i). The most natural cost functional is simply output least squares,

$$min_{\tilde{q}\in\tilde{Q}} J(\tilde{q}) = \frac{1}{2}||\gamma_n \tilde{F}_R(0, f) - g||^2_{L^2(\partial\Omega)} + \beta||\tilde{q} - \tilde{q}_b||^2 \tag{4.9}$$

where $\tilde{F}_R(0, f)$ is forward Robin operator, f is a fixed source and g represents the Neumann data (usually a noisy measurement g^δ). The second term in the sum is the smoothing term, which helps smooth and final image, with regularization parameter given by β.

Theorem 7. *There exists a minimizer to (4.9).*

Proof. The proof is well-established in [22]. □

We give the outline of the proof. The proof uses the Fréchet differentiability of the forward operator $\gamma_n \tilde{F}_R(0, f)$, closedness of the parameter space $\tilde{Q}$ for q, which eventually shows the existence of a convergent subsequence $q_n \in \tilde{Q}$ converging to $q \in \tilde{Q}$ satisfying the restrictions (3.7).

Chapter 5

Analytical Method for EIT and DOT

The inverse problems in EIT and DOT, are extremely challenging mathematical problem, as they are nonlinear and extremely ill-posed in the Hadamard sense. Because of the promising applications and challenging mathematics, EIT and DOT attracts a vast majority of researchers across the world, all started from the pioneering work of Caldèron, [15]. The algorithms that are used to such reconstructions can be categorized as

1. iterative solvers tackling the full nonlinear problem, [1, 78].
2. direct methods, [60, 13, 18, 54, 35],

The iterative solvers exploits the Fréchet differentiability of the forward operator to use Newton-type methods. These techniques are promising, however, they are computationally expensive and slow to convergence, mostly due to the choice of proper

parameters and initial guess to the conductivity. To reduce the computational cost, researchers are encouraged to develop direct methods. Such reconstruction methods are suitable for smooth conductivity distributions.

In this chapter, we represent the mollifier approach, [60], for EIT, where the conductivity distribution is assumed to satisfy necessary smoothness condition. It uses a simple transformation and combines the concept of mollifiers, [59, 57, 58] to establish a connection between the equations defining the inverse conductivity problem and those used in inverse scattering, [20]. However, the method described in [60] had some theoretical error, and we made the appropriate modification to the method which are described in this chapter. Using the appropriate modification, we have also proposed an extension to the method for solving the inverse problems in DOT.

5.1 Mollifier approach for EIT

Consider the EIT problem, described as

$$-\nabla.(\sigma\nabla u) = 0 \text{ in } \Omega \tag{5.1}$$

$$\sigma\frac{\partial u}{\partial n} = f \text{ on } \partial\Omega \tag{5.2}$$

$$u = g \text{ on } \partial\Omega \tag{5.3}$$

where $\Omega \subset \mathbb{R}^n, n = 2$ or 3 is a bounded simply connected domain with boundary $\partial\Omega \in C^2$ and let σ be the conductivity distribution in Ω, where $0 < \sigma_1 \leq \sigma < \infty$ and

$\sigma \in C^2(\Omega) \cap C^1(\overline{\Omega})$. Using the change of variables $\tau = \sqrt{\sigma}$ we have

$$\triangle\psi(x) = -V(x)\psi(x), x \in \Omega \tag{5.4}$$

where

$$V(x) = -\frac{\triangle\tau(x)}{\tau(x)} \tag{5.5}$$

$$\psi(x) = \tau(x)u(x) \tag{5.6}$$

In terms of the new variable, the reconstruction problem becomes that of finding V (and consequently σ) from the knowledge of ψ and $\frac{\partial\psi}{\partial n}$ on the boundary $\partial\Omega$.

Definition 4. *Suppose $\lambda : \Omega \to \mathbb{R}$ is bounded and $\mathcal{H} : \Omega \times \Omega \to \mathbb{R}$ be a bounded solution of the Schrödinger equation with respect to the second variable, i.e.*

$$\triangle_y\mathcal{H}(x,y) + \lambda(y)\mathcal{H}(x,y) = 0, \quad x, y \in \Omega \tag{5.7}$$

Let $\mathcal{F}$ be the set of functions $f : \Omega \to \mathbb{R}$ which satisfy the Schrödinger equation

$$\triangle_y f(y) + \lambda(y)f(y) = 0, \quad y \in \Omega \tag{5.8}$$

here $\mathcal{H}(x,.) \in L^\infty(\Omega)$ and $\mathcal{H}(.,y) \in H^2(\Omega)$.

Applying Green's second identity, [30], to the functions ψ and $\mathcal{H}$ defined above we

have,

$$\begin{aligned}\zeta(x) &= \int_\Omega (\psi \triangle \mathcal{H} - \mathcal{H} \triangle \psi)\, dy \\ &= \int_\Omega X(y)\mathcal{H}(x,y)dy \qquad (5.9) \\ &= \int_{\partial\Omega} \left(\psi(y)\frac{\partial \mathcal{H}}{\partial n}(x,y) - \mathcal{H}(x,y)\frac{\partial \psi(y)}{\partial n}\right) dy, \quad x \in \Omega \qquad (5.10)\end{aligned}$$

where $X(y) = (V(y) - \lambda(y))\psi(y)$. Again if $\mathcal{G}_0(x,y)$ is the free space Green's function of Shrödinger equation (5.7), then we also have the following integral equation of (5.4) as

$$\psi(x) = \zeta_0(x) + \int_\Omega X(y)\mathcal{G}_0(x,y)dy, \quad x \in \Omega \qquad (5.11)$$

where

$$\zeta_0(x) = \int_{\partial\Omega} (\mathcal{G}_0(x,y)\frac{\partial \psi(y)}{\partial n} - \psi(y)\frac{\partial \mathcal{G}_0}{\partial n}(x,y))dy, \quad x \in \Omega \qquad (5.12)$$

Since (5.9) is a Fredholm equation of first kind, it is severely ill-posed, hence needs to be regularized. The reconstruction of σ in Ω using the formulation above is done using the following four steps:

1. Solve the linear problem $AX = \zeta$ given by (5.9), where

$$\begin{aligned}A : L^2(\Omega) &\to L^2(\Omega) \\ X &\mapsto \int_\Omega X(y)\mathcal{H}(x,y)dy \qquad (5.13)\end{aligned}$$

The reconstructed $X(x)$ will be an approximation to $(V(x) - \lambda(x))\psi(x), x \in \Omega$.

2. Compute $\psi(x)$ for $x \in \Omega$ using equation (5.11).

3. Compute $V(x), x \in \Omega$ using $V(x) = \frac{X(x)}{\psi(x)} + \lambda(x)$.

4. From (5.5), compute $\tau(x) = \sqrt{\sigma(x)}$ for the given boundary information of $\tau(x)$ and $\frac{\partial \tau}{\partial n}$.

This procedure will transform the nonlinear ill-posed inverse problem into a linear ill-posed problem (step-1). The reconstruction of X is done using the mollifier method [59, 58], which is a pointwise reconstruction technique and is a generalization of the Backus-Gilbert method [7, 6]. The mollifier method is based on a Dirac sequence $\{e_\gamma(\tilde{y}, y)\}$, such that

$$\int_\Omega e_\gamma(\tilde{y}, y) X(y) dy \to X(\tilde{y}), \text{ as } \gamma \to 0 \tag{5.14}$$

where the parameter γ is called the resolution or the regularization parameter at the point $\tilde{y}$. Using the mollifier method X is reconstructed as

$$X_\gamma(\tilde{y}) = \int_\Omega X(y) e_\gamma(\tilde{y}, y) dy = \langle e_\gamma(\tilde{y}, .), X \rangle_{L^2(\Omega)} \tag{5.15}$$

The adjoint operator A^* of A defined in (5.13) is defined as

$$\begin{aligned} A^* : L^2(\Omega) &\to L^2(\Omega) \\ u &\mapsto \int_\Omega \mathcal{H}(x, y) u(x) dx. \end{aligned}$$

Clearly, A is a self adjoint operator. As a regularization technique, the mollifier

method is used to find a function $u_\gamma(\tilde{y},.)$ at each reconstruction point $\tilde{y}$, satisfying,

$$A^* u_\gamma(\tilde{y},.) = e_\gamma(\tilde{y},.) \tag{5.16}$$

or to compute a minimum norm approximation to $u_\gamma(\tilde{y},.)$ by solving

$$\min \|A^* u_\gamma(\tilde{y},.) - e_\gamma(\tilde{y},.)\|_{L^2(\Omega)} \text{ using } AA^* u_\gamma(\tilde{y},.) = Ae_\gamma(\tilde{y},.) \tag{5.17}$$

Then $X_\gamma(\tilde{y})$ can be estimated as

$$\begin{aligned} X_\gamma(\tilde{y}) &= \langle e_\gamma(\tilde{y},.), X\rangle_{L^2(\Omega)} \\ &\approx \langle A^* u_\gamma(\tilde{y},.), X\rangle_{L^2(\Omega)} \\ &= \langle u_\gamma(\tilde{y},.), AX\rangle_{L^2(\Omega)} = \langle u_\gamma(\tilde{y},.), \zeta\rangle_{L^2(\Omega)}. \end{aligned} \tag{5.18}$$

The construction of $u_\gamma(\tilde{y},.)$ is obtained by solving the ill-posed operator (5.16). Let $\tilde{e}_\gamma = A^* u_\gamma$, where u_γ is the minimizer of (5.18). Thus instead of reconstructing X_γ using (5.16), it can be reconstructed using the following

$$X_\gamma(x) = \int_\Omega X(y)\tilde{e}_\gamma(x,y)dy \tag{5.19}$$

$\tilde{e}_\gamma$ can be obtained from the range of A^*, which depends on the choice of the integral kernel $\mathcal{H}$.

Lemma 14. *Range*$(A^*) \subset \mathcal{F}$.

Proof. Suppose $f \in L^2(\Omega)$. Then we have

$$\begin{aligned}\triangle_y A^* f(y) &= \int_\Omega \triangle_y \mathcal{H}(x,y) f(x) dx \\ &= -\int_\Omega \lambda(y) \mathcal{H}(x,y) f(x) dx, \text{ using (5.7)} \\ &= -\lambda(y) A^* f(y).\end{aligned}$$

□

So if $\{h_l(y) | l \in \mathbb{Z}\}$ is an orthonormal basis for $\mathcal{F}$, the effective mollifier $\tilde{e}_\gamma$ at the point $\tilde{y}$ can be expressed as,

$$\tilde{e}_\gamma(\tilde{y}, y) = \sum_{l \in \mathcal{Z}} \langle e_\gamma(\tilde{y}, .), h_l \rangle_{L^2(\Omega)} h_l(y) \tag{5.20}$$

We can also choose $\mathcal{H}(x,y)$ as

$$\mathcal{H}(x,y) = \sum_{l \in \mathcal{Z}} c_l(x) \langle e_\gamma(\tilde{y}, .), h_l \rangle_{L^2(\Omega)} h_l(y) \tag{5.21}$$

with bounded coefficients $\{c_l(x)\}$ satisfying

$$|c_l(x)| \leq M_l, \quad x \in \Omega, \text{ where } \sum_{l \in \mathcal{Z}} M_l < \infty. \tag{5.22}$$

With the choices of $\tilde{e}_\gamma$ and $\mathcal{H}$ we can reconstruct X_γ (i.e. X) proven in the following theorem, [60].

Theorem 8. *For a fixed $\tilde{y} \in \Omega$, let $e_\gamma(\tilde{y}, y) \in L^2(\Omega)$ be the mollifier function, and $\tilde{e}_\gamma(\tilde{y}, y)$ its projection on $\mathcal{F}$ given by (5.20), then the approximation to the solution*

X at $\tilde{y}$ is given by,

$$X_\gamma(\tilde{y}) = \langle \tilde{e}_\gamma(\tilde{y}, .), X \rangle_{L^2(\Omega)} = \int_{\partial\Omega} \left(\psi(y) \frac{\partial \tilde{e}_\gamma(\tilde{y}, y)}{\partial n} - \tilde{e}_\gamma(\tilde{y}, x) \frac{\partial \psi(y)}{\partial n} \right) dy$$

Proof.

$$\begin{aligned}
X_\gamma(\tilde{y}) &= \langle \tilde{e}_\gamma(\tilde{y}, .), X \rangle_{L^2(\Omega)} \\
&= \langle u_\gamma(\tilde{y}, .), \zeta \rangle_{L^2(\Omega)} \\
&= \int_\Omega u_\gamma(\tilde{y}, x) \zeta(x) dx \\
&= \int_\Omega u_\gamma(\tilde{y}, x) \left(\int_{\partial\Omega} \left(\psi(y) \frac{\partial \mathcal{H}}{\partial n}(x, y) - \mathcal{H}(x, y) \frac{\partial \psi(y)}{\partial n} \right) dy \right) dx \\
&= \int_\Omega u_\gamma(\tilde{y}, x) \left(\sum_{l \in \mathcal{Z}} \langle e_\gamma(\tilde{y}, .), h_l \rangle_{L^2(\Omega)} c_l(x) \int_{\partial\Omega} \left(\psi(y) \frac{\partial h_l(y)}{\partial n} - h_l(y) \frac{\partial \psi(y)}{\partial n} \right) dy \right) dx \\
&= \sum_{l \in \mathcal{Z}} \langle e_\gamma(\tilde{y}, .), h_l \rangle_{L^2(\Omega)} \int_{\partial\Omega} \left(\psi(y) \frac{\partial h_l(y)}{\partial n} - h_l(y) \frac{\partial \psi(y)}{\partial n} \right) dy \\
&= \int_{\partial\Omega} \left(\psi(y) \frac{\partial \tilde{e}_\gamma(\tilde{y}, y)}{\partial n} - \tilde{e}_\gamma(\tilde{y}, x) \frac{\partial \psi(y)}{\partial n} \right) dy \qquad (5.23)
\end{aligned}$$

□

The above theorem shows that that the calculation of the regularized solution X_γ at a point $\tilde{y} \in \Omega$ can be done by an integration over the boundary $\partial\Omega$.

5.1.1 Analytic formulation of X_γ

The fundamental solution of (5.7) is known as, [51], for any $\lambda > 0$,

$$\mathcal{G}_0(x,y) = \begin{cases} -\frac{1}{4}Y_0(\sqrt{\lambda}||x-y||) & n=2 \\ \frac{1}{4\pi}\frac{\cos(\sqrt{\lambda}||x-y||)}{||x-y||} & n=3 \end{cases} \tag{5.24}$$

where Y_0 is the Bessel's function of the second kind.

Throughout the dissertation, we considered Ω to be a disc of radius R, i.e., $\Omega = \{(r\cos\theta, r\sin\theta) : 0 < r < R, 0 \leq \theta \leq 2\pi\}$. The orthonormal solutions $\{h_l^j : l \in \mathbb{Z}, j = 1,2\}$ of (5.7) are given by,

$$h_l^1(r,\theta) = \rho_l J_l(\sqrt{\lambda_l}r)\cos(l\theta)$$
$$h_l^2(r,\theta) = \rho_l J_l(\sqrt{\lambda_l}r)\sin(l\theta)$$

where ρ_l are the normalization constants, and $\lambda_l = (\frac{\alpha_l}{R})^2$ with α_l is the first zero of the bessel function J_l.

Lemma 15. *The normalization constants ρ_l are given as,*

$$\rho_l = \frac{1}{R}\sqrt{\frac{2}{\pi J_{l+1}(\sqrt{\lambda_l})^2}} \tag{5.25}$$

Proof. In order to make the solutions orthonormal, we need

$$\begin{aligned}
&\int_\Omega h_l^j(y)^2 dy = 1 \\
\implies \rho_l^2 \int_{r=0}^{R}\int_{\theta=0}^{2\pi} J_l(\sqrt{\lambda_l}r)\cos^2(l\theta) r dr d\theta = 1,\ &\text{for } j=1 \\
\implies \rho_l^2 \pi \int_{r=0}^{R} J_l(\sqrt{\lambda_l}r) r dr = 1& \\
\implies \rho_l^2 \frac{R^2}{2}\pi J_{l+1}^2(\sqrt{\lambda_l}) = 1& \\
\implies \rho_l = \frac{1}{R}\sqrt{\frac{2}{\pi J_{l+1}(\sqrt{\lambda_l}R)^2}}.&
\end{aligned}$$

□

Lemma 16. *If (s,ω) are the polar coordinates of $\tilde{y}$, the center of the mollifier disc, (r,θ) are the polar coordinates of any point in Ω, then*

$$\tilde{e}_\gamma(s,\omega;r,\theta) = \frac{2}{\sqrt{\lambda}\gamma} J_1(\sqrt{\lambda}\gamma) \sum_{l\in\mathbb{Z}} \rho_l^2 J_l(\sqrt{\lambda_l}s) J_l(\sqrt{\lambda_l}r)\cos(l(\omega-\theta))$$

Furthermore, if the boundary data are sufficiently smooth to guarantee that $\psi \in C(\partial\Omega)$, and both ψ and $\frac{\partial\psi}{\partial n}$ are piecewise smooth on $\partial\Omega$, then

$$\begin{aligned}
X_\gamma(r,\theta) = \frac{2\pi R J_1(\sqrt{\lambda}\gamma)}{\sqrt{\lambda}\gamma} \sum_{l\in\mathbb{Z}} \rho_l^2 J_l(\sqrt{\lambda_l}r) \Big(J_l'(\sqrt{\lambda_l}R)\sqrt{\lambda_l}(a_l\cos(l\theta) + b_l\sin(l\theta)) \\
- J_l(\sqrt{\lambda_l}R)(c_l\cos(l\theta) + d_l\sin(l\theta))\Big)
\end{aligned}$$

where a_l, b_l, c_l, d_l are the Fourier series coefficients of $\psi(R,\theta)$ and $\frac{\partial\psi}{\partial n}(R,\theta)$, respectively.

Proof. From the inner product in (5.20), we have

$$\begin{aligned}\langle e_\gamma(\tilde{y},\cdot), h_l\rangle_{L^2(\Omega)} &= \int_\Omega e_\gamma(\tilde{y},y), h_l(y)dy \\ &= \frac{1}{\pi\gamma^2}\int_{B(\tilde{y},\gamma)} h_l(y)dy\end{aligned}$$

Using mean value theorem for Helmholtz equation, [24], we have,

$$\int_{B(\tilde{y},\gamma)} h_l(y)dy = \left(\frac{2\pi\gamma}{\sqrt{\lambda}}\right)^{n/2} J_{n/2}(\sqrt{\lambda}\gamma)h_l(\tilde{y})$$

Hence from (5.20) and for $n = 2$, we have,

$$\begin{aligned}\tilde{e}_\gamma(\tilde{y};y) &= \frac{2}{\sqrt{\lambda}\gamma}J_1(\sqrt{\lambda}\gamma)\sum_{l\in\mathbb{Z}} h_l(\tilde{y})h_l(y) \\ &= \frac{2}{\sqrt{\lambda}\gamma}J_1(\sqrt{\lambda}\gamma)\sum_{l\in\mathbb{Z}} \rho_l^2 J_l(\sqrt{\lambda_l}s)J_l(\sqrt{\lambda_l}r)\cos\left(l(\omega-\theta)\right).\end{aligned}$$

The analytical result for $X_\gamma(r,\theta)$ can be easily derived by substituting the above result for $\tilde{e}_\gamma$ and the Fourier expansions of $\psi(R,\theta)$, $\frac{\partial\psi}{\partial n}(r,\theta)$ in the result of Theorem 8. □

Knowing X_γ, the estimate of X, computation of ψ inside the unit disc is done using the integral formulae in (5.11), (5.12), expressed as,

$$\psi(r,\theta) = \zeta_0(r,\theta) + \int_0^1\int_0^{2\pi} \rho\mathcal{G}_0(r,\theta;\rho,v)X_\gamma(\rho,v)d\rho dv \tag{5.26}$$

where

$$\zeta_0(r,\theta) = \int_0^{2\pi}\left(\mathcal{G}_0(r,\theta;1,v)\frac{\partial\psi}{\partial n}(1,v) - \frac{\partial\mathcal{G}_0}{\partial n}(r,\theta;1,v)\psi(1,v)\right)dv \tag{5.27}$$

Now, $\mathcal{G}_0$ has a weak singularity when $(r,\theta) = (\rho, v)$. To avoid this singularity in computing, a subtraction technique, [69], is used, which uses the following well-known result,

$$\int_0^1 \int_0^{2\pi} \rho \mathcal{G}_0(r,\theta;\rho,v)d\rho = -\left(\frac{1}{\lambda} + \frac{\pi}{2\sqrt{\lambda}} J_0(\sqrt{\lambda}r)Y_1(\sqrt{\lambda})\right).$$

(5.26) is re written and further simplified as,

$$\begin{aligned}
\psi(r,\theta) &= \zeta_0(r,\theta) + \int_0^1 \int_0^{2\pi} \rho \mathcal{G}_0(r,\theta;\rho,v)[X_\gamma(\rho,v) - X_\gamma(r,\theta)]d\rho dv \\
&\quad + X_\gamma(r,\theta) \int_0^1 \int_0^{2\pi} \rho \mathcal{G}_0(r,\theta;\rho,v)d\rho \\
&= \zeta_0(r,\theta) - X_\gamma(r,\theta)\left(\frac{1}{\lambda} + \frac{\pi}{2\sqrt{\lambda}} J_0(\sqrt{\lambda}r)Y_1(\sqrt{\lambda})\right) \\
&\quad + \int_0^1 \int_0^{2\pi} \rho \mathcal{G}_0(r,\theta;\rho,v)[X_\gamma(\rho,v) - X_\gamma(r,\theta)]d\rho dv
\end{aligned}$$

The integral term in the above formula can be computed using quadrature foumula for numerical integration. We used a set of 172 quadrature points and weights for the unit disc listed in [29]. Using these quadrature points (ρ_i, v_i) and weights w_i, the above integral formula can be rewritten as,

$$\begin{aligned}
\psi(r,\theta) &= \zeta_0(r,\theta) - X_\gamma(r,\theta)\left(\frac{1}{\lambda} + \frac{\pi}{2\sqrt{\lambda}} J_0(\sqrt{\lambda}r)Y_1(\sqrt{\lambda})\right) \\
&\quad + \sum_{k=1}^{172} w_k \mathcal{G}_0(r,\theta;\rho_k,v_k)[X_\gamma(\rho_k,v_k) - X_\gamma(r,\theta)]
\end{aligned}$$

Once ψ is computed, then $V(r,\theta)$ is computed using the formula $V(x) = \frac{X(x)}{\psi(x)} + (x)$, described in step 3. Using V in (5.5), we compute τ as,

$$\tau(r,\theta) = \tau_0(r,\theta) + \int_0^1 \int_0^{2\pi} \rho \mathcal{G}_0(r,\theta;\rho,v)V(\rho,v)\tau(\rho,v)d\rho dv. \tag{5.28}$$

As before, the weak singularity of $\mathcal{G}_0 V$ is avoided by using the subtraction technique, [69], and Engel's quadrature points and weights, we rewrite $\tau(r,\theta)$ as,

$$\tau(r,\theta) = \tau_0(r,\theta) - V(r,\theta)\tau(r,\theta)\left(\frac{1}{\lambda} + \frac{\pi}{2\sqrt{\lambda}} J_0(\sqrt{\lambda}r)Y_1(\sqrt{\lambda})\right) \tag{5.29}$$

$$+ \sum_{k=1}^{172} w_k \mathcal{G}_0(r,\theta;\rho_k,v_k)[V(\rho_k,v_k)\tau(\rho_k,v_k) - V(r,\theta)\tau(r,\theta)] \tag{5.30}$$

where $\tau_0(r,\theta)$ can be computed numerically using the boundary data of $\tau(1,v)$ and $\frac{\partial\tau}{\partial n}(1,v)$,

$$\tau_0(r,\theta) = \int_0^{2\pi} \left(\mathcal{G}_0(r,\theta;1,v)\frac{\partial\tau}{\partial n}(1,v) - \frac{\partial\mathcal{G}_0}{\partial n}(r,\theta;1,v)\tau(1,v)\right) dv. \tag{5.31}$$

5.2 Mollifier approach for DOT

In light of the discussion in the previous section, we extend the mollifier approach for solving the inverse DOT problem. Consider the DOT problem:

$$-\nabla.(D\nabla u) + (\mu + ik)u = 0 \text{ in } \Omega \tag{5.32}$$

$$D\frac{\partial u}{\partial n} = f \text{ on } \partial\Omega \tag{5.33}$$

$$u = g \text{ on } \partial\Omega \tag{5.34}$$

where $\Omega \subset \mathbb{R}^n, n = 2$ or 3 is a bounded simply connected domain with boundary $\partial\Omega \in C^2$ and let D be the conductivity distribution in Ω, where $0 < D_0 \leq D < D_1 <$

∞ and $D \in C^2(\Omega) \cap C^1(\overline{\Omega})$. Using the change of variables $\tau = \sqrt{D}$ we have

$$\triangle\psi(x) = -V(x)\psi(x), x \in \Omega \tag{5.35}$$

where

$$V(x) = -\frac{\triangle\tau(x)}{\tau(x)} + \frac{\mu(x) + ik}{\tau^2(x)} = V_R + iV_I \tag{5.36}$$

$$\psi(x) = \tau(x)u(x) \tag{5.37}$$

where, $V_R = Re(V) = -\frac{\triangle\tau(x)}{\tau(x)} + \frac{\mu(x)}{\tau^2(x)}$ and $V_I = Im(V) = \frac{k}{\tau^2(x)}$. In terms of the new variable, the reconstruction problem becomes that of finding V (and consequently D and μ) from the knowledge of ψ and $\frac{\partial\psi}{\partial n}$ on the boundary $\partial\Omega$.

Definition 5. *Suppose $\lambda : \Omega \to \mathbb{C}$ is bounded and $\mathcal{H} : \Omega \times \Omega \to \mathbb{C}$ be a bounded solution of the Schrödinger equation with respect to the second variable, i.e.*

$$\triangle_y\mathcal{H}(x, y) + \lambda(y)\mathcal{H}(x, y) = 0, \quad x, y \in \Omega \tag{5.38}$$

Let $\tilde{\mathcal{F}}$ be the set of functions $\tilde{f} : \Omega \to \mathbb{R}$ which satisfy the Schrödinger equation

$$\triangle_y\tilde{f} + \lambda(y)\tilde{f} = 0, \quad y \in \Omega \tag{5.39}$$

here $\mathcal{H}(x, .) \in L^\infty(\Omega)$ and $\mathcal{H}(., y) \in H^2(\Omega)$.

Applying Green's second identity [31] to the functions ψ and $\bar{\mathcal{H}}$, complex conjugate

of $\mathcal{H}$, defined above we have,

$$\begin{aligned}\tilde{\zeta}(x) &= \int_\Omega (\mathcal{H}\triangle\psi - \psi\triangle\mathcal{H})dy \\ &= \int_\Omega \bar{X}(y)\mathcal{H}(x,y)dy \qquad (5.40) \\ &= \int_{\partial\Omega} \left(\psi(y)\frac{\partial\mathcal{H}}{\partial n}(x,y) - \mathcal{H}(x,y)\frac{\partial\psi(y)}{\partial n}\right) dy, \quad x \in \Omega \qquad (5.41)\end{aligned}$$

where $\bar{X}(y) = (V(y) - \lambda(y))\psi(y)$. Again if $\mathcal{G}(x,y)$ is the free space Green's function of Shrödinger equation (5.38), then we also have the following integral equation of (5.42) as

$$\psi(x) = \tilde{\zeta}_0(x) + \int_\Omega X(y)\mathcal{G}(x,y)dy, \quad x \in \Omega \qquad (5.42)$$

where

$$\tilde{\zeta}_0(x) = \int_{\partial\Omega} \left(\mathcal{G}(x,y)\frac{\partial\psi(y)}{\partial n} - \psi(y)\frac{\partial\mathcal{G}}{\partial n}(x,y)\right) dy, \quad x \in \Omega \qquad (5.43)$$

The reconstruction of D and μ in Ω using the formulation above is can be done using the following four steps:

1. Solve the linear problem $\tilde{A}X = \tilde{\zeta}$ given by (5.40), where

$$\begin{aligned}\tilde{A} : L^2(\Omega) &\to L^2(\Omega) \\ X &\mapsto \int_\Omega \bar{X}(y)\mathcal{H}(x,y)dy \qquad (5.44)\end{aligned}$$

   The reconstructed $\bar{X}(x)$ will be an approximation to $(V(x) - \lambda(x))\psi(x), x \in \Omega$.

2. Compute $\psi(x)$ for $x \in \Omega$ using equation (5.42).

3. Compute $V(x), x \in \Omega$ using $V(x) = \frac{X(x)}{\psi(x)} + \lambda(x) = V_R + iV_I$.

4. Compute $\tau^2(x) = D(x)$ using $V_I = \frac{k}{\tau^2(x)}$ and $\mu(x)$ using $V_R = -\frac{\triangle\tau(x)}{\tau(x)} + \frac{\mu(x)}{\tau^2(x)}$.

As described before, the reconstruction of $X(x)$ can be done using the mollifier method as,

$$\int_\Omega \bar{X}(y) e_\gamma(\tilde{y}, y) X(y) dy \to \bar{X}(\tilde{y}), \text{ as } \gamma \to 0 \tag{5.45}$$

where $\bar{X}$ is the complex conjugate of X, and e_γ is a standard choice of mollifier given by

$$e_\gamma(\tilde{y}, y) = \frac{1}{|B(\tilde{y}, y)|} \cdot \chi_{B(y,\gamma)}(y) \tag{5.46}$$

Assuming that a reconstruction point $\tilde{y}$ and a desired resolution γ have been chosen, instead of reconstructing X itself, we attempt a reconstruction of

$$\bar{X}_\gamma(\tilde{y}) = \int_\Omega \bar{X}(y) e_\gamma(\tilde{y}, y) dy = \langle e_\gamma(\tilde{y}, .), X \rangle_{L^2(\Omega)} \tag{5.47}$$

The adjoint operator $\tilde{A}^*$ of $\tilde{A}$ defined in (5.44) is defined as

$$\begin{aligned} \tilde{A}^* : L^2(\Omega) &\to L^2(\Omega) \\ u &\mapsto \int_\Omega \mathcal{H}(x, y) \bar{u}(x) dx \end{aligned}$$

where $\bar{u}$ is the complex conjugate of u. We note that $\tilde{A}$ is not a self-adjoint operator. The idea of the mollifier method can similarly be extended in DOT as a regularization

technique to find, at each reconstruction point $\tilde{y}$, a function $u_\gamma(\tilde{y},.)$ satisfying

$$\tilde{A}^* u_\gamma(\tilde{y},.) = e_\gamma(\tilde{y},.) \tag{5.48}$$

or to compute a minimum norm approximation to $u_\gamma(\tilde{y},.)$ by solving

$$\min \|\tilde{A}^* u_\gamma(\tilde{y},.) - e_\gamma(\tilde{y},.)\|_{L^2(\Omega)} \text{ using } \tilde{A}\tilde{A}^* u_\gamma(\tilde{y},.) = \tilde{A} e_\gamma(\tilde{y},.) \tag{5.49}$$

Then $X_\gamma(\tilde{y})$ can then be estimated as

$$\begin{aligned} \bar{X}_\gamma(\tilde{y}) &= \langle e_\gamma(\tilde{y},.), X\rangle_{L^2(\Omega)} \\ &\approx \langle \tilde{A}^* u_\gamma(\tilde{y},.), X\rangle_{L^2(\Omega)} \\ &= \langle u_\gamma(\tilde{y},.), \tilde{A}X\rangle_{L^2(\Omega)} = \langle u_\gamma(\tilde{y},.), \tilde{\zeta}\rangle_{L^2(\Omega)}. \end{aligned} \tag{5.50}$$

The construction of $u_\gamma(\tilde{y},.)$ requires us to solve the ill-posed operator (5.48). Let $\tilde{e}_\gamma = \tilde{A}^* u_\gamma$, where u_γ is the minimizer of (5.49). Thus instead of reconstructing X_γ using (5.48), it can be reconstructed using the following

$$\bar{X}_\gamma(x) = \int_\Omega \bar{X}(y)\tilde{e}_\gamma(x,y)dy \tag{5.51}$$

Using the following lemma $\tilde{e}_\gamma$ can be obtained from the range of $\tilde{A}^*$.

Lemma 17. *Range*$(\tilde{A}^*) \subset \tilde{\mathcal{F}}$.

Proof. The proof is same as the lemma 14. □

Based on the above lemma, our next goal is to obtain an orthonormal basis of $\tilde{\mathcal{F}}$.

The theoretical establishment of the mollifier method for DOT is based on identifying an orthonormal basis of the solution space of the Schrödinger equation (5.38), with complex potential. In [66], the authors constructed a self-adjoint dilation of the operator representing (5.38). In [62], the author provided an integral expression for the green's function of the class of Schrödinger function with complex potential as,

$$\mathcal{G}(x,y) = \mathcal{G}_0(x,y) - \int_\Omega \mathcal{G}_0(x,y)\lambda(y)\mathcal{G}(x,y)dy$$

where $\mathcal{G}_0(x,y)$ is the green's function defined in the previous section. So we can assume that, there exists an orthonormal basis $\{\tilde{h}_l(y)|l \in \mathbb{Z}\}$ for $\tilde{\mathcal{F}}$.
Expressing the effective mollifier $\tilde{e}_\gamma$ at the point $\tilde{y}$ is given by

$$\tilde{e}_\gamma(\tilde{y},y) = \sum_{l\in\mathcal{Z}} \langle e_\gamma(\tilde{y},.), \tilde{h}_l\rangle_{L^2(\Omega)} \tilde{h}_l(y) \tag{5.52}$$

We can also choose $\mathcal{H}(x,y)$ as

$$\mathcal{H}(x,y) = \sum_{l\in\mathcal{Z}} c_l(x)\langle e_\gamma(\tilde{y},.), \tilde{h}_l\rangle_{L^2(\Omega)} \tilde{h}_l(y) \tag{5.53}$$

with bounded coefficients $\{c_l(x)\}$ satisfying

$$|c_l(x)| \le M_l, \quad x \in \Omega, \text{ where } \sum_{l\in\mathcal{Z}} M_l < \infty. \tag{5.54}$$

With the choices of $\tilde{e}_\gamma$ and $\mathcal{H}$ we can reconstruct X_γ (i.e. X) using the following theorem.

Theorem 9. *For a fixed $\tilde{y} \in \Omega$, let $e_\gamma(\tilde{y},y) \in L^2(\Omega)$ be the mollifier function, and $\tilde{e}_\gamma(\tilde{y},y)$ its projection on $\tilde{\mathcal{F}}$ given by (5.52), then the approximation to the solution*

X at $\tilde{y}$ is given by,

$$X_\gamma(\tilde{y}) = \langle \tilde{e}_\gamma(\tilde{y}, .), X \rangle_{L^2(\Omega)} = \int_{\partial\Omega} \left(\psi(y) \frac{\partial \tilde{e}_\gamma(\tilde{y}, y)}{\partial n} - \tilde{e}_\gamma(\tilde{y}, x) \frac{\partial \psi(y)}{\partial n} \right) dy$$

Proof.

$$\begin{aligned}
\bar{X}_\gamma(\tilde{y}) &= \langle \tilde{e}_\gamma(\tilde{y}, .), X \rangle_{L^2(\Omega)} \\
&= \langle u_\gamma(\tilde{y}, .), \tilde{\zeta} \rangle_{L^2(\Omega)} \\
&= \int_\Omega u_\gamma(\tilde{y}, x) \bar{\zeta}(x) dx \\
&= \int_\Omega u_\gamma(\tilde{y}, x) \left(\int_{\partial\Omega} \overline{\left(\psi(y) \frac{\partial \mathcal{H}}{\partial n}(x, y) - \mathcal{H}(x, y) \frac{\partial \psi(y)}{\partial n} \right)} dy \right) dx \\
&= \int_\Omega u_\gamma(\tilde{y}, x) \left(\sum_{l \in \mathcal{Z}} \langle e_\gamma(\tilde{y}, .), h_l \rangle_{L^2(\Omega)} c_l(x) \int_{\partial\Omega} \overline{\left(\psi(y) \frac{\partial h_l(y)}{\partial n} - h_l(y) \frac{\partial \psi(y)}{\partial n} \right)} dy \right) dx \\
&= \sum_{l \in \mathcal{Z}} \langle e_\gamma(\tilde{y}, .), h_l \rangle_{L^2(\Omega)} \int_{\partial\Omega} \overline{\left(\psi(y) \frac{\partial h_l(y)}{\partial n} - h_l(y) \frac{\partial \psi(y)}{\partial n} \right)} dy \\
&= \int_{\partial\Omega} \overline{\left(\psi(y) \frac{\partial \tilde{e}_\gamma(\tilde{y}, y)}{\partial n} - \tilde{e}_\gamma(\tilde{y}, x) \frac{\partial \psi(y)}{\partial n} \right)} dy. \qquad (5.55)
\end{aligned}$$

□

Since the numerical computation of the orthonormal basis is hard, so in this extension we are using $\{h_l | l \in \mathbb{Z}\}$ as described in the subsecion 5.1.1, as an approximation to $\tilde{h}_l$.

Chapter 6

Iterative Method for EIT and DOT

In this chapter, we briefly discuss the iterative approaches we used in this dissertation for the inverse problems. We discuss the implementation of the classic iteratively regularized Gauss-Newton (IRGN) method for solving the inverse problems in EIT and DOT. The corresponding forward problems are solved using the finite element (FEM) Galerkin method. For iterative algorithm, we reformulate the inverse problems for CEM and DOT and discuss the implementation of IRGN for the reconstruction of the parameters.

6.1 IRGN method for EIT

We recover σ by minimizing the following cost functional iteratively from a finite set of measurements, as EIT is severly ill-posed.

$$J(\sigma) = ||F(\sigma) - g^{\delta}||_2^2$$

where g^{δ} approximates the exact data g with the accuracy δ, i.e.,

$$||g - g^{\delta}|| < \delta. \tag{6.1}$$

However, regularization is needed to improve the ill-posed problem and instead, we minimize,

$$J_{\lambda}(\sigma) = ||F(\sigma) - g^{\delta}||_2^2 + \lambda R(\sigma - \sigma^*)$$

where λ is the regularization parameter, $R(\cdot)$ is the regularization term and σ^* is the known background. There are several choices for $R(\cdot)$. The ℓ_p regularization $R_{\ell_p}(\sigma - \sigma^*)$ is defined as

$$R_{\ell_p}(\sigma - \sigma^*) = ||\sigma - \sigma^*||_p.$$

where $0 < p \leq 2$ is a constant, [49]. The ℓ_p regularization enforces sparsity for $0 < p \leq 1$ and smoothness when $p \geq 2$. Total variation regularization is used for most practical applications to obtain smooth images. Total variation is defined as

[77, 43, 1],

$$R_{TV}(\sigma) = \sup\{\int_{\Omega} \sigma \text{ div } z dx | z \in C_0^{\infty}(\Omega), ||z||_{\infty} \leq 1\} = |D\sigma|(\Omega),$$

where $|\cdot|(\Omega)$ is a finite Radon measure. In particular, for $\sigma \in W^{1,1}(\Omega)$, it reduces to the standard notation for TV regularization,

$$R_{TV}(\sigma) = \int_{\Omega} |\nabla \sigma| dx.$$

The regularization function is represented by a norm for most analytical methods. In this dissertation, we used one of the most successful methods for solving the ill-conditioned problem, R_{ℓ_2} known as Tikhonov regularization. The cost functional from Tikhonov regularization is

$$J_{\lambda}(\sigma) = \frac{1}{2}||F(\sigma) - u_{\delta}||_2^2 + \frac{\lambda}{2}||W(\sigma - \sigma^*)||_2^2, \tag{6.2}$$

where W is weight function and upon discretization becomes a weight matrix. There are several iterative approaches to minimize (6.2). In this dissertation, we used a modified iteratively regularized Gauss-Newton (IRGN) method for the minimization, which is described in this section.

Suppose λ_k is some sequence of regularizing parameters satisfying the conditions

$$\lambda_k \geq \lambda_{k+1} > 0, \quad \sup_{k \in \mathbb{N} \cup \{0\}} \frac{\lambda_k}{\lambda_{k+1}} = \hat{d} < \infty, \quad \lim_{k \to \infty} \lambda_k = 0. \tag{6.3}$$

Let the unique global minimum of (6.2) be denoted by $\tilde{\sigma}$. Assume $\tilde{\sigma}$ satisfies the invertibility conditions, then the unique global minimum of (6.2) is explicitly given

by

$$\tilde{\sigma} = \sigma_k - (F'(\sigma_k)^T F'(\sigma_k) + \lambda_k W_2)^{-1}\{F'(\sigma_k)^T (F(\sigma_k) - g_\delta) + \lambda_k W_2(\sigma_k - \sigma^*)\}, \quad (6.4)$$

where σ_k is the k-th approximation to σ and $F'(\sigma_k)$ is the jacobian matrix at the k-th iteration, and $W_2 = W^T W$. The above algorithm is generalized further using a line search procedure from [74, 1]. A variable step size, s_k, is introduced, such that

$$0 < s_k \leq 1. \quad (6.5)$$

The modified IRGN algorithm is then

$$\sigma_{k+1} = \sigma_k - s_k(F'(\sigma_k)^T F'(\sigma_k) + \lambda_k W_2)^{-1}\{F'(\sigma_k)^T (F(\sigma_k) - g_\delta) + \lambda_k W_2(\sigma_k - \sigma^*)\}. \quad (6.6)$$

The line search parameter s_k is chosen to minimize the scalar objective function

$$\Phi(s) = J(\sigma_k + s p_k) \quad (6.7)$$

where p_k is the search direction, which solves

$$(F'(\sigma_k)^T F'(\sigma_k) + \lambda_k W_2) p_k = -\left[F'(\sigma_k)^T (F(\sigma_k) - g_\delta) + \lambda_k W_2(\sigma_k - \sigma^*)\right] \quad (6.8)$$

This step is accomplished through a backtracking strategy until either one of the strong Wolfe conditions,

$$J(\sigma_k + s p_k) \leq J(\sigma_k) + c_1 s \nabla J(\sigma_k)^T p_k \quad (6.9)$$

$$|\nabla J(\sigma_k + s p_k)^T p_k| \leq |c_2 \nabla J(\sigma_k)^T p_k|. \quad (6.10)$$

is satisfied [84], or the maximum number of backtracking steps has been reached. We use the theoretically derived values of $c_1 = 0.0001$ and $c_2 = 0.9$, derived in [84]. Due to the inexact nature of u_δ, we adopt a stopping rule from [8, 1] to terminate the iterations at the first index $\mathcal{K} = \mathcal{K}(\delta)$, such that

$$||F(\sigma_{\mathcal{K}}) - g^\delta||^2 \leq \rho\delta < ||F(\sigma_k) - g^\delta||^2, \quad 0 \leq k \leq \mathcal{K}, \quad \rho > 1. \tag{6.11}$$

6.2 IRGN for DOT

In DOT, we want to solve the inverse problem and reconstruct both the diffusion coefficient D and the absorption coefficient μ_a. Therefore, we need to make some modifications to implement IRGN for solving the inverse problem in DOT. In this section, we discuss the modifications we implemented.

As in EIT, we obtain the simulated data by solving the DOT forward problem using the Galerkin FEM for known D and μ_a. The goal of the inverse problem is then to obtain the distribution for D and μ_a which minimizes the following cost functional using Tikhonov regularization,

$$J_\gamma(\lambda, q) = \frac{1}{2}||\gamma_0 F_N^{(k,q)}(0, f) - g^\delta||_2^2 + \frac{\lambda}{2}||\nabla(q - q_b)||_2^2 \tag{6.12}$$

where $q = (D, \mu_a)^T$, $q_b = (D_b, \mu_b)$ is the known background, $\gamma_0 F_N^{(k,q)}(0, f)$ is the Neumann-to-Dirichlet data, g^δ is the noisy data with a noise level of δ, satisfying $||\gamma_0 F_N^{(k,q)}(0, f) - g^\delta|| \leq \delta$, and $\lambda = (\lambda_D, \lambda_{\mu_a})^T$ are the regularization parameters. As we want to estimate D and μ_a, the discrete sensitivity relation, which is the jacobian

matrix of $J_\gamma(\lambda, q)$, is computed as

$$\nabla J = [J_{D_k}, J_{\mu_k}]$$

where J_D and J_{μ_a} are the jacobian matrices with respect to D and μ_a, respectively at the k-th iteration. Thus the search direction $p_k = (p_{D_k}, p_{\mu_k})^T$ for the IRGN algorithm is obtained by solving the following block system,

$$\left[\begin{pmatrix} J_D^T J_D & J_D^T J_{\mu_a} \\ J_{\mu_a}^T J_D & J_{\mu_a}^T J_{\mu_a} \end{pmatrix} + \lambda_k W \right] \begin{pmatrix} p_{D_k} \\ p_{\mu_k} \end{pmatrix} = - \left(J_D^T, J_{\mu_k}^T \right) \left(\gamma_0 F_N^{(k,q)}(0, f) - g^\delta \right) - \lambda_k W (q - q^*) \tag{6.13}$$

where

$$W = \begin{pmatrix} L_D^T L_D & 0 \\ 0 & L_\mu^T L_\mu^T \end{pmatrix}.$$

6.3 Convergency of IRGN method

Assume that F is a nonlinear operator acts on the Hilbert spaces (H, H_1), $F : D(F) \subset H \to H_1$, and F is Fréchet differentiable in $D(F)$. We consider minimizing the functional

$$J(q) = ||F(q) - g^\delta||_{H_1}^2 \tag{6.14}$$

where g^δ approximates the exact data g with the accuracy δ, i.e.,

$$||g - g^\delta|| \leq \delta \tag{6.15}$$

Our interest is to find an element $\hat{q} \in D(F)$, s.t.

$$||F(\hat{q}) - g||_{H_1} = \inf_{q \in D(F)} ||F(q) - g||_{H_1} = 0 \tag{6.16}$$

Consider the following conditions hold

$$||F'(q_1)|| \leq M_1, \quad \text{for any } q_1 \in B_\eta(\hat{q}) \tag{6.17}$$

$$||F'(q_1) - F'(q_2)|| \leq M_2||q_1 - q_2||, \text{ for any } q_1, q_2 \in B_\eta(\hat{q}) \tag{6.18}$$

where $B_\eta(\hat{q}) = \{q \in H : ||q - \hat{q}|| \leq \eta\} \subset D(F)$. The convergence analysis of IRGN is done under the source condition

$$L^*L(\hat{q} - q) = F'^*(\hat{q})S, \quad S = \{v \in H : ||v|| \leq \varepsilon\} \tag{6.19}$$

and by the following theorem, [74].

Theorem 10. *Assume that*

(1) F satisfies (6.17) and (6.18) with $\eta = l\sqrt{\tau_0}$, conditions (6.15) and (6.16) holds.

(2) The regularization sequence $\{\tau_k\}$ and the step size sequence $\{\alpha_k\}$ are chosen according to (6.3) and (6.5), respectively.

(3) Source condition (6.19) is satisfied.

(4) The linear operator L^*L is surjective and there is a constant $m > 0$ such that

$$\langle L^*Lh, h\rangle \geq m||h||^2, \quad \textit{for any } h \in H \tag{6.20}$$

(5) Constants defining F and the iteration are constrained by

$$\frac{M_2\varepsilon}{m} + \frac{d-1}{d\alpha} + \sqrt{\frac{\varepsilon}{m}\left(\frac{M_2}{2} + \frac{M_1^2}{(\sqrt{\rho}-1)^2}\right)} \leq 1 \tag{6.21}$$

$$\frac{||q_0 - \hat{q}||}{\sqrt{\tau_0}} \leq \frac{\varepsilon}{\sqrt{m}\left(1 - \frac{M_2\varepsilon}{m} - \frac{d-1}{d\alpha}\right)} = l \tag{6.22}$$

Then (1) For iterations (6.6)

$$\frac{||q_k - \hat{q}||}{\sqrt{\tau_k}} \leq l, \quad k = 0, 1, ..., \mathcal{K}(\delta) \tag{6.23}$$

(2) The sequence $\{\mathcal{K}(\delta)\}$ is admissible, i.e.

$$\lim_{\delta \to 0} ||q_{\mathcal{K}(\delta)} - z|| = 0, \tag{6.24}$$

z is $\arg\inf_{q \in D(F)} ||F(q) - g||_{H_1}$.

Proof. Since L^*L is surjective and there exists a constant $m > 0$, s.t.

$$\langle L^*Lh, h\rangle \geq m||h||^2, \text{ for any } h \in H \tag{6.25}$$

Since,

$$\langle F' * (q)F'(q)h, h\rangle = \langle F'h, F'h\rangle = ||F'h||^2 \geq 0$$

We have,

$$\langle [F'^*(q)F'(q)h + \tau L^*L]h, h\rangle \geq \tau m||h||^2$$

for arbitrary $\tau > 0$, $q \in D(F), h \in D(F)$. Furthermore, $[F'^*(q)F'(q)h + \tau L^*L]^{-1}$ exists, and setting $h = [F'^*(q)F'(q)h + \tau L^*L]^{-1}w$, we get

$$\begin{aligned}
\tau m||h||^2 &\leq \langle [F'^*(q)F'(q)h + \tau L^*L]h, h\rangle \\
&\leq ||h||||[F'^*(q)F'(q)h + \tau L^*L]h|| \\
\implies \tau m||h|| &\leq ||w|| \\
\implies \tau m||[F'^*(q)F'(q)h + \tau L^*L]^{-1}w|| &\leq ||w|| \\
\implies ||[F'^*(q)F'(q)h + \tau L^*L]^{-1}|| &\leq \frac{1}{\tau m}
\end{aligned}$$

and thus iterations (6.6) are well-defined. Let $\sigma_j = \frac{q_j - \hat{q}}{\sqrt{\tau_j}} \leq l$, for any $j, 0 < j \leq k < \mathcal{K}(\delta)$. Now for $0 < j \leq k \leq \mathcal{K}(\delta)$, we have

$$\begin{aligned}
F(q_k) &= F(\hat{q}) + F'(\hat{q})(q_k - \hat{q}) - B(q_k, \hat{q})(q_k - \hat{q})^2 \\
&= g + F'(q_k)(q_k - \hat{q}) - B(q_k, \hat{q})(q_k - \hat{q})^2, \text{ using (3)} \\
F(q_k) - g_\delta &= F'(q_k)(q_k - \hat{q}) - B(q_k, \hat{q})(q_k - \hat{q})^2 + g - g^\delta \qquad (6.26)
\end{aligned}$$

with $B(q_k, \hat{q}) \leq \frac{M_2}{2}$. From (6.6), we have

$$\begin{aligned}
q_{k+1} &= q_k - \\
&\quad \alpha_k[F'^*(q_k)F'(q_k) + \tau_k L^*L]^{-1}\{F'^*(q_k)(F(q_k) - g^\delta) + \tau_k L^*L(q_k - \hat{q})\} \\
\implies q_{k+1} - \hat{q} &= q_k - \hat{q} - \\
&\quad \alpha_k[F'^*(q_k)F'(q_k) + \tau_k L^*L]^{-1}\{F'^*(q_k)(F(q_k) - g^\delta) + \tau_k L^*L(q_k - \hat{q})\}
\end{aligned}$$

$$\begin{aligned}
\implies q_{k+1} - \hat{q} &= q_k - \hat{q} - \\
&\alpha_k A^{-1}\{F'^*(q_k)(F'(q_k)(q_k - \hat{q}) - B(q_k, \hat{q})(q_k - \hat{q})^2 + g - g^\delta) \\
&+ \tau_k L^* L(q_k - \hat{q})\}, \text{ using (6.26)} \\
&= q_k - \hat{q} - \\
&\alpha_k A^{-1} A(q_k - \hat{q}) - \\
&\alpha_k A^{-1} F'^*(q_k)\{-B(q_k, \hat{q})(q_k - \hat{q})^2 + g - g^\delta\} \\
&= (1 - \alpha_k)(q_k - \hat{q}) \\
&- \alpha_k A^{-1} F'^*(q_k)\{-B(q_k, \hat{q})(q_k - \hat{q})^2 + g - g^\delta + \tau_k v\} \\
&- \alpha_k \tau_k A^{-1}\{F'^*(q_k) - F'(\hat{q})\}v
\end{aligned}$$

we set $A = [F'^*(q_k)F'(q_k) + \tau_k L^* L]$ for convenience. For any bounded linear operator in a Hilbert space a polar decomposition holds. Hence

$$F'(q_k) = U|F'(q_k)|$$

where $|F'(q_k)| = (F'^*(q_k)F'(q_k))^{1/2}$ and U is a partial isometry. Denoting

$$A_k = F'^*(q_k)F'(q_k), \quad B = L^* L \quad C_k = A_k^{1/2} B^{-1/2}$$

we have

$$
\begin{aligned}
||[F'^*(q_k)F'(q_k) + \tau_k L^* L]^{-1} F'^*(q_k)|| &= ||(A_k + \tau_k B)^{-1} A_k^{1/2} U^*|| \\
&\leq ||(A_k + \tau_k B)^{-1} A_k^{1/2}|| \\
&= ||[B^{1/2}(B^{-1/2} A_k B^{-1/2} + \tau_k I) B^{1/2}]^{-1} A^{1/2}|| \\
&= ||B^{-1/2}(C_k^* C_k + \tau_k I)^{-1} C_k^*|| \\
&\leq ||B^{-1/2}|| \quad ||(C_k^* C_k + \tau_k I)^{-1} C_k^*|| \\
&\leq \frac{1}{\sqrt{m}} \max_{t \geq 0} \frac{\sqrt{t}}{t + \sqrt{\tau_k}} \leq \frac{1}{2\sqrt{\tau_k m}}
\end{aligned}
$$

Then,

$$
\begin{aligned}
||q_{k+1} - \hat{q}|| &\leq (1 - \alpha_k)||q_k - \hat{q}|| + \frac{\alpha_k}{2\sqrt{\tau_k m}} \left(\frac{M_2}{2} ||q_k - \hat{q}||^2 + \delta + \tau_k ||v|| \right) \qquad (6.27) \\
&\quad + \frac{\alpha_k M_2}{m} ||q_k - \hat{q}|| ||v|| \\
&\leq \left(1 - \alpha_k + \frac{\alpha_k M_2}{m} \epsilon \right) ||q_k - \hat{q}|| + \frac{\alpha_k}{2\sqrt{\tau_k m}} \left(\frac{M_2}{2} ||q_k - \hat{q}||^2 + \delta + \tau_k \epsilon \right)
\end{aligned}
$$

For $k < \mathcal{K}(\delta)$, we have,

$$
\begin{aligned}
\rho\delta &\leq ||F(q_k) - g||^2 \\
\implies \sqrt{\rho\delta} &\leq ||F(q_k) - g|| + ||g - g^\delta|| \leq M_1 ||q_k - \hat{q}|| + \delta \\
\implies \sqrt{\rho\delta} - \delta &\leq M_1 ||q_k - \hat{q}|| \\
\implies \delta &\leq \frac{M_1^2}{(\sqrt{\rho} - 1)^2} ||q_k - \hat{q}||^2, \text{ assuming } \delta < 1
\end{aligned}
$$

So,

$$||q_{k+1} - \hat{q}|| \leq \left(1 - \alpha_k + \frac{\alpha_k M_2}{m}\varepsilon\right) dl + \frac{\alpha_k}{2\sqrt{m}} \left(\frac{M_2}{2} + \frac{M_1^2}{(\sqrt{\rho}-1)^2}\right) l^2 d + \frac{\alpha_k d\varepsilon}{2\sqrt{m}}$$

From (6.21) we have,

$$\begin{aligned}\left(\frac{M_2}{2} + \frac{M_1^2}{(\sqrt{\rho}-1)^2}\right) &\leq \frac{m}{\varepsilon}\left(1 - \frac{M_2\varepsilon}{m} - \frac{d-1}{d\alpha}\right)^2 \\ &= \frac{\varepsilon}{l^2}, \quad \text{using (6.22)}\end{aligned}$$

Using the above inequality, we can write,

$$\begin{aligned}||q_{k+1} - \hat{q}|| &\leq \left(1 - \alpha_k + \frac{\alpha_k M_2}{m}\varepsilon\right) dl + \frac{\alpha_k d\varepsilon}{\sqrt{m}} \\ &= \left(1 - \frac{\alpha_k(d-1)}{d\alpha}\right) dl, \quad \text{using (6.22)} \\ &\leq l\end{aligned}$$

□

6.4 Statistical inverse problem

In this dissertation, we have combined the deterministic approach, such as IRGN, described in the previous section, with statistical inversion method. We used the Markov Chain Monte Carlo (MCMC) method and and Pilot Adaptive Metropolis algorithm. For details of these methods, see [78, 1]. For convenience, we present a summarization of the method for EIT and DOT in this section.

Since the forward problems for EIT and DOT are well-posed, we can obtain the probability from a observation vector $\widehat{g}$ given the values from the measurement noise ε and the conductivity distribution ρ using the dirac delta functions as

$$P(\widehat{g}|\rho,\varepsilon) = \delta(\widehat{g} - \Theta(\rho,\varepsilon)).$$

Assuming the independance of ρ and ε and the noise to be additive, i.e. $\widehat{g} = \Theta(\rho) + \varepsilon$, we get,

$$P(\rho,\widehat{g}) = P_{prior}(\rho)P_{noise}(\widehat{g} - \Theta(\rho)).$$

Thus the solution of the statistical inverse problem is,

$$P(\rho|\widehat{g}) = \frac{P_{prior}(\rho)P_{noise}(\widehat{g} - \Theta(\rho))}{c}.$$

where $c = P(\widehat{g})$.

Typically we suppose identical independent Gaussian measurement noise, $P_{prior}(\rho)$ as regularizing prior density as,

$$P_{prior}(\rho) \propto \begin{cases} \exp(-\alpha R(\rho) & \text{if } \rho_j > 0 \text{ for all } j \in \{1,2,...,m\} \\ 0 & \text{otherwise} \end{cases},$$

where $\alpha > 0$ and $R(\rho)$ is a regularizing function chosen as

$$R(\rho) = \beta_1 \sum_{i=1}^{m} \delta_i |\rho_i - \rho_i^*|^s + \beta_2 \sum_{j=1}^{z} d_j |\triangle_j \rho|,$$

where $\beta_1, \beta_2 > 0$ and $0 < s \leq 2$, ρ^* is a prior estimate of ρ.

Once the posterior distribution $P(\rho|\widehat{g})$ is obtained, then we use MCMC method to approx the Bayesian estimate.

6.4.1 Regularizing functions

In this dissertation, we use a combination of ℓ_1-type and TV priors for the statistical setting of the inverse problem. The ℓ_p regularization $R_{\ell_p}(y)$ is defined as

$$R_{\ell_p}(y) := \sum_{i=1}^{n} c_i |y_i - y_i^b|^p,$$

where c_i represent weights, $0 < p \leq 2$ is a constant and y^b the typical background from y. Note that $R_{\ell_p}(y)$ is a norm if $p \geq 1$ and would only define a metric in case $0 < p < 1$. For analytical methods it is usually necessary that the regularization function represents a norm, while for statistical reconstruction the case when $0 < p < 1$ can potentially also be handled.

The total variation regularization is defined as

$$R_{TV_c}(y_c) := \int_{\Omega} |\nabla y_c| dx,$$

where y_c the continuous version of the parameter of interest y. The discrete analogue for a two-dimensional body of the total variation regularization R_{TV_c} [49, 14] is

$$R_{TV}(y) := \sum_{i=1}^{h} l_i |\triangle_i y|,$$

where l_i is defined as the length of the edge corresponding to the i^{th} adjacent pixel and

$$\triangle_i = (0, 0, ..., 0, 1_{a_{(1,i)}}, 0, ..., 0, -1_{a_{(2,i)}}, 0, ..., 0),$$

with $a = (a_{(j,i)})_{i=1,\ j\in\{1,2\}}^{h}$ is the set containing the numbers of all adjacent pixel tuples $(a_{(1,i)}, a_{(2,i)})$.

6.4.2 The Markov Chain Monte Carlo method

An estimator for the true parameter q^* given the measurements g^* is found, i.e. the Bayesian estimator

$$E(q^*|g) = \int_{\mathbb{R}^n} q\pi_{q^*}(q|g)dq.$$

The Markov Chain Monte Carlo Method (MCMC) is then used to generate a large random sample $\{q^{(i)}\}_{i=B+1}^{N}$ from the posterior density $\pi_{q^*}(q|g)$ in order to approximate the Bayesian estimate by its sample mean,

$$E(q^*|g) = \int_{\mathbb{R}^n} q\pi_{q^*}(q|g)dq \approx \frac{1}{N-B}\sum_{i=B+1}^{N} q^{(i)}, \tag{6.28}$$

where N is the total number of samples and B is the burn in time. A pilot adaptive metropolis algorithm, [78], is used for generating this sample.

6.4.3 A pilot adaptive metropolis algorithm

The idea of this algorithm is to update the proposal distribution by changing its covariance matrix in such a way that the acceptance ratio of the chain after the last

adaption is close by the optimal acceptance ratio a_o of the chain.

Suppose we wish to perform M adaptions, one every m iterations, where $1 < mM < B < N$. The algorithm modifies the covariance matrix in the pilot time mM in such a way that it comes closer to one which has an optimal acceptance ratio. Then the standard Metropolis-Hastings algorithm begins with the latest state and proposal distribution of the pilot time.

Chapter 7

Computational Approach and Simulation

In this chapter, we discuss the computational approaches used for reconstructing the parameters in EIT and DOT. We also present all the numerical results and simulations. There are different methods to solve the forward problem. In this dissertation, we used the finite element method (FEM), as FEM can deal with more complex 2D or 3D geometries. Moreover, for elliptic problems, FEM is more suited to take boundary conditions into account because natural boundary conditions are included in the weak form of the equations. We represent the finite element descritization of the forward problems for CEM and DOT. Then we present the reconstructions of the EIT, CEM and DOT problems, using the proposed hybrid methods combining the deterministic, statistical and analytic methods, obtained by simulation for both synthetic and experimental data.

7.1 FEM formulation for CEM

FEM is the most traditional method for solving pde problems involving elliptic equations. To use FEM for the numerical solution to the forward problem, we need to find the variational form (weak form) of the equation. In chapter 2, we obtained the variational form for CEM as, for any $(v, V) \in H^1(\Omega) \times \tilde{\mathbb{R}}^L$,

$$b((u, U), (v, V)) = \sum_{l=1}^{L} I_l V_l \tag{7.1}$$

where $b((u, U), (v, V)) = \int_\Omega \sigma \nabla u \cdot \nabla v dx + \sum_{l=1}^{L} \frac{1}{z_l} \int_{e_l} (u - U_l)(v - V_l) dS$.
In FEM, the next step is to find a finite dimensional approximation to the solution of the above variational problem. Let $T = \{T_1, ..., T_{|T|}\}$ be the triangulation of Ω, which has N mesh points for the finite dimensional subspace H_N of $H_1(\Omega)$. Any $u_N \in H_N$ is represented by

$$u(x) \approx u_N(x) = \sum_{i=1}^{N} \alpha_i \phi_i(x), \text{ for } \alpha_i \in \mathbb{R},$$

where $\phi_i(x)$ are the basis functions of H_h satisfying $\phi_i(x_k) = \delta_{ik}$ for $i, k = 1, \ldots, N$. Electric potential on the electrodes is given by

$$U^L = \sum_{k=1}^{L-1} \beta_k \nu_k = G\beta,$$

where $\nu_k, k = 1, \ldots, L-1$ compose the basis for $\tilde{\mathbb{R}}^L$ are chosen as $\nu_1 = (1, -1, 0, ..., 0)^T$, $\nu_2 = (1, 0, -1, 0, ..., 0)^T \in \mathbb{R}^L$ etc., and $G \in \mathbb{R}^{L \times (L-1)}$. We must determine the coefficients α_i and β_k in this formulation. Choosing $v = \phi_i$ and $V = \nu_k$ when the set of test functions is of the form $(\phi_1, 0), ..., (\phi_N, 0), (\nu_1, 0), ..., (\nu_{L-1}, 0)$ results in the

following system of equations in matrix form:

$$\hat{A}\theta = f, \tag{7.2}$$

where $\theta = (\alpha, \beta)^T \in \mathbb{R}^{N+L-1}$, the matrix $\hat{A}$ is of the form,

$$\hat{A} = \begin{pmatrix} \hat{B} & Z \\ Z^T & D \end{pmatrix}$$

where,

$$\hat{B}(i,k) = b((\phi_i, 0), (\phi_k, 0)) = \int_\Omega \sigma \nabla \phi_i . \nabla \phi_k dx + \sum_{l=1}^{L} \frac{1}{z_l} \int_{E_l} \phi_i \phi_k ds \tag{7.3}$$

$$\text{for } i, k = 1, \ldots, N$$

$$D(i,k) = b((0, \nu_i), (0, \nu_k)) = \sum_{l=1}^{L} \frac{1}{z_l} \int_{E_l} (\nu_i)_l (\nu_k)_l ds, \tag{7.4}$$

$$\text{for } i, k = 1, ..., L-1 \text{ and}$$

$$Z(i,k) = b((\phi_i, 0), (0, \nu_k)) = \sum_{l=1}^{L} \frac{1}{z_l} \int_{E_l} \phi_i (\nu_k)_l ds \tag{7.5}$$

$$\text{for } i = 1, \ldots, N, \text{ and } k = 1, ..., L-1$$

and

$$f(i) = \begin{cases} 0 & \text{for } i = 1, \ldots, N \\ I^T \nu_{i-N} & \text{for } i = N+1, \ldots, N+L-1 \end{cases} . \tag{7.6}$$

If there are $P > 1$ current pattern, we can write α, β and I in matrix form as,

$$\alpha = \begin{pmatrix} \alpha_1^1 & \alpha_1^2 & \dots & \alpha_1^P \\ \alpha_2^1 & \alpha_2^2 & \dots & \alpha_2^P \\ \vdots & \vdots & \dots & \vdots \\ \alpha_N^1 & \alpha_N^2 & \dots & \alpha_N^P \end{pmatrix}, \beta = \begin{pmatrix} \beta_1^1 & \beta_1^2 & \dots & \beta_1^P \\ \beta_2^1 & \beta_2^2 & \dots & \beta_2^P \\ \vdots & \vdots & \dots & \vdots \\ \beta_{L-1}^1 & \beta_{L-1}^2 & \dots & \beta_{L-1}^P \end{pmatrix}, I = a \begin{pmatrix} 1 & 0 & \dots & -1 \\ -1 & 1 & \dots & 0 \\ 0 & -1 & \dots & 0 \\ \vdots & \vdots & \dots & \vdots \\ 0 & 0 & \dots & 1 \end{pmatrix}_{L \times M}$$

where a is the amplitude of the injected currents.

7.2 Numerical results for CEM, [1]

We generate synthetic data for our simulations with a known conductivity distribution σ. We proceed to solve the forward problem using σ using FEM. For each of the examples in this section, [1], we had two different discrete conductivity distributions inside a circular domain Ω. We used $|T| = 4128$ triangles and $N = 2129$ linear basis functions for u and σ on Ω. There are $L = 16$ equally spaced electrodes placed along the boundary with each electrode covering a surface area of 5mm. Next, we added random Gaussian noise with a standard deviation that is 1% and 3% of the maximum measurement, respectively. In order to avoid the inverse crime, we reconstructed σ on Ω with a smaller mesh size consisting of 1032 triangles with 549 mesh points.
Our simulations specifications are listed in the following table, which includes the known σ with a residual δ in (6.11) and a stopping rule for choosing ρ in (6.1).
The sequence of step lengths s_k is chosen through a backtracking strategy, $s_1, s_1/2, ...$ until either the strong Wolf condition from (6.9) or (6.10) is satisfied. The maximum

number of backtracking steps was set to 16. We also imposed $s_k > (\frac{\hat{d}-1}{\hat{d}})10^{-3}$ to prevent singularity in the numerical computation.

Note that, no backtracking is possible if the sequence of regularization parameter λ_k decreases too quickly. We define $\lambda_k = \frac{\lambda_1 c}{c+k-1}$ with $\lambda_1 = 1, c = 4$, to provide us with $\hat{d} = 1.25$.

Example 1. Single inclusion

The true conductivity consists of a homogeneous background and one circular inclusion of radius 0.01mm centered at (0.0242mm, 0.015mm). The conductivities of the background and the inclusions are $7 \cdot 10^{-4} Ohm$ and $10^{-8} Ohm$, respectively, as shown in Figure 7.1.

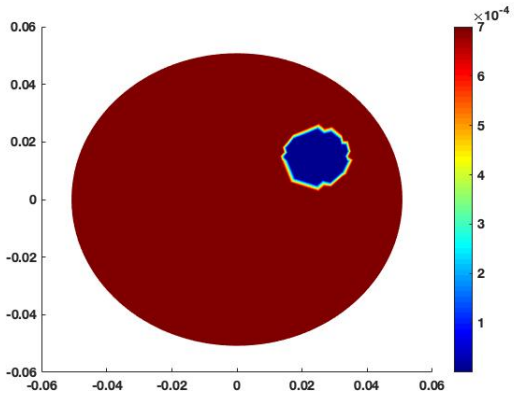

Figure 7.1: True conductivity distribution with single inclusion

The reconstructions with 1% and 3% noise levels are shown in Figures 7.2(a) and 7.2(c) for the IRGN method and Figures 2(b) and 2(d) for the statistical inversion method.

Inversion results from the IRGN method are smooth from Tikhonov regularization. The inclusion location is effectively captured, but its support is slightly larger than the true inclusion. In particular, its significantly extended towards the center of Ω

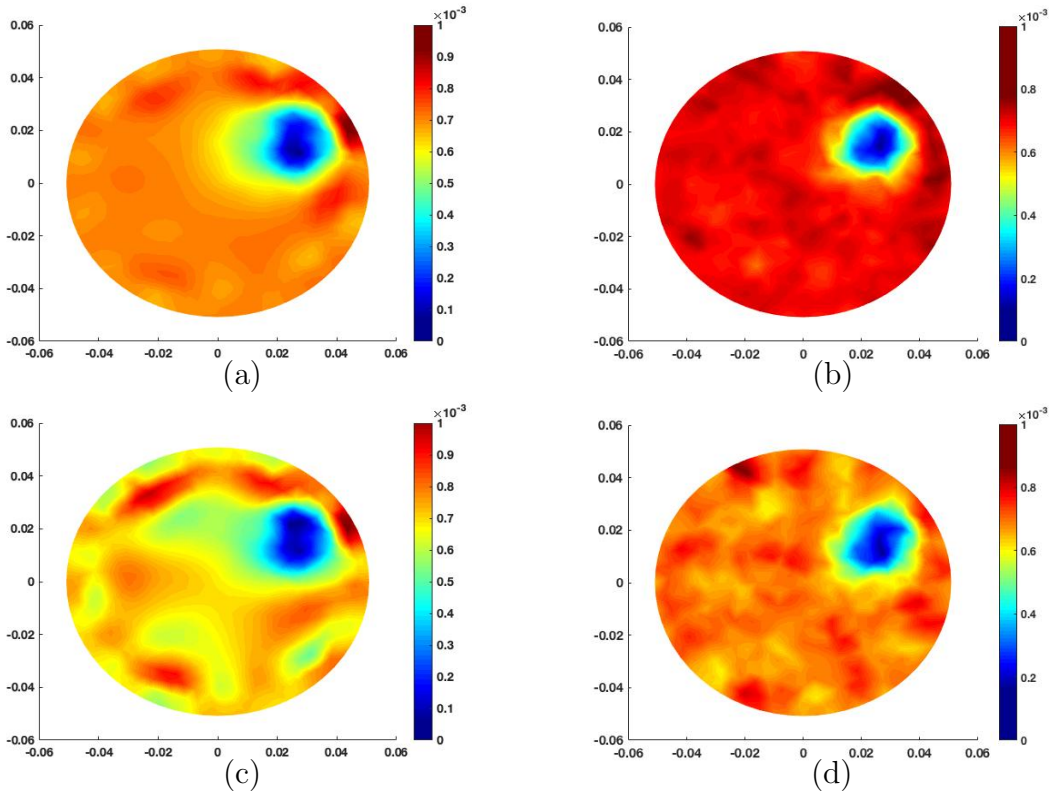

Figure 7.2: Reconstructions for Example 1: by IRGN method (a) with 1% noise, (c) with 3% noise; and by statistical inversion method (b) with 1% noise, (d) with 3% noise

when the noise level is higher at 3%. The magnitude of the inclusion conductivity is overestimated by $10^{-4}Ohm$ compared to the true value of $10^{-8}Ohm$. In contrast, the reconstruction by the statistical inversion method is more localized at the true location with a reasonably homogeneous background. However, with a higher noise level, the background conductivity starts to get distorted. We computed the ℓ_1 and ℓ_2 reconstruction errors as $e_1 = \frac{||\sigma_k - \sigma_T||_1}{||\sigma_T||_1}$ and $e_2 = \frac{||\sigma_k - \sigma_T||_2}{||\sigma_T||_2}$, where σ_T is the true conductivity distribution.

Example 2. Double inclusion

The true conductivity consists of a homogeneous background and double circular

	1% Noise		3% Noise	
	IRGN	Statistical Inversion	IRGN	Statistical Inversion
e_1	0.0677	0.0636	0.1196	0.0911
e_2	0.1187	0.1005	0.1598	0.1279

Table 7.1: Error comparison between IRGN and statistical inversion method for Example 1.

inclusions of radius 0.01mm centered at ($\pm$0.036mm, 0mm). The conductivities of the background and the inclusions are $7 \cdot 10^{-4} Ohm$ and $10^{-8} Ohm$, respectively, as shown in Figure 7.3.

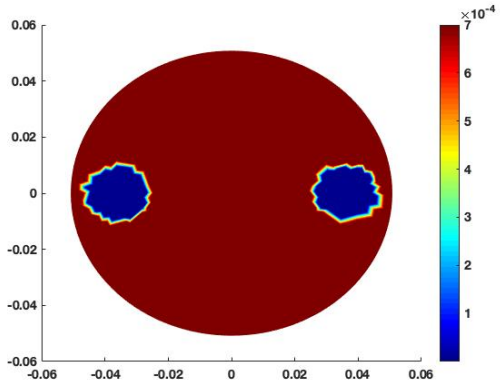

Figure 7.3: True conductivity distribution with double inclusions

	1% Noise		3% Noise	
	IRGN	Statistical Inversion	IRGN	Statistical Inversion
e_1	0.1194	0.0946	0.1225	0.1063
e_2	0.1725	0.1347	0.1775	0.1520

Table 7.2: Error comparison between IRGN and statistical inversion method for Example 2.

The reconstructions with 1% and 3% noise levels are shown in Figures 7.4(a) and 7.4(c) for the IRGN method and Figures 7.4(b) and 7.4(d) for the statistical inversion method. We observe that both methods are able to retrieve the inclusions. In IRGN method, the supports of the inclusions are extended towards the center of Ω, and the

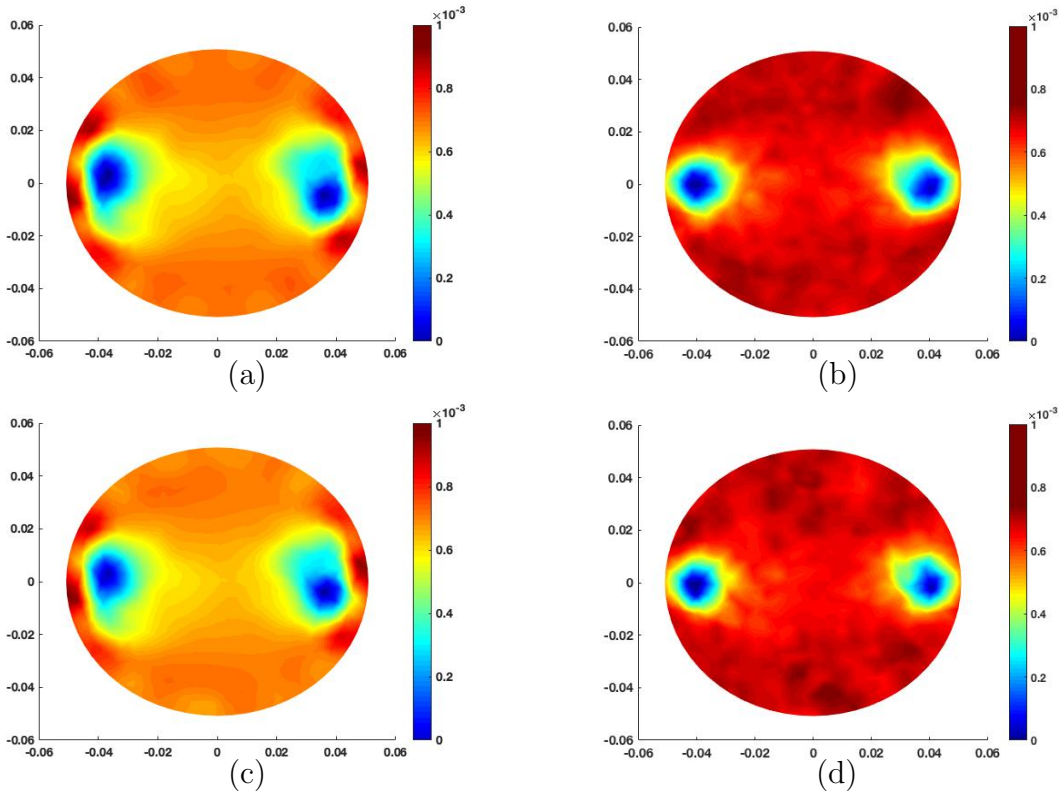

Figure 7.4: Reconstructions for Example 2: by IRGN method (a) with 1% noise, (c) with 3% noise; and by statistical inversion method (b) with 1% noise, (d) with 3% noise

magnitude of the background conductivity is slightly overestimated. However, the statistical approach provides a more localized solution with a sharper background. We list the reconstruction errors for σ in Table 3, which shows that the errors e_1 and e_2 are smaller for the statistical inversion method.

Example 3. Quadruple inclusion

The true conductivity consists of a homogeneous background and double circular inclusions of radius 0.01mm centered at ($\pm$0.036mm, 0mm) and (0mm, $\pm$ 0.036mm). The conductivities of the background and the inclusions are $7{\cdot}10^{-4}Ohm$ and $10^{-8}Ohm$,

respectively, as shown in Figure 7.5. Multiple inclusions are challenging for most

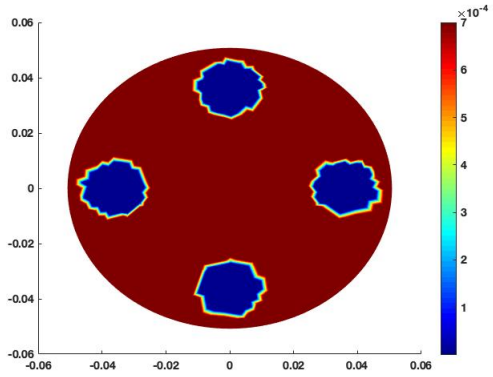

Figure 7.5: True conductivity distribution with four inclusions

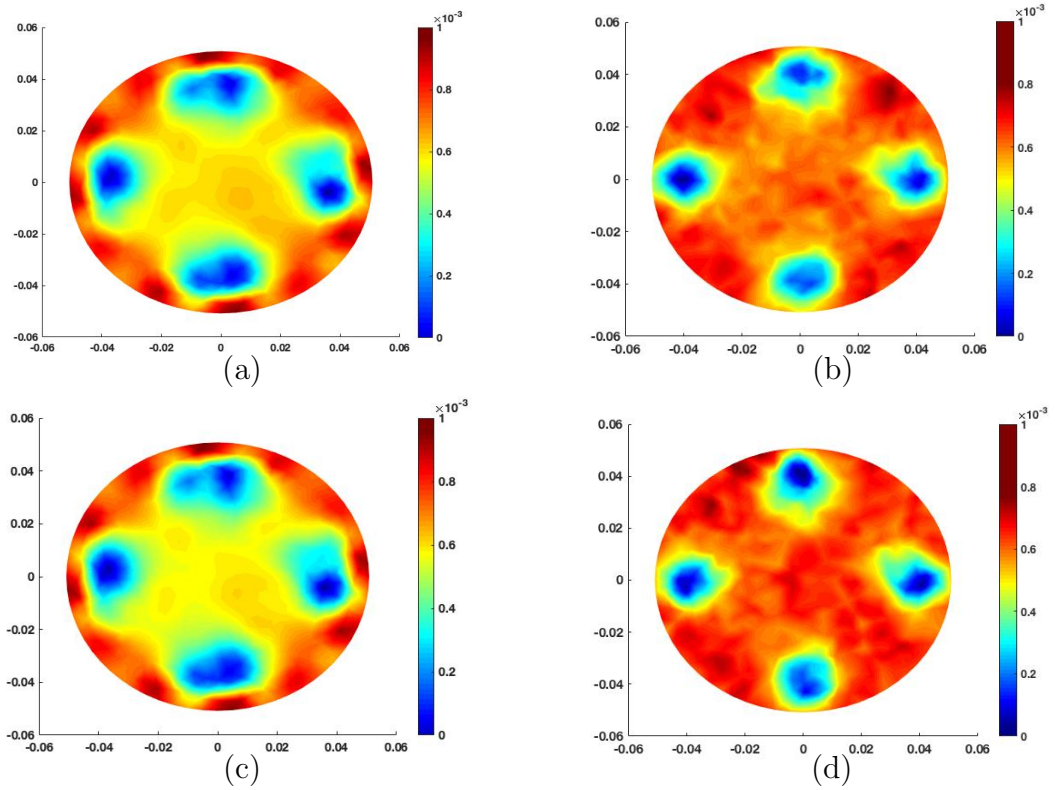

Figure 7.6: Reconstructions for Example 3: by IRGN method (a) with 1% noise, (c) with 3% noise; and by statistical inversion method (b) with 1% noise, (d) with 3% noise

numerical algorithms. However, both the approaches we used in this paper produce

reasonable reconstructions of σ for different noise levels. As expected, with higher noise level and more inclusions, their support becomes larger in IRGN method, eventually making them barely observable. On the other hand, the statistical inversion does produce significantly sharper images with more localized inclusions even for a higher noise level.

	1% Noise		3% Noise	
	IRGN	Statistical Inversion	IRGN	Statistical Inversion
e_1	0.2201	0.2016	0.2274	0.2028
e_2	0.2563	0.2370	0.2609	0.2387

Table 7.3: Error comparison between IRGN and statistical inversion method for Example 3.

Example	$\delta_{1\%}$	$\delta_{3\%}$	ρ
1	0.0328	0.0812	2
2	0.0590	0.1265	2
3	0.0616	0.1643	2

Table 7.4: Choice of δ and ρ for different examples

7.3 FEM formulation for DOT

In chapter 3, we obtained the variational form for DOT as, for any $u, v \in H^1(\Omega)$,

$$B(u,v) = \frac{1}{2}\int_{\partial\Omega} g\bar{v}ds \tag{7.7}$$

where $B(u,v) = \int_\Omega D\nabla u \cdot \nabla v dx + \int_\Omega \mu_a u\bar{v}dx + \frac{1}{2}\int_{\partial\Omega} u\bar{v}ds$.

In FEM, the next step is to find a finite dimensional approximation to the solution of the above variational problem. Let $T = \{T_1, ..., T_{|T|}\}$ be the triangulation of Ω, which

has N mesh points for the finite dimensional subspace H_N of $H_1(\Omega)$. Any $u_N \in H_N$ is represented by

$$u(x) \approx u_N(x) = \sum_{i=1}^{N} \alpha_i \phi_i(x), \text{ for } \alpha_i \in \mathbb{R},$$

where $\phi_i(x)$ are the basis functions of H_h satisfying $\phi_i(x_k) = \delta_{ik}$ for $i, k = 1, \ldots, N$. Substituting $u(x)$ by the above form and choosing $v = \phi_i$ for $i = 1, ..., N$ in (7.7) results in the following system of equations in matrix form:

$$S\theta = f, \tag{7.8}$$

where $\theta = (\alpha_1, ..., \alpha_N)^T \in \mathbb{R}^N$,

$$S_{i,j} = \int_\Omega D\nabla\phi_i \cdot \nabla\phi_j dx + \int_\Omega \mu_a \phi_i \bar{\phi}_j dx + \frac{1}{2}\int_{\partial\Omega} \phi_i \bar{\phi}_j ds, \text{ for } i, j = 1, \ldots, N$$
$$f(i) = \frac{1}{2}\int_{\partial\Omega} g\bar{\phi}_i, \text{ for } i = 1, ..., N.$$

Solving (7.8) for θ, we get the solution of the forward DOT problem.

7.4 Numerical results for DOT

In this section, reconstructions using a pilot adaptive Metropolis algorithm [78, 1] are presented. The photon density measurements were simulated on a mesh of 2097 triangles (Figure 7.7.A), then 1% Gaussian measurement noise has been added to the measurements. The reconstructions where made, based on the noisy measurement on a mesh of 541 triangles (Figure 7.7.B). The mesh for the simulations and the

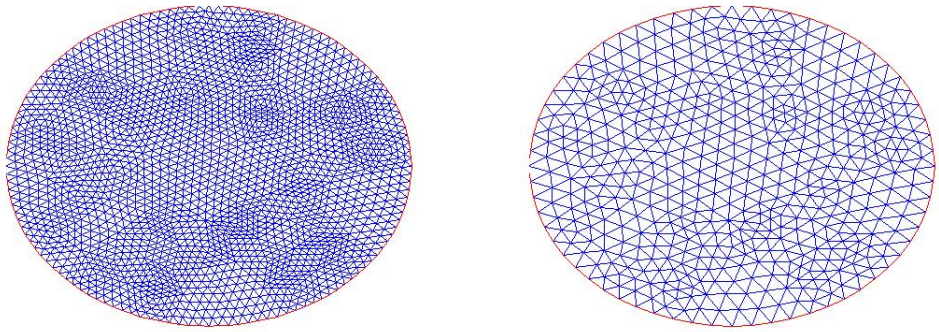

A B

Figure 7.7: A: Mesh containing 2097 triangles used for simulating measurements. B: Mesh containing 541 triangles used for the parameter reconstruction.

reconstructions were chosen to be different in order to avoid committing an inverse crime. We assume that the parameters of interest are known and constant on the boundary, hence the number of parameters to be estimated for D and μ where with 477 parameters somewhat smaller then the number of triangles. Note that in order to reduce the computational time the starting guess $x^{(0)} \in E$ has been selected to be the reconstruction after a few iterations of IRGN method. In all reconstructions we choose to perform $M = 600$ adaptions, one every $m = 50$ iterations, e.i. the pilot time was chosen to be $mM = 30.000$. Further, the burn in time was chosen to be $B = 100.000$ and the total number of samples was $N = 150.000$. We run this method until convergence at approximately 150 iterations and compared with the result obtained from IRGN method.

In figures 7.8-7.11, image A and B represent the true parameters μ and D in mesh 7.7.A, images C-D and E-F are the corresponding reconstructions using the TV reconstruction and a mixture of the TV and the ℓ_1 regularization (general regularization), respectively, from photon density measurements with 1% additive relative Gaussian noise. It can be seen that both, the reconstructions with the TV, and the mixed TV

and ℓ_1, regularizations obtain relatively good reconstructions from the true parameters. However, in the presence of multiple inclusions (Figure 7.9) or more complex inclusions (Figure 7.10 and 7.11) the mixed regularization seems to outperform the TV regularization. Note that in figures G-H, which represent reconstructions with the IRGN method.

Clearly, the reconstructions are strongly dependent on the choice of the regularization parameters. There is a vast literature for choosing optimal regularization parameters for linear problems. However, there are, to our knowledge, no good methods for nonlinear problems like DOT. Hence, we chose the parameters add hock. That is we used a computer cluster to run the algorithm with large set of regularization parameters choices, then we evaluated the reconstructions and picked the visually best parameters for the TV and the mixed regularizations. Note that once this parameter was found it was kept fixed for all reconstructions in figures 7.8-7.11.

Example	Example 1	Example 2	Example 3	Example 4
ξ	0.0018	0.0016	0.0016	0.0019
Residual, E_N	0.0124	0.0101	0.01335	0.01302
Residual, E_S	0.0129	0.0153	0.0139	0.0139

Table 7.5: Numerical results for noiselevel ξ and residual error, $E = ||F(q) - g^\delta||_2^2$ (i) E_N using IRGN and (ii) E_S using Statistical inversion for 1% noise

Relative Noise Level	l_1 error (TV)	l_1 error (GR)	l_1 error (IRGN)	l_2 error (TV)	l_2 error (GR)	l_2 error (IRGN)
1%	0.1447	0.1337	0.1234	0.3245	0.3398	0.3230
5%	0.1439	0.1347	0.1206	0.3192	0.3423	0.3212
10%	0.1462	0.1355	0.1258	0.3272	0.3390	0.3257
15%	0.1442	0.1328	0.1315	0.3232	0.3368	0.3287
20%	0.1404	0.1358	0.1144	0.3129	0.3441	0.3268

Table 7.6: Relative Numerical Errors of μ

In Table 7.6 and 7.7 the relative error of reconstructions of μ and D with different

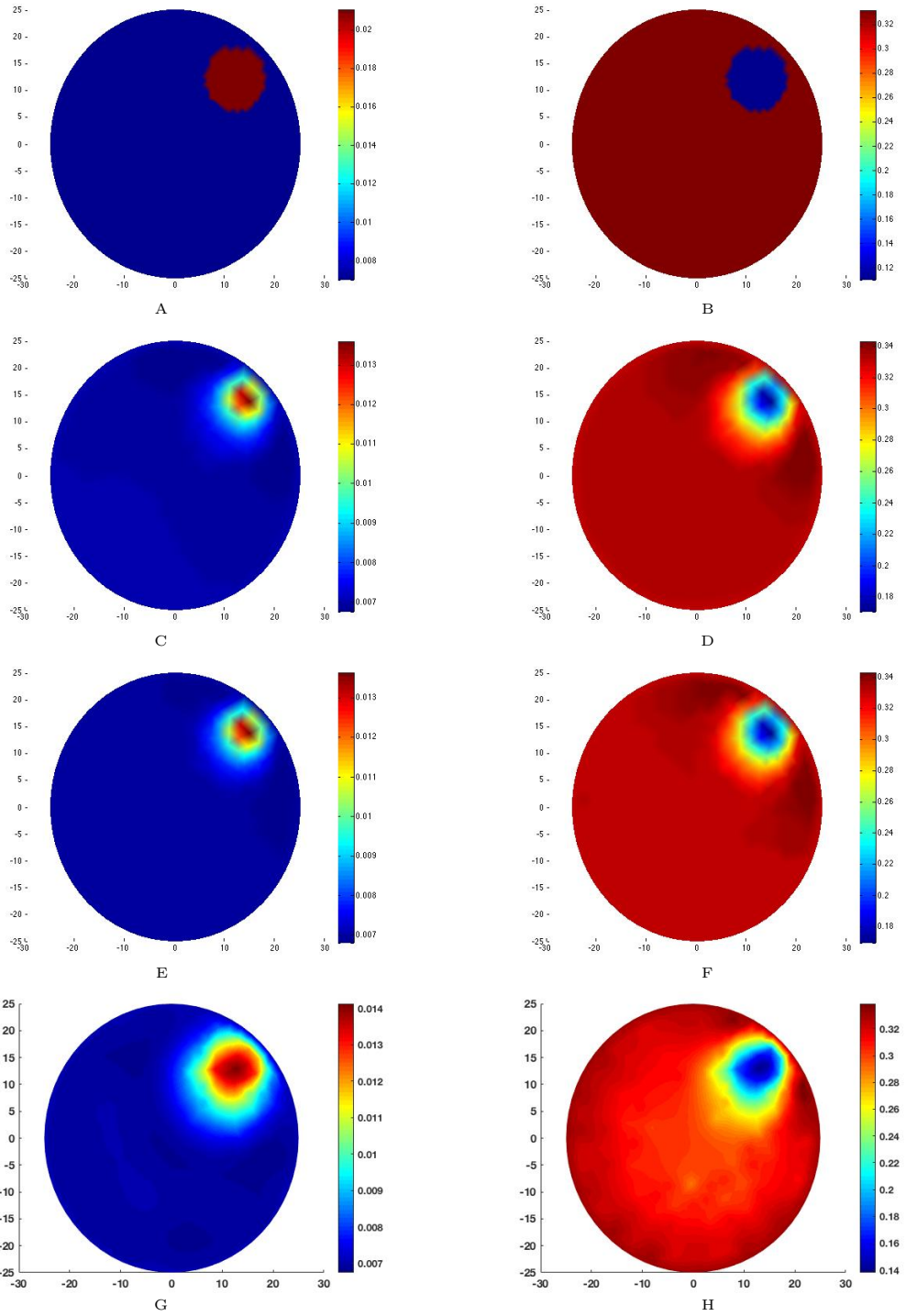

Figure 7.8: A & B: The true parameters μ and D in the simulation mesh (Figure 7.7.A). Reconstructions of the parameters μ and D from measurements with 1% additive Gaussian noise, C & D: using the TV regularization (adapted from [79]) E & F: using a mixture of the TV and ℓ_1 regularization (adapted from [79]), G & H: using IRGN Method.

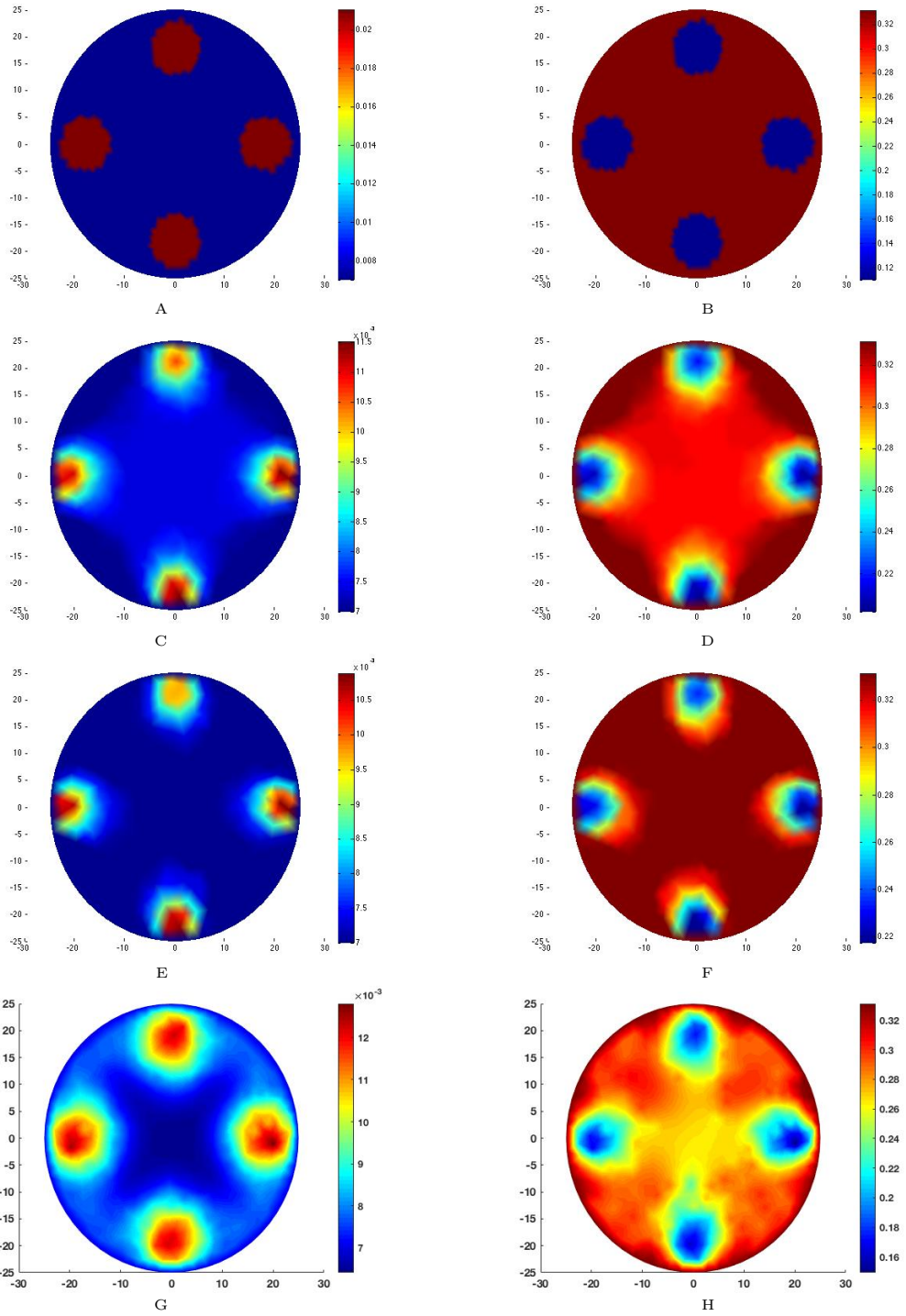

Figure 7.9: A & B: The true parameters μ and D in the simulation mesh (Figure 7.7.A). Reconstructions of the parameters μ and D from measurements with 1% additive Gaussian noise, C & D: using the TV regularization (adapted from [79]), E & F: using a mixture of the TV and ℓ_1 regularization (adapted from [79]), G & H: using IRGN Method.

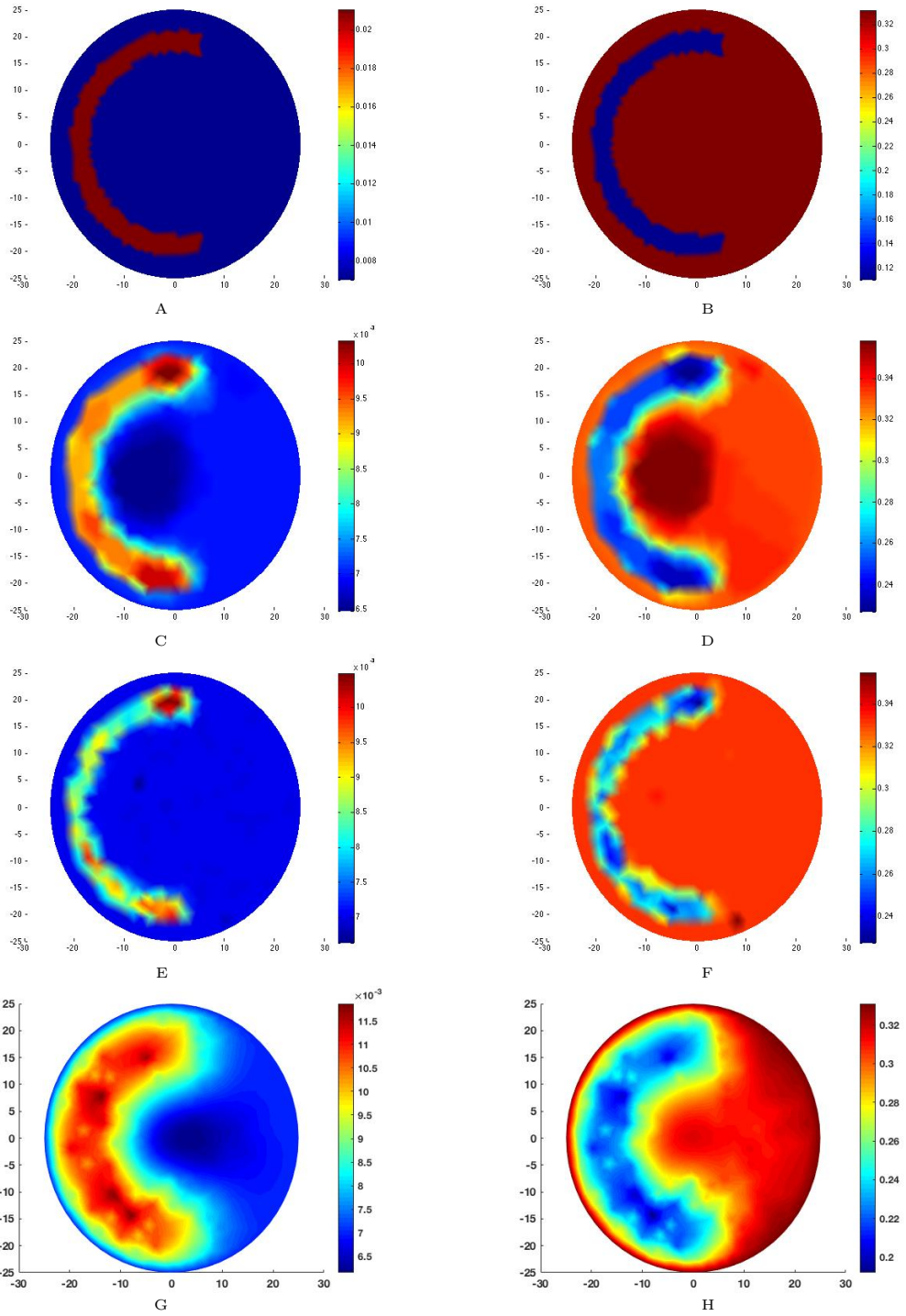

Figure 7.10: A & B: The true parameters μ and D in the simulation mesh (Figure 7.7.A). Reconstructions of the parameters μ and D from measurements with 1% additive Gaussian noise, C & D: using the TV regularization (adapted from [79]), E & F: using a mixture of the TV and ℓ_1 regularization (adapted from [79]), G & H: using IRGN Method.

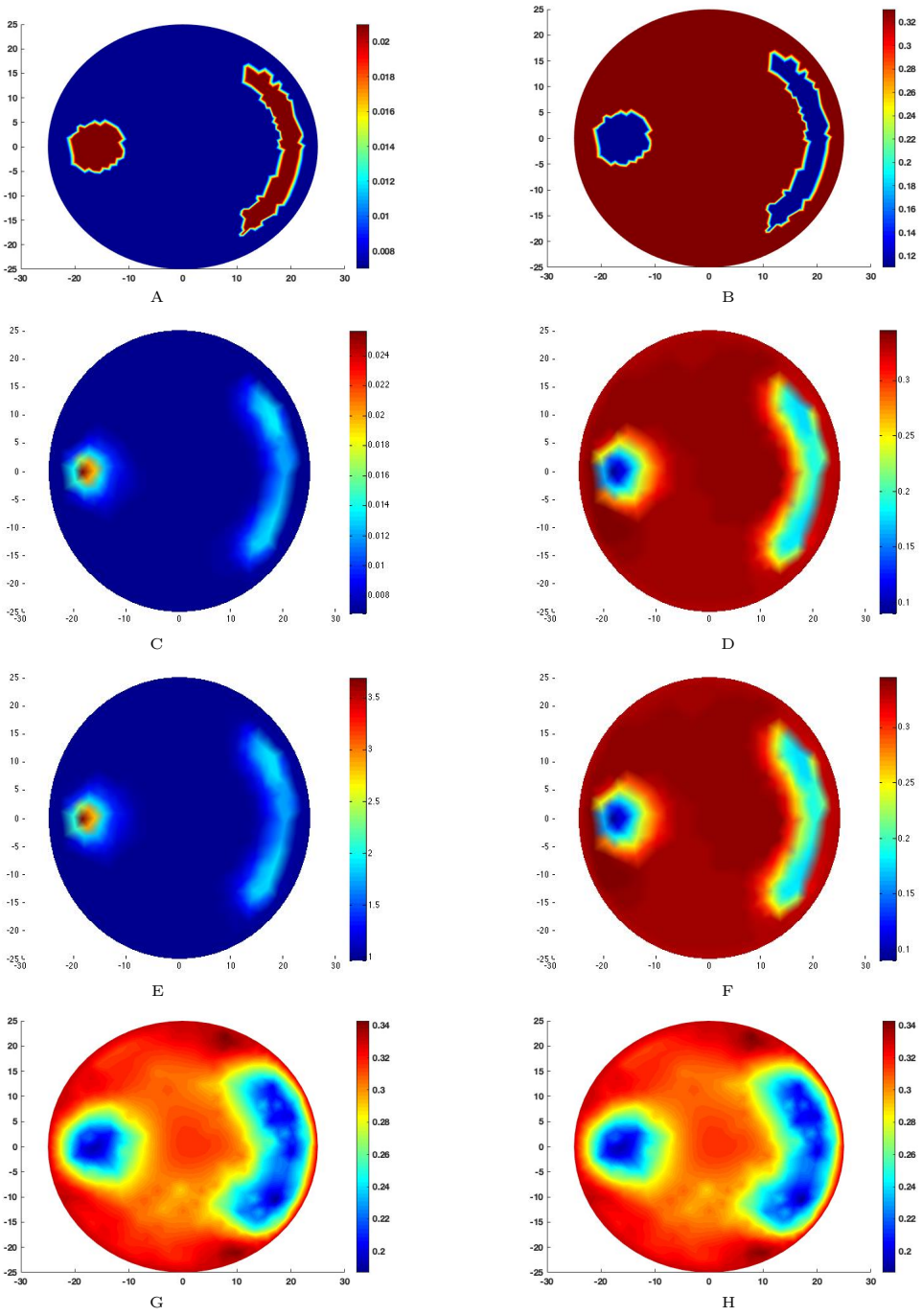

Figure 7.11: A & B: The true parameters μ and D in the simulation mesh (Figure 7.7.A). Reconstructions of the parameters μ and D from measurements with 1% additive Gaussian noise, C & D: using the TV regularization (adapted from [79]), E & F: using a mixture of the TV and ℓ_1 regularization (adapted from [79]), G & H: using IRGN Method.

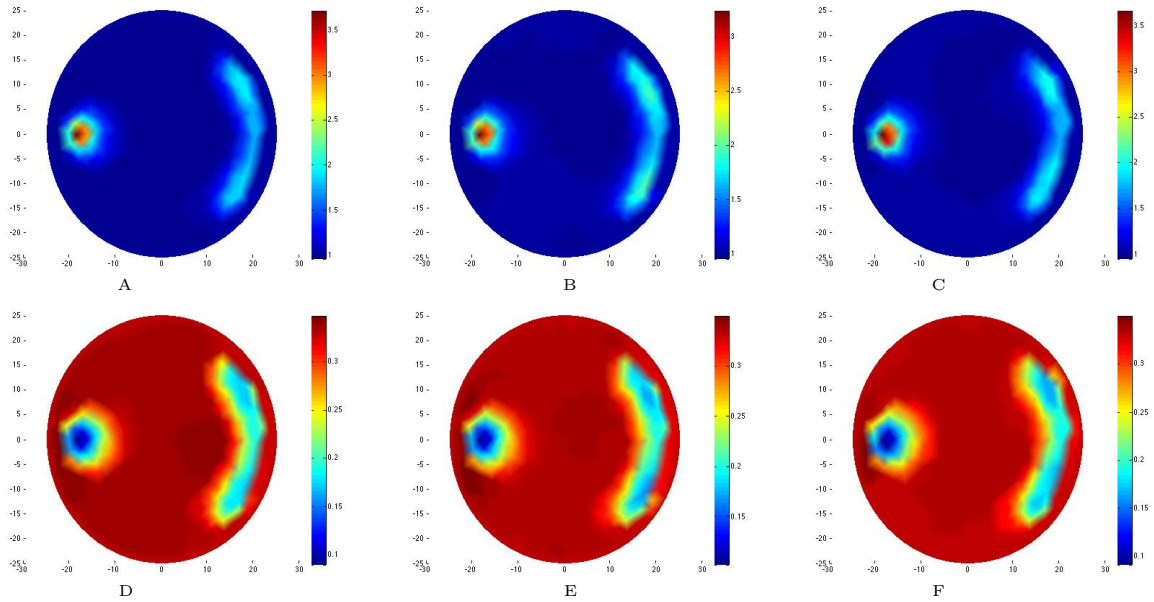

Figure 7.12: Reconstruction of μ and D using statistical inversion method with, A, D: 5% noise, B, E: with 10% noise, C, F: with 20% relative additive Gaussian noise, respectively, figures adapted from [79].

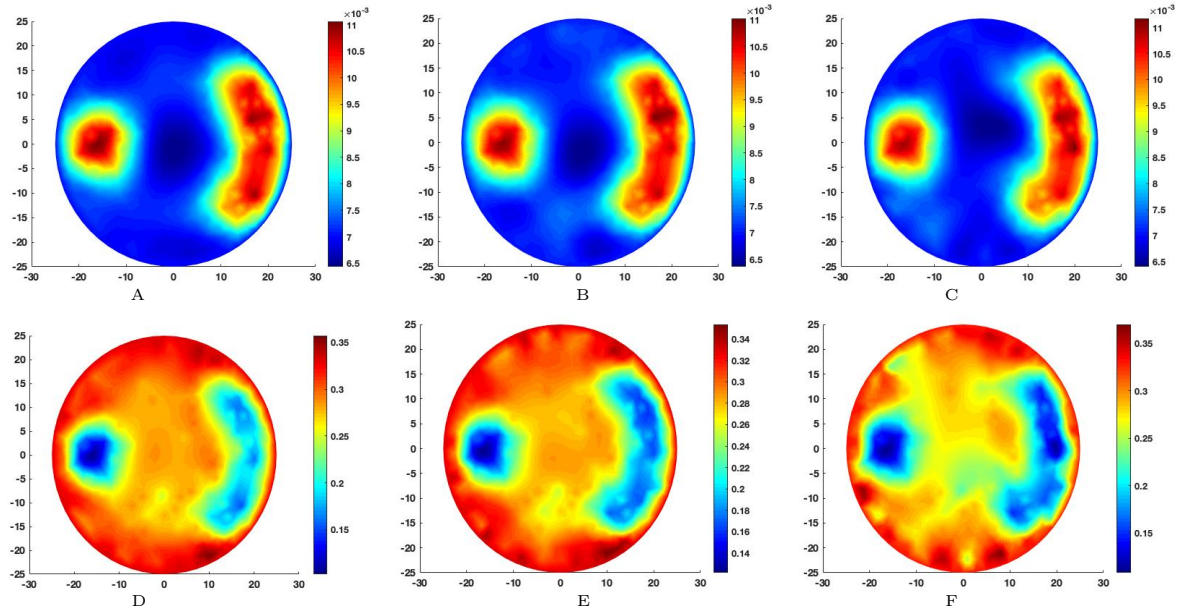

Figure 7.13: Reconstruction of μ and D using IRGN method with, A, D: 5% noise, B, E: with 10% noise, C, F: with 20% relative additive Gaussian noise, respectively.

Relative Noise Level	l_1 error (TV)	l_1 error (GR)	l_1 error (IRGN)	l_2 error (TV)	l_2 error (GR)	l_2 error (IRGN)
1%	0.0625	0.0470	0.1002	0.1189	0.1227	0.1259
5%	0.0625	0.0455	0.0930	0.1161	0.1198	0.1192
10%	0.0638	0.0462	0.1159	0.1199	0.1216	0.1423
15%	0.0632	0.0449	0.1363	0.1204	0.1203	0.1653
20%	0.0598	0.0474	0.0923	0.1158	0.1242	0.1171

Table 7.7: Relative Numerical Errors of D

relative noise levels are listed. Note that the relative error of μ is defined as $\frac{||\mu_t - \mu_r||_{L_p}}{||\mu_t||_{L_p}}$, were μ_t represents the true parameter to be estimated and μ_r the reconstruction of μ_t. The relative error of D is defined analogous. In table 7.6 and 7.7 the relative l_1 and l_2 errors from the reconstructions using the Total Variation regularization (TV), the general regularization (GR) as well as with the IRGN method have been computed. As expected the reconstructions with using the Total Variation have mostly a smaller l_2 relative errors while reconstructions using the general regularization have mostly a smaller l_1 relative errors. We observe that, both the statistical inversion method and the IRGN method become unstable for higher noise level, as expected.

7.5 Proposed hybrid approach for EIT

A computational disadvantage of iterative algorithm is that, the accuracy of the solution depends on the initial guess. To overcome this disadvantage, we propose a hybrid algorithm for EIT, where the initial solution is obtained by using the mollifier regularization technique, discussed in chapter 5 under suitable assumptions. Using the solution as an initial guess, we apply the IRGN method which provides an improved approximation to the desired conductivity distribution. In this section, we present the

reconstruction of the conductivity distribution using the mollifier approach. We then presented the results obtained by combining the mollifier approach and the IRGN method.

We reconstructed a conductivity distribution of an off-centered high conductivity

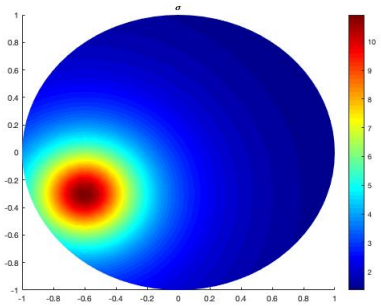

Figure 7.14: Conductivity distribution $\sigma(x, y)$

region with a constant background defined as,

$$\sigma(x, y) = 1 + \frac{1}{(x + 0.6)^2 + (y + 0.3)^2 + 0.1}$$

see Figure 7.14.

The reconstruction is obtained very rapidly, and same resolution, $\gamma = 0.1$, is used for all reconstruction points. σ is reconstructed with noise free data for different current patterns. Based on the table 7.8, we fixed the current pattern $j(\theta) = \cos\theta$ as our

Current pattern	$j(\theta) = \cos\theta$	$j(\theta) = \sin\theta$	$j(\theta) = \cos 3\theta$
l_2 rel error	0.85256	2.0983	1.00457

Table 7.8: Relative error in σ for different current patterns with noise free data

optimal choice of current.

From table 7.9, we see that mollifier regularization can be used to obtain a decent estimation to the parameter distribution in EIT. However, the proposed hybrid ap-

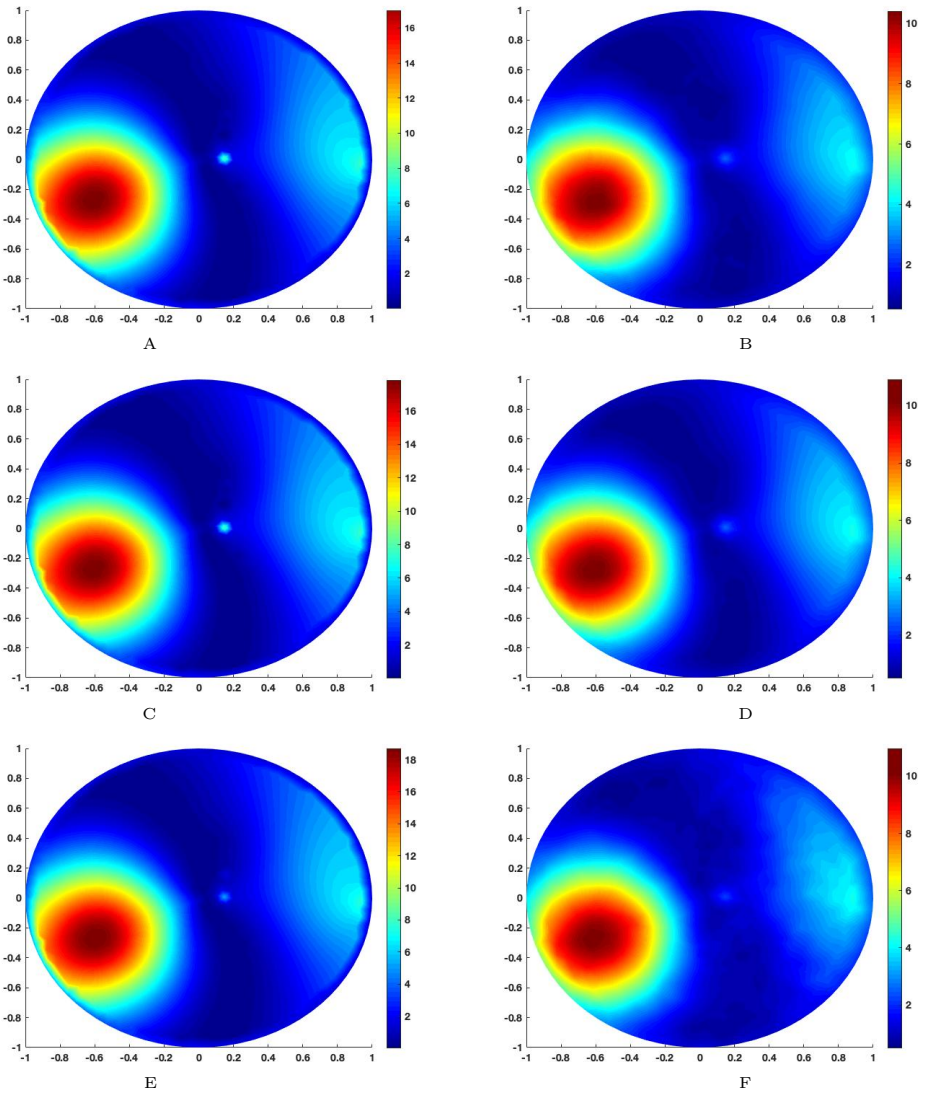

Figure 7.15: Reconstructed conductivity distribution, (A, C, E) using mollifier regularization, (B, D, E) using hybrid approach, with noise free, 1%, and 3 % noise in data

Relative noise level	Mollifier approach	Hybrid Approach
0%	0.85256	0.29883
1%	0.85459	0.30985
3%	0.92345	0.30914

Table 7.9: Relative error, ℓ_2, table for mollifier and hybrid approaches for different noise levels

proach, which uses the mollifier estimate as an initial guess and update the solution using the classical IRGN method, can improve the estimate significantly. The reconstructions for different noise levels are shown in Figure 7.15. We note that, the mollifier approach does not provide better estimate for high noise level, as expected, as well as the hybrid approach.

7.6 Reconstructions from real data

With the advancements in computational power in recent years, real world applications of the hybrid approaches have become feasible. We applied the hybrid method to study the corrosion of concrete using experimental EIT data. This is particularly interesting because it has potential applications to test the degradation of concrete constructions such as bridges.

We used 16 electrodes as shown in figure 7.16. Two neighboring electrodes are specially assigned, i and $i+1$, one for direct current injection (positive) and the other for direct current injection (negative). For each fixed direct current injection, I, we measure 13 voltages, V. It is physically impossible to obtain those voltage observations in a direct way. But we are able to measure the electrical potentials, U. Hence, the potential observations can be converted into voltage observations making use of the additional condition that

$$\sum_{j\in\{i+2,\ldots,i+15\}} U_j^i = 0, \text{ where } i,j \in \mathbb{Z}/16\mathbb{Z} \tag{7.9}$$

that is, the potential difference between two adjacent electrodes, i.e. we define the j^{th} voltage from the i^{th} current injection as $V_j^i := U_{j+1}^i - U_j^i$, where $j \in \{i+2, i+$

$3, ..., i+14\}$. Solving the following system, we compute the voltages.

$$\left[\begin{array}{ccccc|c} U^i_{i+2} & U^i_{i+3} & \dots & U^i_{i+14} & U^i_{i+15} & 0 \\ -U^i_{i+2} & U^i_{i+3} & \dots & 0 & 0 & V^i_{i+2} \\ 0 & -U^i_{i+3} & \dots & 0 & 0 & V^i_{i+3} \\ \vdots & \vdots & \ddots & \vdots & \vdots & \vdots \\ 0 & 0 & \dots & U^i_{i+14} & 0 & V^i_{i+13} \\ 0 & 0 & \dots & -U^i_{i+14} & U^i_{i+15} & V^i_{i+14} \end{array}\right]$$

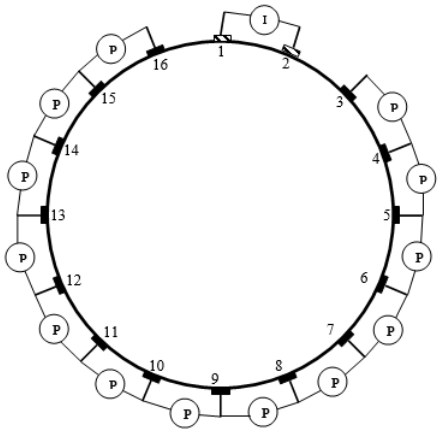

Figure 7.16: Sixteen electrodes connected to the body Ω. Here, electrode 1 represents the input current and electrode 2 the output current and $U^1_j = U_{j,j+1}$ with $j \in \{3, 4, ..., 15\}$ represents the thirteen corresponding potential measurements.

7.6.1 Description of the experiment and reconstructions

A mortar cylinders, of $100mm$ diameter and $200mm$ hight, with water-to-cement ratio of 0.47 and aggregate content of 40% of cement were cast according to ASTM C192-06. Type I Ordinary Portland Cement (OPC) and natural sand were used to

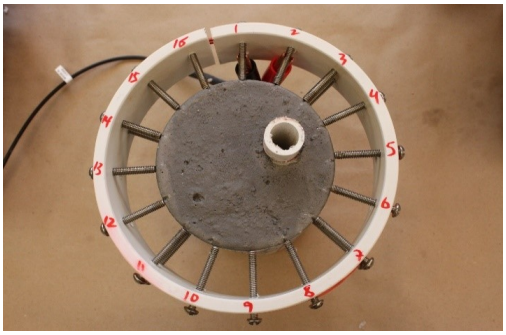

Figure 7.17: Concrete cylinder.

cast the cylinders. A PVC pipe of $25.4mm$ diameter was embedded into the sample to simulate the damage. The pipe was located at the midpoint of surface center and boundary, as shown in Figure 7.17. Then, the samples cured for 28 days in 100% humidity and $25°C$ temperature before performing the test. Cylinders were removed from the curing room and left in laboratory condition for a week. This time allowed the surface moisture on the samples to be dried out. Then, a nickel-based conductive paint was sprayed on top of the cylinder, as shown in Figure 7.17.

The EIT equipment for data acquisition is shown in Figure 7.18, the system consisted of a Keithley 6221 low-noise AC/DC current source, a Keithley model 2700 high resolution multi-meter and switch system, computer and a PVC ring that carrying electrodes. Stainless steel screws were used as the electrodes. There were 16 electrodes equally distributed around the PVC ring (Figure 7.17) as described by the model. As described earlier, the current was injected at two adjacent electrodes in a clockwise fashion, then the potentials were measured on every two neighboring electrodes. $10mA$ was used as the amplitude of injected direct current in this investigation. Statistical inversion was used to reconstruct the conductivity of the concrete cylinder based on the obtained measurements. The reconstruction was performed

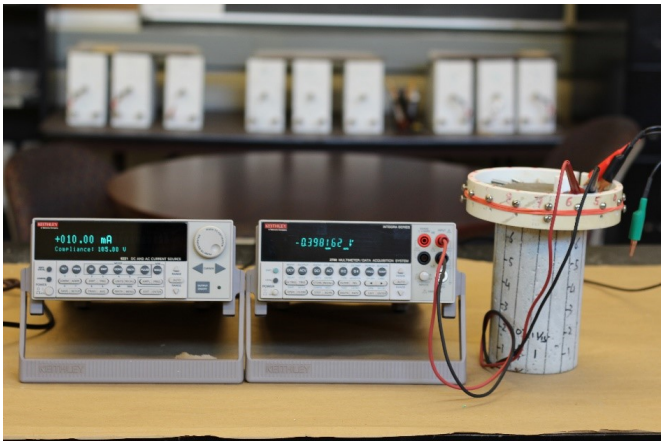

Figure 7.18: EIT equipment for data acquisition

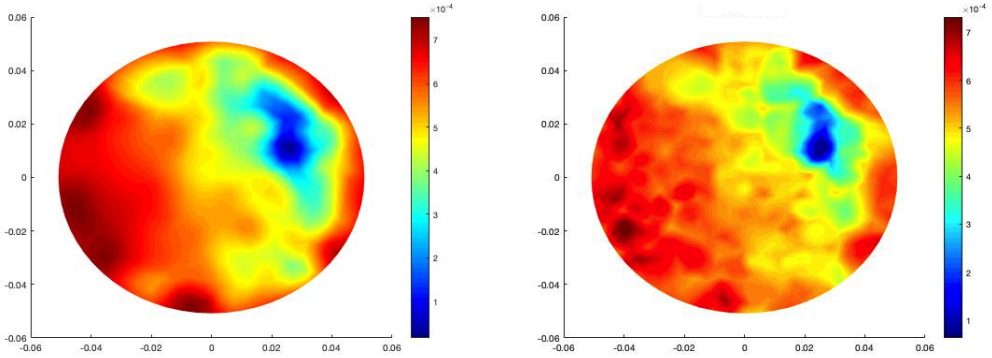

(a) (b)

Figure 7.19: Reconstruction of a plane of the concrete cylinder in Figure 7.17. (a) IRGN method (b) statistical inversion method

in the in reconstruction mesh (Figure 7.7.b) of 281 triangles. A TV regularization (Figure 7.19.a.) as well as a combination of the TV and the ℓ_1 regularization (Figure 7.19.b.) have been used. A ℓ_1 regularization has not been used because the conductivity of concrete is not exactly known, i.e. the conductivity of concrete depends from many variables such as humidity, age and mixture. Both obtained reconstructions (Figure 7.19) seem to be reasonably good. Note that with real data considerable worse reconstructions should be expected in comparison to the simulated data case. This is because the measurement noise might not be Gaussian as assumed in our model. Further, the conductivity of concrete is generally not constant because it depends from the humidity and mixture in each coordinate of the object.

Chapter 8

Conclusions and Discussion

In this dissertation, we proposed a hybrid techniques for solving the inverse problem in EIT and DOT. We investigated a direct method for EIT using mollifier regularization that was modified and extended to solve the inverse problem in DOT. The extension to DOT method requires existence of eigen-functions of non-symmetric operators, which do exist; however, finding the analytical form is not tractable. Therefore, we used the symmetric eigenfunctions as an approximation for the DOT mollifiers. Appropriate formulation of the mollifier method is implemented and an appropriate algorithm is devised for verification of the efficacy of the proposed method. For both EIT and DOT, a comprehensive numerical and computational comparison of several types of regularization techniques, ranging from analytical to iterative to statistical method, was presented. Based on the results of the comparison of the regularization methods, a novel hybrid method combining the deterministic (mollifier and iterative) and statistical (iterative and statistical) was proposed. The efficacy of the proposed method was then further investigated via simulations and using experimental data

for damage detection in concrete.

We also formulated the EIT forward model using the CEM as the Galerkin finite element approximation and also provided justification for the linearization for solving the inverse problem. We investigated several regularization methods for the inverse problem ranging from deterministic, analytical and iterative method, and to statistical method. We performed a comprehensive comparison between the regularization functions for the statistical inverse problem and the regularization functions for the deterministic case. We used the statistical algorithm that uses a Bayes' estimate for the unknown parameter that implements a smoothing criteria and enforces sparsity in the prior distribution. We used both the ℓ_p and total variation priors for regularization for the statistical method.

From our findings, we determined that sparsity and smoothness regularization are needed during EIT inversion for improved image reconstruction. For this study, the statistical algorithm provided better reconstructions compared to IRGN in terms of both ℓ_2 and ℓ_1 errors. One drawback to the statistical approach is that it can be computationally expensive to run compared to the IRGN method. For low dimensional cases, the run times were about 40-45 minutes when we used the deterministic method as an initial guess. However, the IRGN method with Tikhonov regularization provided an initial guess to the solution within a few iterations, 5 - 15 on average, and took about 5 - 10 minutes.

Additional disadvantages of the statistical algorithm and IRGN method are their dependencies on the (1) location of the inclusions and (2) data noise. Reconstruction errors are higher as data noise increases and the location of inclusions move further inside the object. This result is a direct consequence of the ill-posed inverse problem. We verified this effect by creating inclusions closer to the surface as well as deeper into the body.

We also compared the statistical formulation for the DOT inverse problem and compared it with the classical IRGN method. From a visual point of view, we found that the statistical method outperforms the IRGN method up to high levels of relative noise. However, computing the statistical solution from the MCMC-based algorithm is computationally very expensive compared to the IRGN method. Therefore, analytical and iterative methods, such as IRGN, significantly decrease the time required for convergence of statistical methods.

Most experimental noise for EIT does not exceed 10%, however we do not know the exact noise distribution for the experimental data. We applied the IRGN method coupling with the statistical algorithm using experimental data for detecting damage inside a cement block. Overall, we found that the hybrid approach is a promising approach and computationally efficient. We conclude that, hybrid techniques may have a significant role in improving the parameter reconstructions in ill-posed inverse problems like EIT and DOT. Our future work is to investigate the non-symmetric eigenfunctions for the mollifier method in DOT and develop a theoretical framework for approximating the DOT eigenfunctions using symmetric eigenfunctions which will provide reasonable results from simulations. Another new direction is to develop a framework for comparing of various hybrid algorithms and determining an optimal hybrid method. Another direction is to explore machine learning approaches using the hybrid framework proposed in this dissertation.

Bibliography

[1] Sanwar Ahmad, Thilo Strauss, Shyla Kupis, and Taufiquar Khan. Comparison of statistical inversion with iteratively regularized gauss newton method for image reconstruction in electrical impedance tomography. *Applied Mathematics and Computation*, 358:436–448, 2019.

[2] Thowhida Akther. Dimensional analysis and variational formulation of diffuse optical tomography (dot) model. 2018.

[3] Simon R Arridge and William RB Lionheart. Nonuniqueness in diffusion-based optical tomography. *Optics letters*, 23(11):882–884, 1998.

[4] Simon R Arridge and John C Schotland. Optical tomography: forward and inverse problems. *Inverse Problems*, 25(12):123010, 2009.

[5] SR Arridge. Optical tomography in medical imaging: topical review. *Inverse Problems*, 15:R4193.

[6] George Backus and Freeman Gilbert. The resolving power of gross earth data. *Geophysical Journal International*, 16(2):169–205, 1968.

[7] George E Backus and JF Gilbert. Numerical applications of a formalism for geophysical inverse problems. *Geophysical Journal International*, 13(1-3):247–276, 1967.

[8] Anatoly Bakushinsky and Alexandra Smirnova. On application of generalized discrepancy principle to iterative methods for nonlinear ill-posed problems. *Numerical Functional Analysis and Optimization*, 26(1):35–48, 2005.

[9] Richard H Bayford. Bioimpedance tomography (electrical impedance tomography). *Annu. Rev. Biomed. Eng.*, 8:63–91, 2006.

[10] Lipman Bers, Salomon Bochner, and Fritz John. *Contributions to the theory of partial differential equations*. Princeton University Press, 1954.

[11] Liliana Borcea. Electrical impedance tomography. *Inverse problems*, 18(6):R99, 2002.

[12] A Borsic, Cesare Comina, Sebastiano Foti, Renato Lancellotta, and Guido Musso. Imaging heterogeneities with electrical impedance tomography: laboratory results. *Géotechnique*, 55(7):539–547, 2005.

[13] Martin Brühl, Martin Hanke, and Michael S Vogelius. A direct impedance tomography algorithm for locating small inhomogeneities. *Numerische Mathematik*, 93(4):635–654, 2003.

[14] Florian Bürgel, Kamil S Kazimierski, and Armin Lechleiter. A sparsity regularization and total variation based computational framework for the inverse medium problem in scattering. *Journal of Computational Physics*, 339:1–30, 2017.

[15] Alberto P Calderón. On an inverse boundary value problem. *Computational & Applied Mathematics*, 25(2-3):133–138, 2006.

[16] Subrahmanyan Chandrasekhar. *Radiative transfer*. Courier Corporation, 2013.

[17] Margaret Cheney, David Isaacson, and Jonathan C Newell. Electrical impedance tomography. *SIAM review*, 41(1):85–101, 1999.

[18] Margaret Cheney, David Isaacson, Jonathan C Newell, S Simske, and J Goble. Noser: An algorithm for solving the inverse conductivity problem. *International Journal of Imaging systems and technology*, 2(2):66–75, 1990.

[19] Kuo-Sheng Cheng, David Isaacson, JC Newell, and David G Gisser. Electrode models for electric current computed tomography. *IEEE Transactions on Biomedical Engineering*, 36(9):918–924, 1989.

[20] David Colton and Rainer Kress. *Inverse acoustic and electromagnetic scattering theory*, volume 93. Springer Science & Business Media, 2012.

[21] Cesare Comina, Renato Maria Cosentini, Gabriele Della Vecchia, Sebastiano Foti, and Guido Musso. 3d-electrical resistivity tomography monitoring of salt transport in homogeneous and layered soil samples. *Acta Geotechnica*, 6(4):195–203, 2011.

[22] John Cooper. *Sparsity regularization in diffuse optical tomography*. PhD thesis, Clemson University, 2012.

[23] Renato Maria Cosentini, Gabriele Della Vecchia, Sebastiano Foti, and Guido Musso. Estimation of the hydraulic parameters of unsaturated samples by electrical resistivity tomography. *Géotechnique*, 62(7):583–594, 2012.

[24] Richard Courant and David Hilbert. *Methods of Mathematical Physics: Partial Differential Equations*. John Wiley & Sons, 2008.

[25] William Daily, Abelardo Ramirez, Douglas LaBrecque, and John Nitao. Electrical resistivity tomography of vadose water movement. *Water Resources Research*, 28(5):1429–1442, 1992.

[26] Ingrid Daubechies. *Ten lectures on wavelets*, volume 61. Siam, 1992.

[27] Hamid Dehghani, Brian W Pogue, Steven P Poplack, and Keith D Paulsen. Multiwavelength three-dimensional near-infrared tomography of the breast: initial simulation, phantom, and clinical results. *Applied Optics*, 42(1):135–145, 2003.

[28] Louise C Enfield, Adam P Gibson, Nicholas L Everdell, David T Delpy, Martin Schweiger, Simon R Arridge, Caroline Richardson, Mohammad Keshtgar, Michael Douek, and Jeremy C Hebden. Three-dimensional time-resolved optical mammography of the uncompressed breast. *Applied optics*, 46(17):3628–3638, 2007.

[29] Hermann Engels. Numerical quadrature and cubature. 1980.

[30] Lawrence C. Evans. *Partial differential equations*. American Mathematical Society, Providence, R.I., 2010.

[31] LawrenceCraig Evans. *Measure theory and fine properties of functions*. Routledge, 2018.

[32] Yutaka Fuchino, Masahiro Nagao, Takusige Katura, Mitsuaki Bando, Masayoshi Naito, Atsushi Maki, Ken Nakamura, Hideaki Hayashi, Hideaki Koizumi, and Takeshi Yoro. High cognitive function of an als patient in the totally locked-in state. *Neuroscience letters*, 435(2):85–89, 2008.

[33] Rachel Elizabeth Grotheer. *Hyperspectral Diffuse Optical Tomography Using the Reduced Basis Method and Sparsity Constraints*. PhD thesis, Clemson University, 2016.

[34] Christina Habermehl, Susanne Holtze, Jens Steinbrink, Stefan P Koch, Hellmuth Obrig, Jan Mehnert, and Christoph H Schmitz. Somatosensory activation of two fingers can be discriminated with ultrahigh-density diffuse optical tomography. *Neuroimage*, 59(4):3201–3211, 2012.

[35] Sarah Hamilton, Andreas Hauptmann, and Samuli Siltanen. A data-driven edge-preserving d-bar method for electrical impedance tomography. *arXiv preprint arXiv:1312.5523*, 2013.

[36] J Handamard. Lectures on the cauchy problems in linear partial differential equations,(1923).

[37] Martin Hanke and Martin Brühl. Recent progress in electrical impedance tomography. *Inverse Problems*, 19(6):S65, 2003.

[38] Andreas H Hielscher, Raymond E Alcouffe, and Randall L Barbour. Comparison of finite-difference transport and diffusion calculations for photon migration in homogeneous and heterogeneous tissues. *Physics in Medicine & Biology*, 43(5):1285, 1998.

[39] Andreas H Hielscher, Alexander D Klose, Alexander K Scheel, Bryte Moa-Anderson, Marina Backhaus, Uwe Netz, and Jürgen Beuthan. Sagittal laser optical tomography for imaging of rheumatoid finger joints. *Physics in Medicine & Biology*, 49(7):1147, 2004.

[40] Bernd Hofmann, Barbara Kaltenbacher, Christiane Poeschl, and Otmar Scherzer. A convergence rates result for tikhonov regularization in banach spaces with non-smooth operators. *Inverse Problems*, 23(3):987, 2007.

[41] David S Holder. *Electrical impedance tomography: methods, history and applications*. CRC Press, 2004.

[42] Tsung-Chin Hou and Jerome P Lynch. Electrical impedance tomographic methods for sensing strain fields and crack damage in cementitious structures. *Journal of Intelligent Material Systems and Structures*, 20(11):1363–1379, 2009.

[43] José A Iglesias, Gwenael Mercier, and Otmar Scherzer. A note on convergence of solutions of total variation regularized linear inverse problems. *Inverse Problems*, 34(5):055011, 2018.

[44] O Isaksen, AS Dico, and Erling A Hammer. A capacitance-based tomography system for interface measurement in separation vessels. *Measurement science and technology*, 5(10):1262, 1994.

[45] Huabei Jiang. *Diffuse optical tomography: principles and applications*. CRC press, 2018.

[46] Bangti Jin, Taufiquar Khan, and Peter Maass. A reconstruction algorithm for electrical impedance tomography based on sparsity regularization. *International Journal for Numerical Methods in Engineering*, 89(3):337–353, 2012.

[47] Bangti Jin and Peter Maass. An analysis of electrical impedance tomography with applications to tikhonov regularization. *ESAIM: Control, Optimisation and Calculus of Variations*, 18(4):1027–1048, 2012.

[48] Bangti Jin and Peter Maass. Sparsity regularization for parameter identification problems. *Inverse Problems*, 28(12):123001, 2012.

[49] Jari P Kaipio, Ville Kolehmainen, Erkki Somersalo, and Marko Vauhkonen. Statistical inversion and monte carlo sampling methods in electrical impedance tomography. *Inverse problems*, 16(5):1487, 2000.

[50] Peter G Kaup, Fadil Santosa, and Michael Vogelius. A method for imaging corrosion damage in thin plates from electrostatic data. Technical report, Cornell University, 1995.

[51] Jirair Kevorkian. *Partial Differential Equations: Analytical Solution Techniques (Texts*, volume 89871. Springer, 1990.

[52] Taufiquar Khan and Alexandra Smirnova. 1d inverse problem in diffusion based optical tomography using iteratively regularized gauss–newton algorithm. *Applied mathematics and computation*, 161(1):149–170, 2005.

[53] Alexander D Klose and Andreas H Hielscher. Iterative reconstruction scheme for optical tomography based on the equation of radiative transfer. *Medical physics*, 26(8):1698–1707, 1999.

[54] Kim Knudsen, Matti Lassas, Jennifer L Mueller, and Samuli Siltanen. D-bar method for electrical impedance tomography with discontinuous conductivities. *SIAM Journal on Applied Mathematics*, 67(3):893–913, 2007.

[55] Hideaki Koizumi, Tsuyoshi Yamamoto, Atsushi Maki, Yuichi Yamashita, Hiroki Sato, Hideo Kawaguchi, and Noriyoshi Ichikawa. Optical topography: practical problems and new applications. *Applied optics*, 42(16):3054–3062, 2003.

[56] Armin Lechleiter and Andreas Rieder. Newton regularizations for impedance tomography: a numerical study. *Inverse Problems*, 22(6):1967, 2006.

[57] AK Louis. Approximate inverse for linear and some nonlinear problems. *Inverse problems*, 12(2):175, 1996.

[58] AK Louis. A unified approach to regularization methods for linear ill-posed problems. *Inverse problems*, 15(2):489, 1999.

[59] Alfred K Louis and Peter Maass. A mollifier method for linear operator equations of the first kind. *Inverse problems*, 6(3):427, 1990.

[60] Peter Maass, Michael Pidcock, and Cristiana Sebu. A regularized solution for the inverse conductivity problem using mollifiers. *Inverse Problems in Science and Engineering*, 18(1):145–161, 2010.

[61] Olavo H Menin, Vanessa Rolnik, and Alexandre S Martinez. Boundary element method and simulated annealing algorithm applied to electrical impedance tomography image reconstruction. *Revista Brasileira de Ensino de Física*, 35(2):1–7, 2013.

[62] Kiyoshi Mochizuki. Eigenfunction expansions associated with the schrödinger operator with a complex potential and the scattering theory. *Publications of the Research Institute for Mathematical Sciences, Kyoto University. Ser. A*, 4(2):419–466, 1968.

[63] Frank Natterer, Helmut Sielschott, Oliver Dorn, Thomas Dierkes, and Victor Palamodov. Fréchet derivatives for some bilinear inverse problems. *SIAM journal on applied mathematics*, 62(6):2092–2113, 2002.

[64] Frank Natterer and Frank Wübbeling. *Mathematical methods in image reconstruction*, volume 5. Siam, 2001.

[65] Robert L Parker. The inverse problem of resistivity sounding. *Geophysics*, 49(12):2143–2158, 1984.

[66] Boris Sergeevich Pavlov. Selfadjoint dilatation of the dissipative shrdinger operator and its resolution in terms of eigenfunctions. *Matematicheskii Sbornik*, 144(4):511–536, 1977.

[67] Brian W Pogue, Steven P Poplack, Troy O McBride, Wendy A Wells, K Sunshine Osterman, Ulf L Osterberg, and Keith D Paulsen. Quantitative hemoglobin tomography with diffuse near-infrared spectroscopy: pilot results in the breast. *Radiology*, 218(1):261–266, 2001.

[68] Nick Polydorides and William RB Lionheart. A matlab toolkit for three-dimensional electrical impedance tomography: a contribution to the electrical impedance and diffuse optical reconstruction software project. *Measurement science and technology*, 13(12):1871, 2002.

[69] WH Press, SA Teukolsky, WT Vetterling, and BP Flannery. Numerical recipies in fortran ., cambridge university press, cambridge,(1992).

[70] Luca Rondi. On the regularization of the inverse conductivity problem with discontinuous conductivities. *Inverse Problems & Imaging*, 2(3):397–409, 2008.

[71] Luca Rondi and Fadil Santosa. Enhanced electrical impedance tomography via the mumford–shah functional. *ESAIM: Control, Optimisation and Calculus of Variations*, 6:517–538, 2001.

[72] Wilhelm Conrad Röntgen. On a new kind of rays. *Science*, 3(59):227–231, 1896.

[73] Martin Schechter. *Principles of functional analysis*. Number 36. American Mathematical Soc., 2001.

[74] Alexandra Smirnova, Rosemary A Renaut, and Taufiquar Khan. Convergence and application of a modified iteratively regularized gauss–newton algorithm. *Inverse problems*, 23(4):1547, 2007.

[75] Erkki Somersalo, Margaret Cheney, and David Isaacson. Existence and uniqueness for electrode models for electric current computed tomography. *SIAM Journal on Applied Mathematics*, 52(4):1023–1040, 1992.

[76] Robert W Stacey. Electrical impedance tomography. *Department of Energy and by the Department of Petroleum Engineering, Stanford University*, 2006.

[77] Gabriele Steidl. Combined first and second order variational approaches for image processing. *Jahresbericht der Deutschen Mathematiker-Vereinigung*, 117(2):133–160, 2015.

[78] Thilo Strauss. *Statistical Inverse Problems in Electrical Impedance and Diffuse Optical Tomography*. PhD thesis, Clemson University, 2015.

[79] Thilo Strauss. Personnel communication. Feb, 2019.

[80] Miyuki Suda, Kanehisa Morimoto, Akiko Obata, Hideaki Koizumi, and Atsushi Maki. Emotional responses to music: towards scientific perspectives on music therapy. *Neuroreport*, 19(1):75–78, 2008.

[81] Gentaro Taga, Kayo Asakawa, Atsushi Maki, Yukuo Konishi, and Hideaki Koizumi. Brain imaging in awake infants by near-infrared optical topography. *Proceedings of the National Academy of Sciences*, 100(19):10722–10727, 2003.

[82] Satoshi Tsujimoto, Tsuyoshi Yamamoto, Hideo Kawaguchi, Hideaki Koizumi, and Toshiyuki Sawaguchi. Prefrontal cortical activation associated with working memory in adults and preschool children: an event-related optical topography study. *Cerebral cortex*, 14(7):703–712, 2004.

[83] Päivi J Vauhkonen. *Image reconstruction in three-dimensional electrical impedance tomography*. Kuopion yliopisto, 2004.

[84] Stephen Wright and Jorge Nocedal. Numerical optimization. *Springer Science*, 35(67-68):7, 1999.

[85] Minghua Xu and Lihong V Wang. Photoacoustic imaging in biomedicine. *Review of scientific instruments*, 77(4):041101, 2006.

[86] Benjamin W Zeff, Brian R White, Hamid Dehghani, Bradley L Schlaggar, and Joseph P Culver. Retinotopic mapping of adult human visual cortex with high-density diffuse optical tomography. *Proceedings of the National Academy of Sciences*, 104(29):12169–12174, 2007.